UNIVERSITÀ DEGLI STUDI "ROMA TRE"

DOTTORATO DI RICERCA IN FISICA

XXVIII CICLO

Next-generation Laser Retroreflectors for Precision Tests of General Relativity

Relazione sull'attività di Dottorato di

Manuele Martini

Relatore Interno:
Prof. Aldo Altamore

Relatore Esterno:
Dr. Simone Dell'Agnello, LNF-INFN

Coordinatore:
Prof. Roberto Raimondi

Anno Accademico 2015/2016

Alla mia famiglia...

Contents

List of Acronyms

ASI Agenzia Spaziale Italiana

APOLLO Apache Point Observatory Lunar Laser ranging Operation

CERGA Centre d'Etudes et de Recherche en Géodynamique et Astronomie

CCR Corner Cube Retroreflector

DAO Dihedral Angle Offset

ETRUSCO Extra Terrestrial Ranging to Unified Satellite COnstellations

FFDP Far Field Diffraction Pattern

GLONASS GLObal NAvigation Satellite System

GNSS Global Navigation Satellite System

GPS Global Positioning System

GR General Relativity

ILN International Lunar Network

ILRS International Laser Ranging Service

INFN Istituto Nazionale di Fisica Nucleare

INRRI INstrument for landing-Roving laser ranging/altimetry Retroreflector Investigations

LAGEOS LAser GEOdynamics Satellites

LLR Lunar Laser Ranging

LLRRA21 Lunar Laser RetroReflector for the 21^{st} Century

LNF Laboratori Nazionali di Frascati

LRA Laser Retroreflector arrays

MLRO Matera Laser Ranging Observatory

MLRS McDonald Laser Ranging Station

MoonLIGHT Moon Laser Instrumentation for General relativity High accuracy Tests

OCA Observatoire de Côte d'Azur

PEP Planetary Ephemeris Program

PPN Parametrized Post Newtonian

SCF_Lab Satellite/lunar/GNSS laser ranging/altimetry and Cube/microsat Characterization Facilities Laboratory

SLR Satellite Laser Ranging

VA Velocity Aberration

VLBI Very Long Baseline Interferometry

Preface

Why this work at LNF-INFN

Lunar Laser Ranging (LLR) is used to conduct high-precision measurements of ranges between an observatory on Earth and a laser retroreflector on the lunar surface. Over the years, LLR has benefited from a number of improvements both in observing technology and data modeling, which led to the current accuracy of postfit residuals of $\sim$2 cm. Today LLR is a primary technique to study the dynamics of the Earth-Moon system and is especially important for gravitational physics, geodesy, and studies of the lunar interior [2] [3] [4] [5]. When the gravitational physics is concerned, LLR is used to perform high-accuracy tests of the equivalence principle, to search for a time variation in the gravitational constant, and to test predictions of various alter- native theories of gravity. LLR contributes to the realization of both the terrestrial and selenocentric reference frames. In contrast to the kinematically-realized frame of Very Long Baseline Interferometry (VLBI), the realization of a dynamically-defined inertial reference frame offers new possibilities for mutual crosschecking and confirmation Finally, LLR also investigates the processes related to the Moon's interior dynamics. Since 1969 LLR to the Apollo CCR arrays has supplied several significant tests of General Relativity (GR) [6] [7]: it has evaluated the Geodetic Precession, probed the weak and strong equivalence principle, determined the Parametrized Post Newtonian (PPN) parameter, addressed the time change of the gravitational constant (G) and $1/r^2$ deviations. The group I work with and I show that the Moon equipped with retroreflectors can be used effectively

to test new gravitational theories beyond GR, like spacetime torsion. LLR has also provided important information on the composition and the origin of the Moon by measuring its rotations and tides.
Initially, the Apollo arrays contributed a negligible portion of the LLR error budget. Nowadays, the ranging accuracy of ground stations has improved by more than two orders of magnitude: the new Apache Point Observatory Lunar Laser ranging Operation (APOLLO) station at Apache Point, USA, is capable to make measurements with a level of accuracy to the mm; Matera Laser Ranging Observatory (MLRO), at the Agenzia Spaziale Italiana (ASI) Space Geodesy Center of Matera in Italy, has restarted LR operations. Now, because of lunar librations, the Apollo arrays dominate the LLR error budget, which is of a few cm. The University of Maryland, Principal Investigator for the Apollo arrays, and Istituto Nazionale di Fisica Nucleare (INFN)-Laboratori Nazionali di Frascati (LNF) are proposing an innovative CCR array design that will reduce the error contribution of LLR payloads by more than two orders of magnitude, down to tens of microns. This is the goal of the MoonLIGHT, a technological experiment of INFN and of the Satellite/lunar/GNSS laser ranging/altimetry and Cube/microsat Characterization Facilities Laboratory (SCF_Lab), the CCR space test facility at LNF [1]. The main challenges for this new array design are: 1) address the thermal and the optical effects of the absorption of solar radiation within the CCR; reduce the heat transfer from the hot housing and from the rapid temperature changes of the regolith to the CCR; 2) define a method of deploying the CCR package on the Moon's surface in order to be stable over the lunar day/ night cycle; 3) adapt the design to the type of robotic mission (lander only or lander plus rover) and site.

What my contribution is

My thesis period at INFN-LNF should be divided into three main parts:

- Work in the field of optics;
- Industrial & quality assurance;

- Physics analysis

Work in the field of optics

SCF_Lab is an infrastructure equipped with instruments for characterization and modeling of the detailed thermal behavior and the optical performance ("SCF-Test") of CCRs and with the INFN experiment Extra Terrestrial Ranging to Unified Satellite COnstellations (ETRUSCO) these activities were performed for the LAser GEOdynamics Satellites (LAGEOS) 1 and for a prototype hollow CCR. Our key experimental innovation is the concurrent measurement and modeling of the Far Field Diffraction Pattern (FFDP) and the temperature distribution of the retroreflector payload under thermal conditions produced with a close-match solar simulator. These unique capabilities provide experimental validation [8] of the space segment for Satellite and lunar laser ranging (Satellite Laser Ranging (SLR)/LLR). An uncoated retroreflector with properly insulated mounting can minimize thermal degradation and significantly increase the optical performance, and as such, it is emerging as the recommended design for modern Global Navigation Satellite System (GNSS) satellites.

Industrial & quality assurance

Working on optics, I also spent a lot of time in optics work for industrial acceptance test of a huge variety of CCRs.
The "acceptance" test of the CCR optical performance is the measurement of the absolute angular size and the shape of single-CCR FFDP with linearly polarized CW lasers. FFDP are acquired with the CCR in air and isothermal conditions. The absolute angular scale of the circuit is calibrated with the double-slit method to test the consistency of each CCR FFDP with its nominal Dihedral Angle Offset (DAO). We also measure the FFDP intensity relative to the Airy Peak, obtained with optical flats of known reflectivity, as an indicator of the CCR laser return.
FFDP measurements are modeled with CodeV, a software package by Optical Research Associates, Inc. The INFN-LNF CCR FFDP test procedure [9] has been

developed in 2007/2008 with GLONASS prototypes and a GPS-2 flight model array given on loan by the University of Maryland at College Park to LNF, all composed of Al-coated fused silica retroreflectors with an hexagonal front face of approximately 27 mm diameter. In summer 2008 this procedure was applied to the FFDP test of LAGEOS Sector.

Physics analysis

Regarding the physics measurements, I made the very first offline physics analysis work of LLR data with CfA's Planetary Ephemeris Program (PEP) software at INFN-LNF. In particular, I spent a lot of time understanding PEP.
The very first measurement made by the SCF_Lab is the estimation of the expected accuracy on geodetic precession variation (h) that is presented in this thesis work.

The present work is divided into 6 chapters. The first chapter is an introduction to SLR/LLR. In particular I will explain how a station works and what is a CCR.
The second chapter is devoted to the description of the test of General Relativity that can be done using the laser ranging technique.
The SCF_Lab infrastructure is shown in the third chapter.
The fourth chapter deals with the description of the MoonLIGHT-2 experiment.
The fifth chapter is focused on the experimental results obtained with the SCF-Test. In particular this chapter is splitted into three sections: optical simulations, optical results and thermal results.
In the last chapter I will show the results obtained with the tests of general relativity using the PEP software. I will also show the possible improvements carried out with MoonLIGHT-type CCR on lunar surface. Last but not least there will be conclusions and future prospects of this thesis work.

Chapter 1

Satellite/Lunar Laser Ranging

In this section I am going to describe the actual scientific objectives carried out using SLR and LLR techniques.
The origins of the SLR technique, as well as LLR, go back to the 1950's. Some scientists were considering a possible way to look on changes in the gravitational constant using precision tracking of artificial satellites. In order to do this, they deployed CCR (cfr 1.3) on the satellite and fired light pulses from the ground to measure angular motion respect to stars [10] [11].
After the development of lasers, laser ranging measurements became much more accurate.
A huge variety of scientific objectives achievable using laser measurements were:

- Improvement of lunar orbit;
- Determination of CCR position;
- Measurements of lunar librations.

The SLR/LLR technique consists in a time-of-flight measurement of short laser pulses fired from ground stations of the International Laser Ranging Service (ILRS) towards payloads of CCRs on the Moon/Satellites, and then retroreflected back to the stations. Nowadays laser ranging technique provides precise, metrologically

absolute positioning measurements in the gravitational laboratory of the Sun-Earth-Moon system with a space segment based on cost-effective, passive, maintenance-free payloads.

Using SLR/LLR is possible to provide the best test for every parameter in table 1.1. We are interested in these kind of parameters because any possible departure from

Parameter	General Relativity value	Up to 2004 (cm)
PPN, $\beta - 1$	0	1.1×10^{-4}
WEP	0	1.4×10^{-13}
SEP, η	0	4.4×10^{-4}
$\dot{G}/G$	0	9×10^{-13}
$1/r^2$	0	3×10^{-11}
Geodetic Precession	0	6.5×10^{-3}

Table 1.1: Science constraints using LLR updated to 2004.

their value in GR would imply [12]:

- A change in the lunar orbit (from $\dot{G}/G$);
- other gravity theories (from $1/r^2$);
- implications in dark energy and cosmological constant from geodetic precession;
- possible new metrics theories of gravity (from equivalence principle through Nordtvedt parameter η, β and γ.

For further details about the tests see chapter 2 and 6.

1.1 The ILRS

The ILRS was established during late 90s (1998) to support programs in geodetic, geophysical, and lunar research activities. It also provides products for the Interna-

tional Earth Rotation Service (IERS) in order to maintain an accurate International Terrestrial Reference Frame (ITRF).

Figure 1.1: ILRS stations network

The stations able to do SLR/LLR are reported in figure 1.1, but only few of these stations are able to reach the Moon. The first one, born in 1970, is McDonald Observatory, Texas (USA). It was fully dedicated to lunar ranging and ceased its activities in 1985 after routine maintenance activities and remained non-operational for more than 15 years. The transition to the McDonald Laser Ranging Station occurred on two sites: MLRS1 (1983-1988) and MLRS2 (since 1988) which shared lunar and artificial satellite ranging facilities. In the 1980s, two other stations have carried out Lunar Laser Ranging: the Haleakala Observatory on Maui, (USA), produced high-quality data over a few years around 1990. Since 1982, Centre d'Etudes et de Recherche en Géodynamique et Astronomie (CERGA) station is active at the Observatoire de Côte d'Azur (OCA), (France). All the data used for our analysis and for our simulations (see Chapter 6) come from the two observatories that are still operating: McDonald and CERGA; besides the new APOLLO. ASI-MLRO in Italy has recently re-started LLR operations.

However over the past four decades the ground station technology has greatly improved, enhancing LLR accuracy (fig.1.2). Historically the accuracy of LLR measurements is dropped from more than 30 cm, to about 2 cm, thanks to the improvement of the LLR stations and their capability to records photons. But as shown in fig.1.2, an asymptote has been reached from 1995 to 2005 so it is necessary to accomplish the same improvements on the CCR side.

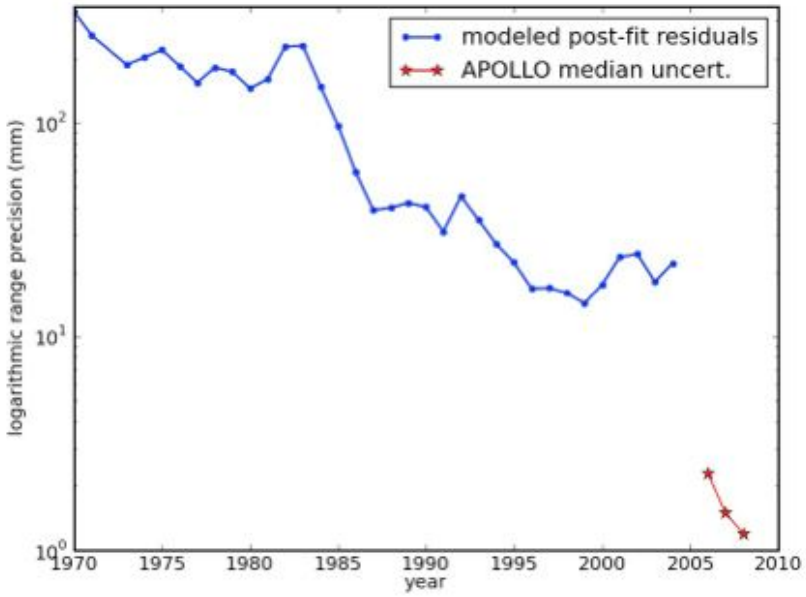

Figure 1.2: LLR accuracy improvements over the years and before the advent of APOLLO [12]

1.2 How it works

The basic idea in order to do this kind of measurement is to measure the time of flight of a laser pulse from the station to the satellite/Moon and return. The main issue to take into account is the need of a very collimated laser pulse. The first problem to resolve is that the atmosphere turbulence distorts the laser beam, giving a divergence of about 1 arcsecond. For the Moon this divergence translates into ~ 2

kilometers.

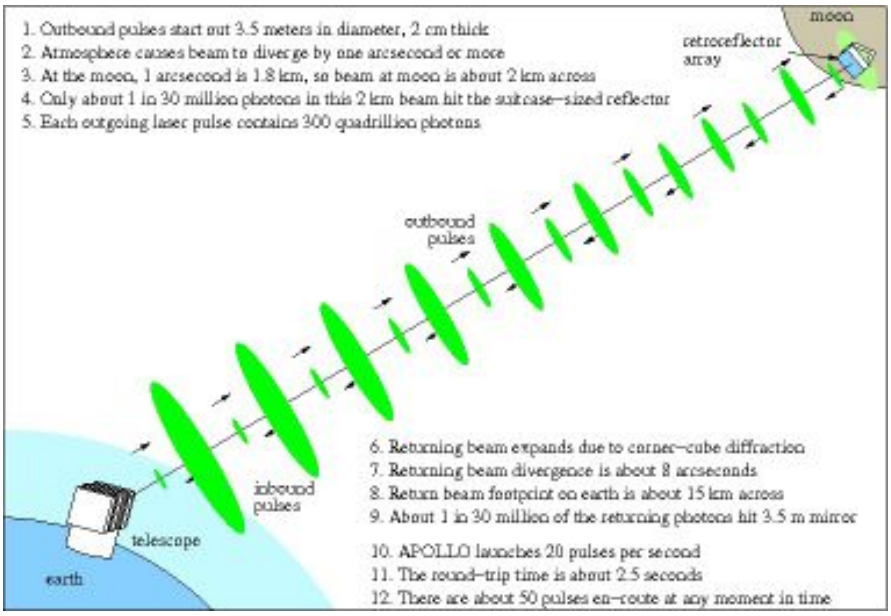

Figure 1.3: Simple sketch of laser ranging technique [13]

As shown in fig.1.3, the station sends a laser pulse to the Moon, this pulse diverges and approximately only one part in 30 million of the light hits the retroreflector array. Due to the CCR, the returning pulse has a divergence itself. For Apollo reflectors the divergence is ~ 8 arcsec. Due to this divergence, the beam retroreflected to the station has dimensions of about 15 kilometers.
Undoubtedly, in order to achieve millimeter-range measurements, it is necessary to record thousands of photons. The main procedure is to send 10^{17} photons every pulse from the station; they record 5 photons in return reaching thousands of returns thanks to the very fast pulse of the laser (about 20 pulses per second).

1.3 Corner Cube Retroreflectors

A CCR is a solid cube corner retroreflector, typically made out of fused silica (see fig.1.4). The CCRs are mounted in Laser Retroreflector arrays (LRA) that are passive, lightweight, maintenance free, and, if built with proper thermal design and choice of materials like the Apollo ones (fig.1.4), can provide very good performance for several decades.

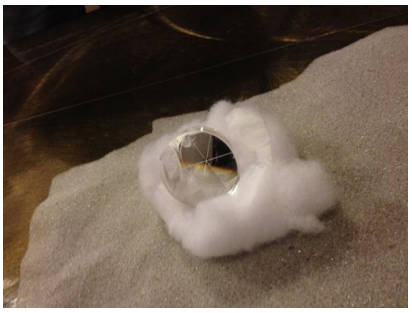

Figure 1.4: Apollo 14 CCR

In simple words, a CCR is a device that retroreflects the light back in the extact direction from which it came. It consists of three perpendicular reflective surfaces forming a corner of a cube. There are different kinds of CCRs, but in this section we will examine in depth the coated and the uncoated ones.
Regarding the uncoated CCR, its performance was demonstrated with the Apollo 11, 14 and 15 arrays deployed on lunar surface by Apollo missions. These three arrays contain hundreds of 38 mm diameter CCRs mounted inside some special cavities (see fig.1.5).

Uncoated cubes like the Apollo ones were also used with the LAGEOS. The orbital precision on this kind of satellites is about 1 cm. In chapter 4 I will show the future of lunar CCR with the MoonLIGHT project. The main purpose is to use a new bigger CCR (100 mm instead of 38), fig.1.6, in order to better estimate the Earth-Moon distance and to test General Relativity with LLR.

Back-coated aluminum cubes of about 28 mm active diameter were used for the

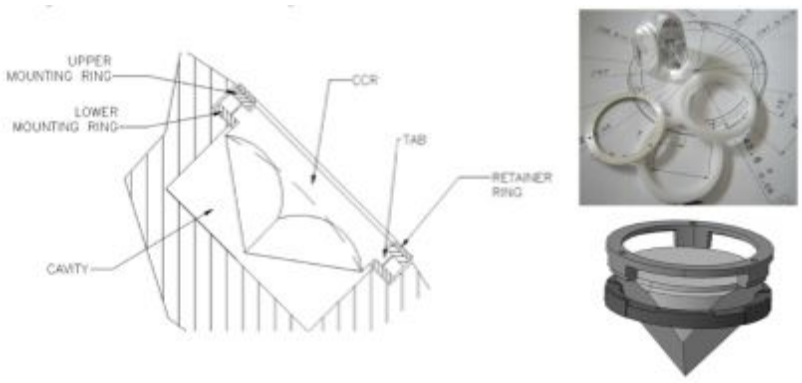

Figure 1.5: Apollo CCR mounting scheme

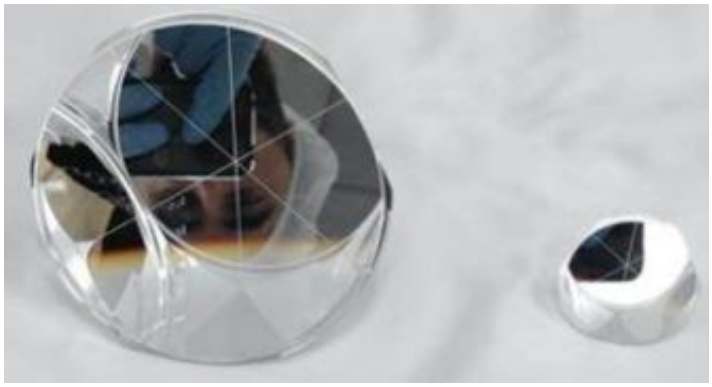

Figure 1.6: Comparison between Apollo and MoonLIGHT CCR

first generation GNSS constellations, GLObal NAvigation Satellite System (GLONASS) and Global Positioning System (GPS) starting in the late 1980s. The mounting scheme of this kind of CCR was really different from the uncoated one; in particular they were mounted inside a special aluminum housing (see fig.1.7).

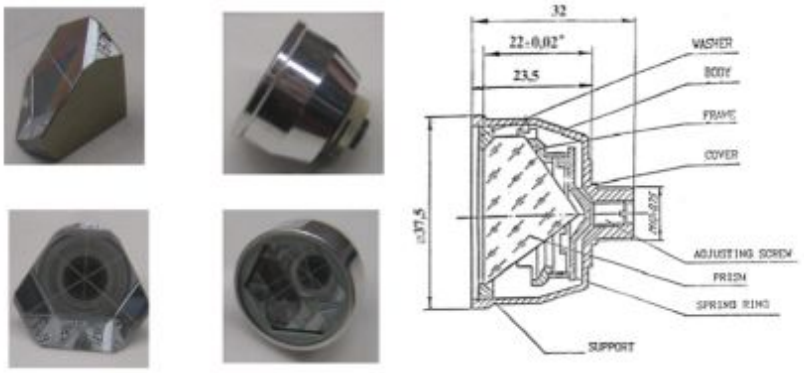

Figure 1.7: GLONASS CCR mounting scheme

New GNSS constellations and satellites are starting to use uncoated fused silica retroreflectors, following the test results obtained with the group I work with (SCF_Lab) [14].

1.3.1 Apollo & Lunokhod CCR

Actually on the lunar surface there are 5 different arrays of CCRs (see fig.1.8). Three of them were installed by Apollo missions astronauts (Apollo 11, 14 and 15); the other two arrays come from unmanned missions (Luna 17 and Luna 21).

Apollo 11 and Apollo 14 have 100 38 mm diameter CCRs in a square pattern of 10×10. The Apollo 15 array is bigger then the others, in particular it has an hexagonal shape and has 300 38 mm diameter CCRs. Due to its dimension, it is preferentially used for LLR measurements. Nowadays $\sim$ 78% of LLR data come from measurements to Apollo 15 array.

The two arrays from unmanned missions are two rovers called Lunokhod 1 and

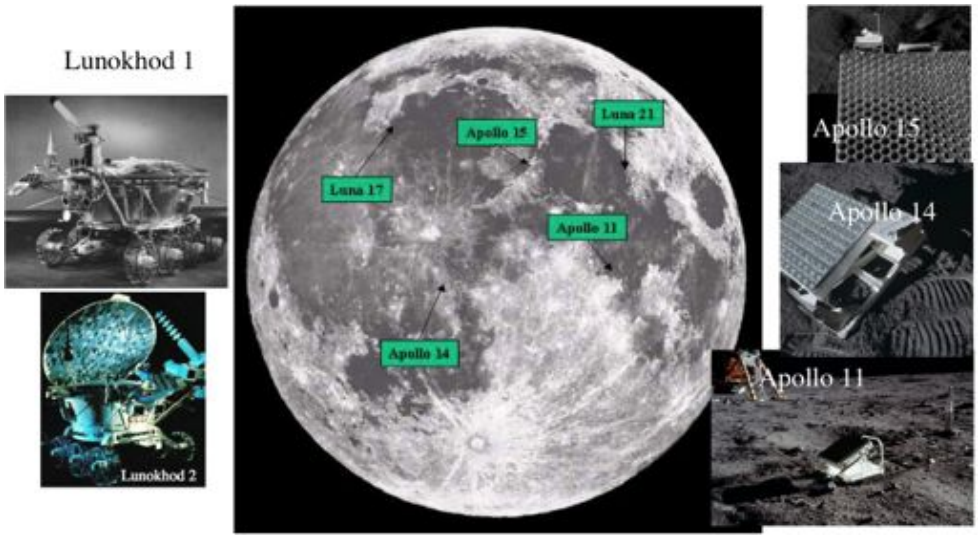

Figure 1.8: GLONASS CCR mounting scheme

Lunokhod 2 equipped with small arrays of CCRs. Those arrays are constituted by 14 CCRs in triangular configuration.

Chapter 2

General Relativity tests

In this chapter I will focus on the history of GR tests starting from the ones originally proposed by Einstein, to the modern tests. In the last section we will give a brief introduction to PPN formalism, giving particular attention to parameters β, γ and η.

2.1 Tests originally proposed by Einstein

GR was developed by Einstein between 1907 and 1915. During these years, Einstein calculated observable effects of GR like Mercury perihelion precession, the deflection of light and the gravitational redshift.

2.1.1 Mercury perihelion precession

According to astronomical observations, in the early 1600s Kepler was able to determine that the orbit of a planet from the Sun is an ellipse, with the Sun occupies one focus. Assuming that a planet is subject only to the gravitational force of the Sun, we can obtain Kepler's result using Newton's theory.
But the other planets exert a gravitational pull on the planet in question. What is the effect of their presence? If we repeat the calculation considering this compli-

cation, it turns out that the attraction of all the other planets of the solar system on the planet in question induces a perihelion advance . Even the precession of the Earth's rotation results in the same effect. For example, the perihelion of Mercury moves slightly at the speed of 5600 arcseconds/century, in the same direction in which the planet revolves around the sun. However, removing the contribution of the Earth's precession (5025 arcseconds), the one due to to the attraction of other planets, we obtain a missing 43 arcseconds.
The solution to this missing 43 arcseconds came in 1915, when Einstein applied the final version of his theory of gravity to calculate the orbit of Mercury. General relativity, in fact, exactly reproduces the observed precession, recovering the missing 43 arcseconds. In addition to that of Mercury, in recent years were measured with high accuracy also precession of all the other planets of the solar system. And the results are in good agreement with general relativity. The expiression of the perihelion advance predicted by Einstein is shown in eq.2.1.

$$\Delta\pi R = \frac{3n^3a^2}{c^2\left(1-e^2\right)^2}t \tag{2.1}$$

Where n is the mean motion of the planet, a is the semiaxis, e is the eccentricity, t is the time and c is the speed of light.

2.1.2 Deflection of light

In this section we want to compute the deflection angle produced by a massive body (like a star) on a massless particle, otherwise a photon. For this reason we define the following parameters (see figure 2.1 for reference):

- r = radial coordinate of the photon in frame centered with the center of the massive body and the periastron is indicated as r_0
- b = distance between the direction of the photon and center of attraction, otherwise called impact parameter.

- δ = angle between the incoming photon direction and the outgoing direction, otherwise called deflection angle.

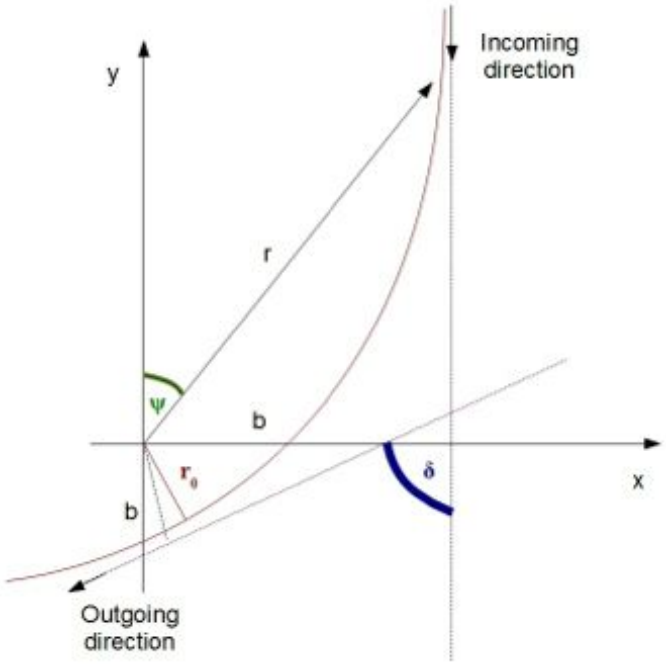

Figure 2.1: Schematic view of the deflection of a photon by a massive body. See text for details

The aim is to evaluate δ. It's important to underline that, since the Schwarzchild metric is invariant under time reflection, so event the particle is invariant under time reflection and the photon can follow the line in figure 2.1 the direction marked by the arrow or in the opposite one. Referring always to figure 2.1 we first assume, $\forall$ r that:

$$\frac{m}{r} \ll 1 \tag{2.2}$$

This condition is always satisfied when we consider photons deflected by the Sun, in fact calling R_S the Sun radius we have:

$$\frac{m}{r} \leq \frac{m}{R_S} \approx 10^{-6} \tag{2.3}$$

then we define a starting orientation where:

$$\psi^{in} = 0 \tag{2.4}$$

and an outgoing orientation where:

$$\psi^{out} = \pi + \delta \tag{2.5}$$

From figure 2.1, assuming that photon is at infinity (r tends to infinity and $\psi \approx 0$), we can approximate the impact parameter:

$$b = \lim_{\psi \to 0} r sin\psi = r\psi \tag{2.6}$$

then expressing deriving respect to ψ we have:

$$\frac{d\psi}{dr} \approx -\frac{b}{r^2} \tag{2.7}$$

Using the geodesic equations of Schwarzchild metric for a massless particle we have:

$$\frac{d\psi}{dr} = \pm \frac{L}{r^2\sqrt{E^2 - V(r)}} \tag{2.8}$$

where L is the angular momentum of the photon, E is the Energy and V(r) is the potential at r distance.
Now comparing equations 2.7 and 2.8 we obtain in the limit of r $\to \infty$ we obtain:

$$\frac{d\psi}{dr} \approx \pm - \frac{L}{Er^2} \tag{2.9}$$

Finally combining equations 2.9 with 2.6 and 2.7 we obtain an expression for the impact parameter:

$$b \approx \frac{L}{E} \tag{2.10}$$

According to General Relativity a photon is deflected by a gravitational field if $E^2 < V_{max}$ otherwise, knowing that the potential as only one maximum at r =3m (see figure 2.2) and there $V_{max} = \frac{L^2}{27m^2}$ we obtain the condition:

$$E^2 < \frac{L^2}{27m^2} \tag{2.11}$$

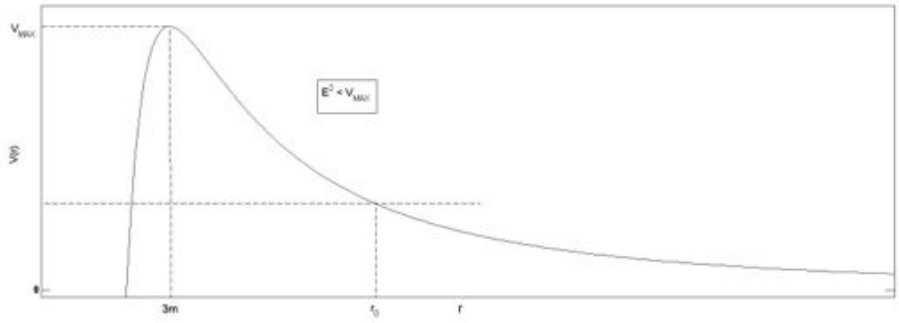

Figure 2.2: Potential behaviour for a massless particle in function of the distance r from the center of a massive body

Now comparing equations 2.11 with 2.10 we obtain a constrain for the impact parameter

$$b \geq \sqrt{27}m \equiv b_{critical} \tag{2.12}$$

$b_{critical}$ define a condition on the photon, if the impact parameter is smaller than $b_{critical}$ then the particle is captured by the central body, so for a deflection condition b must be grater then $b_{critical}$. To find the deflection angle we can use the

Schwarzchild metric geodesic for a massless particle orbiting around a massive body and write:

$$\dot{\psi} = Lu^2 \tag{2.13}$$

$$\dot{r} = -Lu' \tag{2.14}$$

where the new variable u is defined as: $u \equiv \frac{1}{r}$ and must satisfy the equations:

$$u'' + u - 3mu^2 = 0 \tag{2.15}$$

Resolving the two equations using the following boundary conditions:

$$u(\psi = 0) = 0 \tag{2.16}$$

$$u'(\psi = 0) = -\frac{1}{b} \tag{2.17}$$

If the central body is massive then the photon is deflected and the solution is described by 2.18

$$\frac{3m}{r} << 1 \tag{2.18}$$

we can solve the 2.15 with conditions 2.18 using a perturbative approach, finally we obtain the complete solution for u:

$$u = \frac{1}{b}sin\psi + \frac{3m}{2b^2}\left(1 + \frac{1}{3}cos2\psi - \frac{4}{3}cos\psi\right) \tag{2.19}$$

Assuming $\psi = \pi + \delta$ we obtain:

$$\psi_{out} = u(\pi + \delta) \simeq -\frac{\delta}{b} + \frac{3m}{2b^2}\frac{8}{3} \tag{2.20}$$

For the conditions $\psi_{out} = 0$ we obtain:

$$\delta = \frac{4m}{b} \tag{2.21}$$

Considering a photon travelling near the Sun we obtain finally the deflection of Light produced by Sun masses as:

$$\delta \simeq 1.75arcsec \tag{2.22}$$

The early measurement of the bending of a optical starlight was produced by Eddington, Dayson and Dividson during a solar eclipse in 1919 and this is one of the most important success of the General Relativity theory (fig.2.3). Eddington, Dayson and Davidson measured the apparent position of a star behind the Sun during the eclipse (in this way the reduced Sun luminosity allowed the star radiation to be visible from the Earth). However tat test was carried out with an accuracy of 30% then increased with following experiment until 1970-1980 at around 10%.

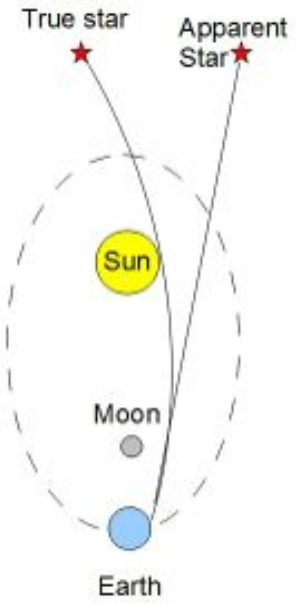

Figure 2.3: Schematic example of Eddington, Dayson and Dividson light deflection test

The results was inside a range of 1.5 and 2 times the Einstein predicted value. A great improvement was provided by the Long-baseline and very-long-baseline interferometry that measures the bending of radio waves produced by quasar; with this technique is possible to reach an accuracy of about 1%.

2.1.3 Gravitational redshift

Lets consider a clock based on the atomic oscillations of a quartz crystal. in a frame which the clock is at rest the interval proper time between two clicks will be depended on the metric, and considering the clock respect to reference frame:

$$dT = \frac{1}{c}(-g_{\mu\nu}dx^{\mu}dx^{\nu})^{\frac{1}{2}} \tag{2.23}$$

Assuming that the clock is moving respect to the frame with a velocity $\frac{dx^{\alpha}}{dt}$ we can obtain the time dilation factor $\frac{dT}{dt}$ in the frame x^{μ} that depends on the metric and on the velocity. Considering teh clock at rest and using equation 2.23 we obtain:

$$\frac{dT}{dt} = [-g_{00}]^{\frac{1}{2}} \tag{2.24}$$

Due to this factor the frequency of signals detected at a given point different from the source point, changes with respect to the emission frequency. Consider a metric independent from time (so we can assume x^0 as universal time), S the source of light that emit two wave crest to O the observer just like in fig.2.4.

If S and O are at rest in a stationary field, the time interval of the light to go to O from S is a constant, therefore the two wave crest reaches O with a defined time. The wave crest are emitted with a period ΔT_{em} (otherwise the source proper time) and a frequency $\nu_{em} = \frac{1}{\Delta T_{em}}$ where:

$$\Delta T_{em} = [-g_{00}]^{\frac{1}{2}}\Delta t_{em} \tag{2.25}$$

Similar condition we have for the observer:

$$\Delta T_{obs} = [-g_{00}]^{\frac{1}{2}}\Delta t_{obs} \tag{2.26}$$

$$\nu_{obs} = \frac{1}{\Delta T_{obs}} \tag{2.27}$$

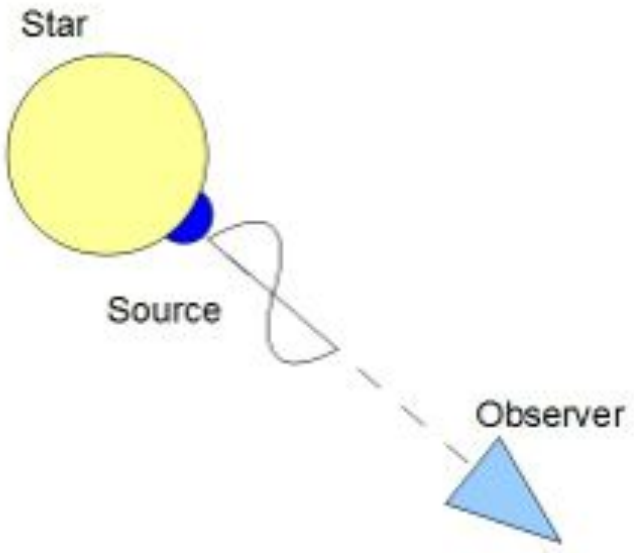

Figure 2.4: Schematic view of the gravitational redshift. See text for details

So we have comparing 2.25 with 2.26, using $\Psi = -\frac{GM}{r}$ with M the mass of the body generating the gravitational field and choosing the approximation of weak gravitational field near O:

$$\frac{\nu_{em} - \nu_{obs}}{\nu_{em}} \approx \frac{1}{c^2}(\Psi_{em} - \Psi_{obs}) \tag{2.28}$$

Lets considers a star emitting a wave, and assume (safely) that the gravitational field near the star is much more stronger near the Earth we have that $|\Psi_{em}| >> |\Psi_{obs}|$ and then $\Delta\nu << 0$. This implies that the observed spectral lines will be shifted to the lower frequency, otherwise the light spectrum will be shifted to the "red" zone. This effect, that is a direct result of gravitational time dilation, is called "Gravitational Refshif". The effect was predicted for the first time by John Michell in 1783, Pierre-Simon Laplace in 1796 and Johann Georg von Soldner (1801), which assumed that light could slow down and fall near a strong gravitational field like the one from a star. The correct effect was theorized by Einstein's 1911 and then confirmed by many experiments, were the first was Arthur Eddington's 1919 solar

eclipse expedition.

2.1.4 Shapiro time delay

During early 60s, I. Shapiro realized that according to GR, a light signal sent through the solar system should be delayed by the effect of the gravitational field of the Sun (or the planets) by a quantity proportional to the light bending factor ($\frac{1+\gamma}{2}$). This effect is measurable if the signal is reflected back to Earth.
Usually, time delays are more or less hundreds of microseconds. Using the Vikings like a radar transmitter it was possible to confirm GR at 0.1% level. Other measurements were made using radar reflection from other targets like Mariners and Voyager but the best one was made using Doppler tracking to Cassini spacecraft. This measure confirm GR at a level of 0.002%.
This test is also called the 4^{th} test of GR.

2.2 Parametrized Post-Newtonian formalism

Extensions of GR have been proposed, to compare theory and experiment. An approximation, known as the post-Newtonian limit, is adequately accurate to enclose most solar-system tests that can be performed nowadays. Although the existence of a long-range gravitational fields in addition to the metric in different metric theories of gravity, postulation of those theories request that matter and non-gravitational fields be completely unaware to them. The metric g is the only field that enters in the equations of motion. Any other field that can be contained in a theory can only generate the space-time curvature associated to the metric. The equations of motions and the metric for matter are the principal entities to calculate the observable effects, and all that distinguishes a metric theory by another is the particular way in which matter and other gravitational fields generate the metric, so the biggest difference among metrics is the numerical values of the coefficients that appear in front of the metric potentials. This PPN formalism inserts parameters in place of these coefficients, parameters whose values depend on the theory under study. In

the current version of the PPN formalism, ten parameters are used (see table 2.1).

Parameter	What it measures relative to GR	Value in GR	Value in PPN formalism
γ	How much spacecurvature produced by unit rest mass?	1	γ
β	How much "nonlinearity" in the superposition law for gravity?	1	β
ξ	Preferred-location effects?	0	ξ
α_1	Preferred-frame effects?	0	α_1
α_2		0	α_2
α_3		0	0
α_3	Violation of conservation of total momentum	0	0
ζ_1		0	0
ζ_2		0	0
ζ_3		0	0
ζ_4		0	0

Table 2.1: PPN parameters and their significance.

In this work the attention will be focused on parameters γ and β, used to describe classical tests of GR; they are the most important and the only nonzero parameters in GR.

Chapter 3

The SCF_Lab

The aim of this chapter is to describe the *SCF_Lab* with all its subsystems used for the MoonLIGHT-2 experimental tests. The *SCF_Lab* is an infrastructure built by INFN-LNF over the years for the ETRUSCO, MoonLIGHT and especially for the ETRUSCO-2 research programs. The laboratory is located inside an 85 m^2 class 10,000 Clean Room (ISO 7) and is operational with the SCF and the SCF-G Optical Ground Support Equipments (OGSEs). The clean room guarantee adequate condition for the tested optics avoiding any dust particle on the CCR that will decrease the test accuracy. The Laboratory has two separate entry areas for personnel and equipment. The rest of the lab is divided in two other areas, one for the SCF and one for the SCF-G and each part has the fundamental hardware to run the facility. Both of the facilities are designed to characterize in a simulated space environment (in terms of pressure and temperature) the thermal and optical properties of CCR (for LLR but also for SLR). In the operative phase each camera can reach a pressure around $10^{-6} mbar$ and a T_{shroud} around 90K. On the front side each facilities have a solar window in order to illuminate the payload inside the chamber with a Solar Simulator radiation AM0 outside the cryostat. Other two windows, an Infrared (IR) window and an optical window are placed on the right side of the cryostat for the thermal and optical tests respectively. The payload inside the chamber can be rotated by an external movement system (with a dedicated SW) in a way that can

be placed in front of one of three windows during the tests phases (see fig.3.1 for a schematic view).

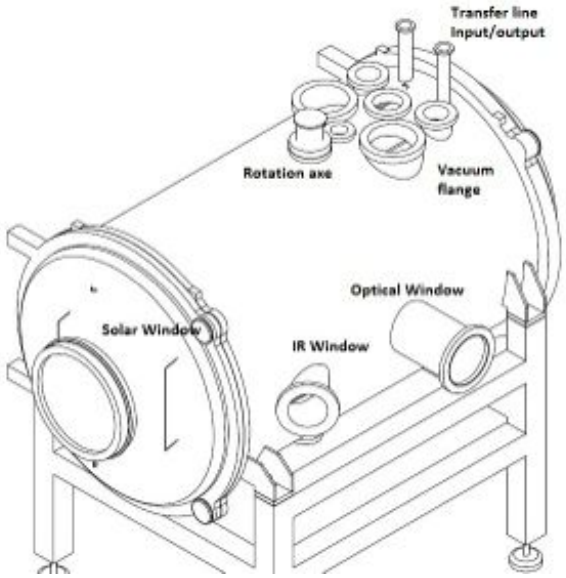

Figure 3.1: Schematic view of SCF-G facility with in evidence the main elements.

All MoonLIGHT-2 tests were carried out in the SCF-G, the subsystem involved can be schematically divided in:

- *SCF-G Crystat*: the facility used to test the CCR in a simulated space thermal environment
- *Vacuum and Cryogenic System*: the subsystem dedicated to reach the operative pressure and temperature conditions.
- *Control and acquisition electronics*: the subsystem dedicated at the data acquisition (invasive thermometry and vacuum reading), remote movement system control and payload temperature control
- *Solar Simulator*: the apparatus that reproduce the AM0 solar spectrum used during the test

- *IR Thermacam*: the subsystem used to take the IR pictures and then the SW package used to analyze them in order to obtain the CCR front face temperature

- *Optical Bench*: the subsystem composed by the optical elements used to reproduce the laser beam on the CCR and acquire the returning FFDP, along with the AccuFiz Fizeau Interferometer.

In the following sections we will describe all the SCF-G subsystem, with more detail for the ones more involved in the MoonLIGHT-2 tests phases.

3.1 SCF-G Cryostat

The SCF-G is composed by a base cylindrical steel cryostat, closed in its two terminal part by two steel spherical cap (fig.3.2a).

Inside the cryostat is placed a cylindrical copper shroud equipped with a cooling coil (painted with black Aeroglaze Z306) where the liquid nitrogen flow when the SCF-G is running. In the operative phase, when the LN2 is fully flowing inside the chamber the shroud reach temperature of 90±10K degree. The front spherical cap has a hole where is installed the quartz solar window (3.2b), inside the Solar Window Flange is installed a dedicated PT100 probe used to monitor the flange temperature when the Solar Simulator is turned on (see section 3.4). On the right side of the cryostat is installed a Germanium window (fig.3.2c) transparent to the Infrared Radiation, with 45° inclination with respect to the longitudinal axis, and a fused silica optical window (fig.3.2d). The shroud, including the two caps, is covered with COOLCAT 2 NW MLI (10 Layers) in order to ensure the thermal isolation from the external environment and reduce the LN2 consumption. On the shroud are installed two different PT100 probes circuits for temperature control, each circuit has 24 probes. In addition on the shroud are also installed a series of Resistive Kapton Heaters tapes, remotely controlled by a dedicated SW, in order to increase rapidly the shroud temperature from 90K to 300K and return in air

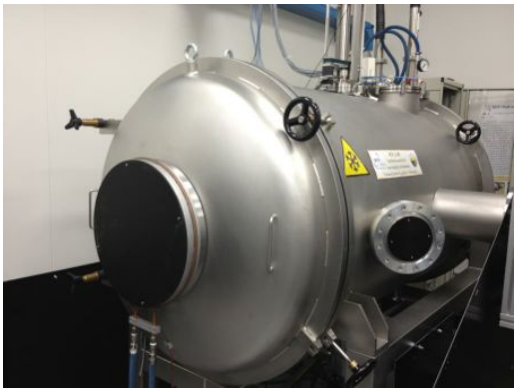

(a) *The SCF-G cryostat with the front spherical cap.*

(b) *Solar window.*

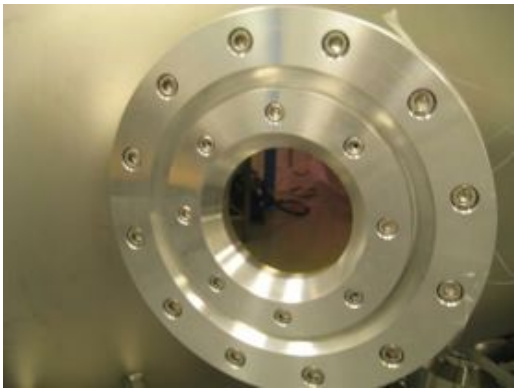

(c) *IR window.*

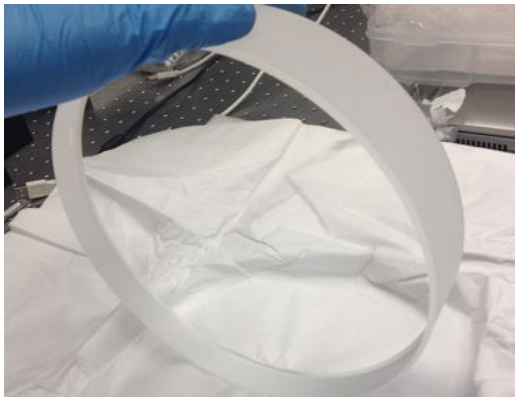

(d) *Optical window.*

Figure 3.2: The external view (front) of the SCF-G, with the three windows in details

conditions (section 3.3). The upper side of the cryostat is provided with a series of vacuum flange (see fig.3.1) (corresponding at holes in the upper side of the shroud) for the control and reading of PT100 and the other electronics inside the chamber, see section 3.3 for detail about the movement and thermal probes acquisition system. The rotation axis (fig.3.5b) of movement system (fig.3.1) is directly connected to a vertical bar through an hole in the upper section on the shroud , inside the cryostat, where MoonLIGHT-2 is hooked; on the axis is installed a potentiometer (see section 3.3 for details) and can be rotated by the external movement system in order to

SCF-G element	dimensions
Steel Cylinder height (from ground)	1036mm
Steel Cylinder diameter	1036mm
Steel Cylinder length	1020mm
Solar window diameter	370mm
IR window diameter	80mm
Optical window diameter	230mm

Table 3.1: SCF-G dimensions summarized

place the payload facing one of the windows. In table 3.1 are reported the details about the dimensions of the cryostat and the windows.

3.2 Vacuum & Cryogenic System

The SCF-G vacuum system is composed by two different pumps:

- Oil rotative pump (3.3a): The pump is located outside the clean room and it is used for the pre-vacuum phase and in backing pumping mode for the turbomolecular pump. The rotative pump is connected at the cryostat between two different valves: "rough" and "fine". The "rough valve" is used to connect directly the camera with the pump, in this way it is possible to achieve the pre-vacuum condition and reach a pressure around $10^{-1} mbar$. The "fine valve" is used to put the rotative pump in backing pump with the turbomolecular pump (the "rough" valve must be closed in order to switch safely in this state). Between the rotative pump and the cryostat, outside the clean room, is placed a cold vacuum trap, in order to avoid that any oil particles goes inside the chamber.

- Turbo molecular pump (3.3b): The pump is located inside the clean room, directly below the SCF-G and is connected to the chamber between the "Gate"

valve. The pump is used to reach the hight vacuum condition, at least $10^{-6}mbar$; when the pre-vacuum condition are reached ($10^{-1}mbar$), the "rough" valve is closed and then the "fine" and the "gate" valves are opened.

(a) *The Oil rotative pump.* **(b)** *The Turbo molecular pump.*

Figure 3.3: The two SCF-G pumps

All the valves used are electronics type, manually controlled with knobs placed on the control box (fig.3.4a), placed in front of the SCF-G. Inside the control box there is a vacuum sensor reader (fig.3.4b) that report the pressure (in mbar) inside the chamber acquired by a sensor. The pressure value is then acquired also by the data acquisition system and digitally stored, see section 3.3 for details.

When the camera is at the operative pressure of ($10^{-6}mbar$), the LN2 cryogenic system can start its work and take the shroud at 90K. The LN2 tank is placed outside the *SCF_Lab*, near the "Gran Sasso" warehouse at LNF (fig.3.5a). Once the valve is opened the LN2 begins to flow inside the shroud through the transfer line. The LN2 flux can be remotely controlled with an external fluxmeter with a specific LabVIEW SW (fig.3.5c) called Virtual Instrument (vi). The LN2 flow start form the outside tank trough a secure valve, then across the first line of the transfer line (around 40m) and finally goes inside the cryostat. Then the LN2 cools the shroud and then goes out the cryostat across the second line of transfer line (around 20m), that take it outside from the *SCF_Lab*. In this second line there are in series;

(a) *The SCF-G Control Box controls for electro-valves.*

(b) *The vacuum sensor reader.*

Figure 3.4: The SCF-G control box

an heating pipe that heat up the LN2, the Fluxmeter (located outside the Lab, after the tank and before the SCF-G) and an exchanger that transform the liquid LN2 in its gaseous phase and free it in the environment outside the laboratory. The fluxmeter can control the LN2 in two modes:

- analog: in this mode the user must set a LN2 flux setpoint, between 0 and 400 l/min, with the specific LabVIEW SW by *SCF_Lab* team. (see section 3.3)

- digital: in this mode the user must choose between the "valve open" configuration, where the fluxmeter control is turned off and all the LN2 goes inside the SCF-G, and "valve closed" where the fluxmeter deflect all the LN2 on the heater exchanger.

In input at the fluxmeter is placed a PT100 probe, readed by the cFP (see section 3.3) in order to control the temperature and avoid any freeze at the fluxmeter. Starting from air condition ($pressure = 10^3 mbar$ and $T_{shroud} = 300K$) the vacuum phase takes around 1.5 hours to reach the operative conditions while the cryogenic phase takes another 1 hour.

(a) *The LN2 tank.*

(b) *The rotation axis with the potentiometer installed.*

(c) *The LN2 Fluxmeter.*

Figure 3.5: The LN2 system

3.3 Control and acquisition electronics

The control and acquisition electronics subsystem include all the SW (developed with LabVIEW of National Instrument by *SCF_Lab* team) used to monitor and control MoonLIGHT-2 and the related instrumentation during the test phases.

Schematically during a standard test in the *SCF_Lab* the Control and acquisition electronics must provide the control of movement and payload heating system and the acquiring of the chamber vacuum pressure within the temperature probes (the ones from the shroud plus the ones installed on the payload). The most important vi's used during the test are reported in fig.3.6 and can be divided in three different category:

- Temperature data acquisition system and fluxmeter control.
- Payload and shroud heaters remote control.
- Movement system control.

- *Temperature data acquisition system:* On the shroud are installed two different PT100 probes circuits, each one with 24 probes, in addition other probes are installed on the payload in test phases (for MoonLIGHT-2 there are installed other 6 probes, see chapter 5 for details). All of these probes are connected to the PC with a NI (National Instrument) cFP (compact Field Point) 2220. Also the fluxmeter temperature reading probe along with the probe on the solar window (see section 3.1 and 3.4) are connected to the cFP 2220. The vacuum pressure reader and a custom board for the fluxmeter analog control are connected to cFP respectively with a serial connection and a DAO (Digital Analog Input/Output) module. Finally the cFP 2220 is connected to the PC with an ethernet connection and two different dedicated LabVIEW SW, the acquisition and the fluxmeter program, acquire and control all of these elements in "real time". With the acquisition program all the temperature and pressure data are automatically saved in the cFP internal memory. In fig.3.6a is shown the acquisition.vi where all the temperature probes along with the pressure value are acquired, plotted and saved; while fig.3.6b shows the fluxmeter.vi which is possible control the fluxmeter and read the temperature probe.
- *Payload and shroud heaters remote control:*Referring to section 3.1, on the shroud are installed a series of resistive Kapton Heaters tape in order to rapidly increase the shroud temperature from 90K to 300K and return in "air" conditions. The heater power supply is connected with the PC with a Can-ethernet interface and is

controlled by a dedicated SW. In addition, in order to ensure the MoonLIGHT-2 thermal control, two resistive heater tapes (with two wires configuration) are installed on its housing. Each heater is connected with a power supply. The power supply are connected, with a custom electronic circuit, at the DAO cFP module and controlled with a dedicated LabVIEW vi, (fig.3.6c). The vi allow the user to choose, for each power supply (and so each heater tape on MoonLIGHT-2), two different work mode:
Automatic: the user set the housing setpoint temperature and the program automatically control the chosen power supply in order to reach the desired temperature. In this mode the vi read the housing average temperature (with the dedicated probes) and put this temperature in feedback with the setpoint value, then using a specific PID (Proportional-Integral-Derivative) control the program choose the right current for the heater tape. Using the automatic mode with this program, is possible to reach the desired housing average temperature within an error of $\pm 1K$, where the probes accuracy is about $\pm 0.2 - 0.5K$ (depending on the working temperature).
Manual: the user set manually the desired current for the specific heater tape.
- *Movement system control:* The movement system allow the payload rotation on its axis of more than 280°, starting from payload facing the cool shield ($-90°$ with respect to the payload facing the solar window) until to the payload faces the optical window (90° with respect to the payload facing the solar window). The movement motor is a step-step motor, located above the SCF-G vacuum chamber, while the motor controller dedicated is the Pollux-NT, located inside the SCF-G control box. The controller is connected to the PC with a serial-ethernet connection. In addition a potentiometer is installed on the external rotation axis (fig.3.5b). The potentiometer allow to read the absolute position of the rotation axis (hence the position of MoonLIGHT-2 inside the chamber), regardless the control Pollux reading. In this way the user can always obtain an absolute position reading even if the electrical supply of the Pollux controller if cut off. The signal coming from the potentiometer is acquired by an "Arduino UNO R3" logic board, sent to Arduino Ethernet Shield and then to the PC with an ethernet switch. The movement system vi (fig.3.6d) is connected with the Pollux controller and Arduino UNO allowing the full control

of the movement system; the user can rotate the payload manually, choosing between a relative movement from the last position or an absolute rotation from the "zero" value, or set pre-defined position. A set of indicators report the status of the movement system (if it is moving or not), the actual position acquired by the controller along with the position acquired by the potentiometer, and eventually the limit status that define the "zero" value for the absolute movement.

3.4 Solar Simulator

The SCF-G Solar Simulator (fig.3.7a), provided by TS Space Systems LTD, is a class A Solar Simulator made out of the following elements:

- a metal halides lamp, capable to emit a radiation equal to the solar constant ($\sim 1.4kW/m^2$)
- a mask of optical filters placed in front of the lamp used to match the output spectrum lamp with the real solar spectrum. The mask is composed by 5 shaded and 44 unshaded filters, for 49 filters in total each one with dimensions around 5x5cm, placed in a holder with the scheme reported in fig.3.7b.
- a shutter which is manually controlled by an air compressed system which gives the possibility of interrupting the beam during the tests without turning off the simulator.

The Solar Simulator is provided with a dedicated control box, that use an internal SW automatically put the lamp in the maximum output power conditions (50V and 115A, equal to around 95% of its maximum power), the automatic start up procedure takes around 30 minutes. In addition the control box acquires the temperature from a dedicated PT100 probe, placed inside the Solar Simulator on the filters holder, to monitor the internal temperature avoiding any overheating and turning off the simulator if the internal temperature exceeds 80°C.

(a) *The acquisition probes (PT100) and pressure reading .vi.*

(b) *The LN2 Fluxmeter control .vi.*

(c) *The paylolad heaters control .vi.*

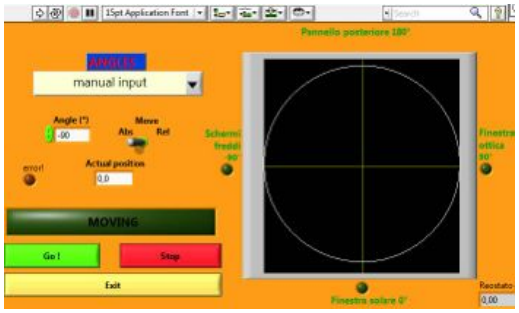

(d) *The rotation system movement control .vi.*

Figure 3.6: The SCF-G data acquisition system with the front panel of the main used program

(a) *Internal view of the SCF-G Solar Simulator. On the left side there is the metal halides lamp, on the right side the filters.*

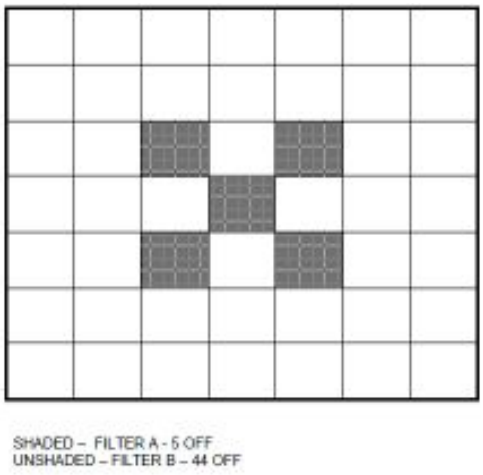

(b) *The Solar Simulator filters scheme.*

Figure 3.7: The SCF-G Solar Simulator, internal hardware and filters scheme

The distance between the lamp and the opening, along with the Simulator itself structure are designed in order to obtain three different features at the MoonLIGHT-2 distance (1.1 m from the shutter):

- The beam divergence allows the illumination of 420 mm diameter surface.
- A close match with the AM0 (Air Mass 0) spectrum. The AM0 is defined as the Solar Spectrum, outside the Earth atmosphere in the interval 400-3000 nm. Fig.3.8 shows the SCF-G Solar Simulator spectrum with respect to the AM0 standard spectrum, along with the values for each band recorded during the Solar Simulator validation test.

- The output beam uniformity is ±5% inside a circle surface with 350 mm diameter. The measured uniformity during the calibration phase before the MoonLIGHT-2 test is ±3.12% with a central beam intensity of $1474.65 W/m^2$, respecting the solar constant value.

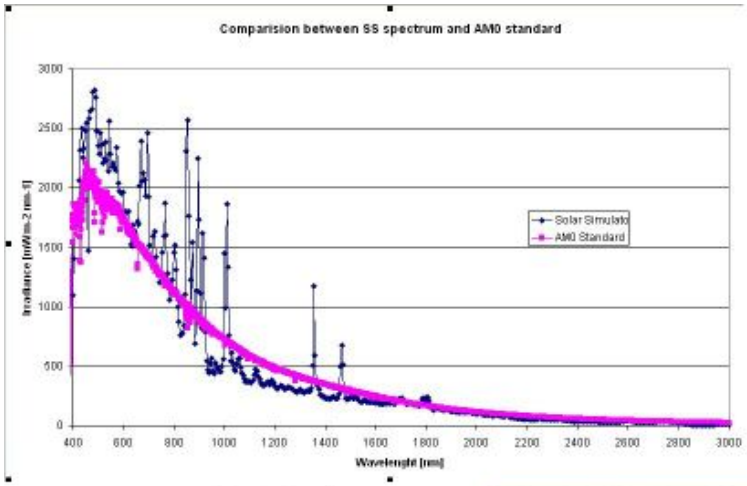

Band [nm]	AM.15 %distribution	Spectrum Integral over the range [W/m^2]	% distribution and Class Rating	Class A Upper Limit %	Class A Lower Limit %	Inside the Range
400-500	18.4	226316	21.75071768	23	13.8	Yes
500-600	19.9	221659	21.30314397	24.875	14.925	Yes
600-700	18.4	185630	17.84047846	23	13.8	Yes
700-800	14.9	140804	13.53235323	18.625	11.175	Yes
800-900	12.5	129909	12.48525948	15.625	9.375	Yes
900-1100	15.9	136179	13.08785496	19.875	11.925	Yes

Figure 3.8: The Solar Simulator spectrum w.r.t. the AM0 spectrum.

All of these features allow the Solar Simulator to reproduce closely the real Sun illumination present on the Moon, in terms of uniformity and spectrum, during the test phases.

3.5 IR Thermacam

The InfraRed Thermacam subsystem is composed of:

- The FLIR Thermacam (fig.3.9)
- The FLIR Researcher SW

The FLIR Thermcam, is a digital camera with a CCD designed to operate in the spectrum range 7.5-10 μm, corresponding to the far infrared radiation spectrum. The camera is provided of an automatic electronic zoom and its accuracy is $\pm$2K for single spot, or $\pm$2% reading with a thermal sensitivity $\leq$ 0.02°C at 30°C. The Thermacam takes IR pictures with a resolution of 640x480 pixels (see fig.3.10 for an example of MoonLIGHT-2 IR picture taken during one of the experimental tests).

Figure 3.9: The SCF-G FLIR Thermacam.

Processing the picture with the dedicated FLIR Researcher SW provided by the camera producer, it is possible to measure the temperature of a specific spot with known emissivity once having defined: environment temperature and humidity, distance between spot on the object and camera, and reflected apparent temperature.

Assuming that in vacuum the umidity is equal to 0, so the distance parameter is useless because there is no absorption/emissivity in IR range from the air O_2 molecule, the reflected apparent temperature is the key element used to calibrate the camera. In order to obtain the absolute object temperature we must solve the general equation 3.1;

$$W_{tot} = W_{obj} + W_{ref} \tag{3.1}$$

The equation 3.1 states that the total radiation collected by the camera is the sum of the radiation emitted by the analyzed object (interested signal), and the environment radiation reflected by the object to the camera (the noise background signal). In the approximation that in vacuum the only thermal exchange possible is a radiative type we can express the equation 3.1 with:

$$W_{tot} = A_{obj} \cdot \sigma \cdot \epsilon_{obj} \cdot (T_{obj}^4 - T_{env}^4) + A_{obj} \cdot \sigma \cdot (1 - \epsilon_{obj}) \cdot (T_{ref}^4 - T_{env}^4) \tag{3.2}$$

where:

- W_{tot} is total IR radiation acquired by the IR camera
- W_{obj} is the total IR radiation emitted by the object at temperature T_{obj} with emissivity ϵ_{obj}
- W_{ref} is IR radiation emitted by the environment and reflected by the object to the camera. In order to simplify the problem the environment radiation is approximated as a black body radiation with temperature T_{env}
- σ is the Stefan-Boltzmann constant; $\sigma = 5.67 \cdot 10^{-8}$ W/m^2 K^4
- A_{obj} is the object surface, in the approximation that (for the IR camera point of view) the object emissive area is equal to the reflective area.
- T_{env} is the environment (shroud) temperature, 90K average value.

So the mandatory requirement to obtain the object temperature is to measure the reflected temperature and remove it from the total radiation collected. So knowing the background radiation from T_{ref} we obtain W_{obj} and hence T_{obj} solving equation 3.2 in 3.3.

$$T_{obj} = \sqrt[4]{\frac{1}{\epsilon_{obj}} \cdot \left[\frac{W_{tot}}{A_{obj} \cdot \sigma} - (1 - \epsilon_{obj}) \cdot (T_{ref}^4 - T_{env}^4) \right] + T_{env}^4} \tag{3.3}$$

This procedure is automatically carried out by the FLIR Researcher SW once the user set manually the reflected apparent temperature or T_{ref}. To obtain the reflected apparent temperature the user must: first set a spot in a place with known temperature and emissivity (for example a Kapton tape near a PT100 probe acquired by acquisition vi) then find the right reflected apparent temperature which give a T_{obj} equal to the temperature read by the PT100. Finally setting the just obtained reflected apparent temperature the FLIR SW will provide the temperature of any object in the IR picture with known emissivity (in our case we obtain the MoonLIGHT-2 front face CCR temperature). With the FLIR Researcher SW it is possible to obtain the temperature of a single spot or the average temperature of an area, see chapter 5 for MoonLIGHT-2 detailed thermal analysis. During the operative phases the Thermacam is placed on a tripod in front of the Germanium IR window with emissivity equal to 0.97 and can take IR pictures programmatically with a user defined time span (typically 1-2 minutes for MoonLIGHT-2). It is important to underline that the Thermacam is used mainly as an instrument for differential measurement temperature. The main goal during the test is to obtain the CCR thermal constant (see chapter 5 for test details) and in this way the test results are independent from the calibration that provides only the CCR front face absolute temperature.

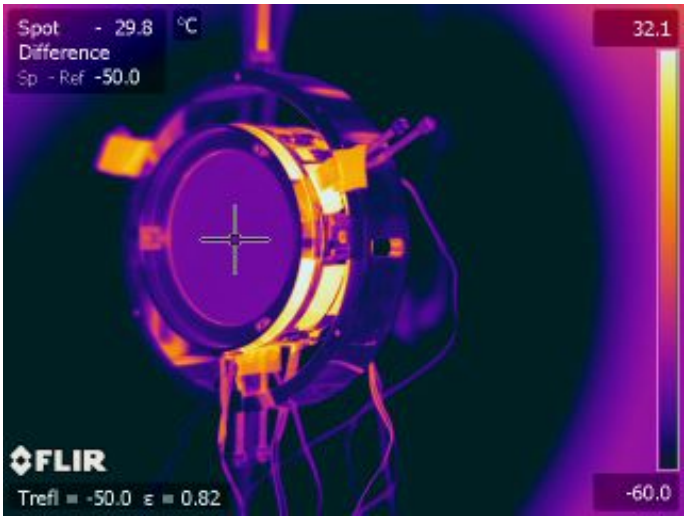

Figure 3.10: A sample of an IR picture of MoonLIGHT-2 with FLIR Thermacam, **the picture is not calibrated**.

3.6 Optical layout

In this section we will focus our attention on the optical bench layout used to simulate the laser ranging procedure. The optical circuit has a huge variety of components (see fig.3.11).

The basic industrial acceptance test of a CCR optical performance is the measurement of the absolute angular size, shape and optical cross section of single-CCR FFDP with linearly polarized continuous wave lasers.
The horizontal and vertical polarization components of each FFDP are recorded separately. This is particularly important for uncoated CCR, whose FFDP have a strong dependency on the orientation of the input linear polarization. No dependency is expected for coated CCR. Our laser beam profilers are two 12-bit, 2 Mega-pixel CCD cameras read-out through Firewire or USB with a PC. FFDPs are acquired with the CCR in Air and Isothermal Conditions (AIC). The absolute angular scale of the optical circuit is calibrated with the double-slit method to test the consistency of each CCR FFDP with its nominal DAO expressed in arcsec. The

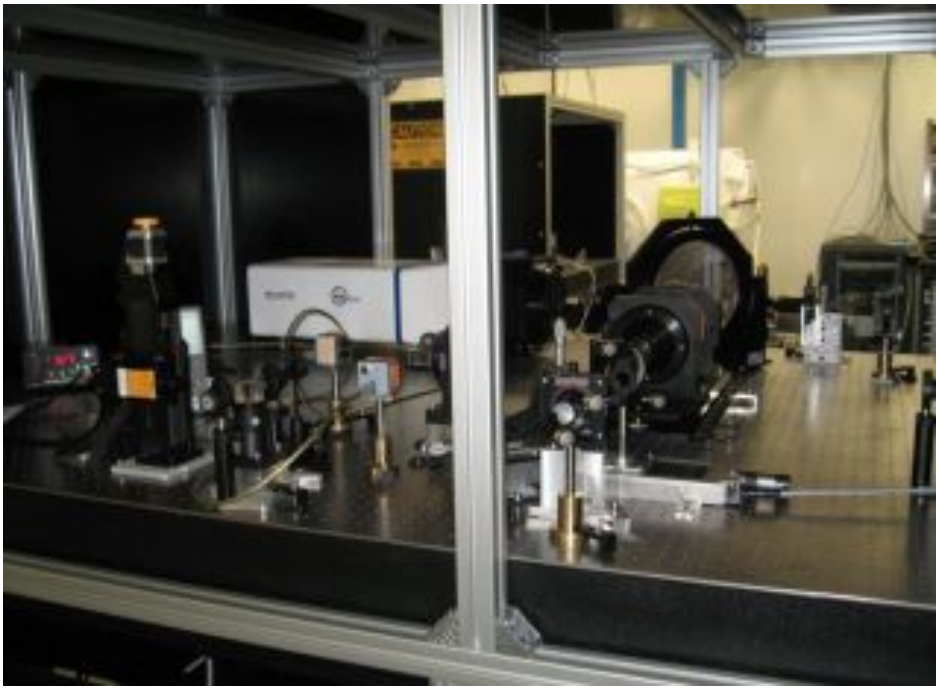

Figure 3.11: Picture of the optical bench

latter are related to the satellite velocity aberration, which is determined by its orbital altitude (velocity). The lack of knowledge of the DAO specifications makes the modeling of the optical FFDP and, especially, its variations due to thermal effects, extremely difficult and unreliable. We also measured the FFDP intensity relative to the Airy Peak, using reference flat mirrors of known reflectivity and good optical quality. FFDP measurements were modeled with CodeV, an optical ray-tracing software package by O.R.A., Inc. The DAO are strictly related to the satellite and lunar velocity aberration, fig 3.12, which is in turn determined by its orbital altitude.

The problem is referred to the relative movement of the CCR, on the satellite or on the Moon, round the Earth during the laser pulse time of flight. The study of the FFDP is necessary to understand in which place the laser pulse retroreflected by the CCR will reach the starting station, where the CCD is able to catch the incoming photons.

The velocity aberration for the Moon is about 4 μrad. In this case the best choice

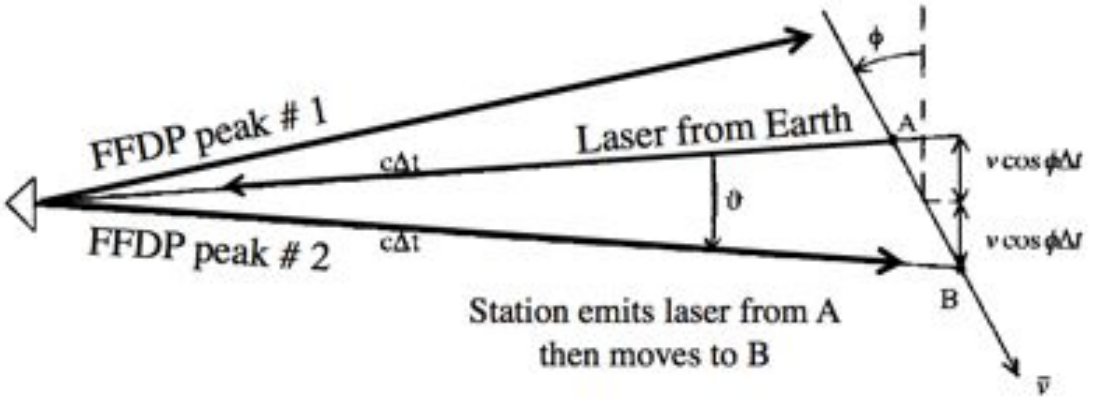

Figure 3.12: Velocity aberration

is a 0,0", 0.0", 0.0" (in arcsec) dihedral angle offset, because in the FFDP space is located in the central peak. The velocity aberration for the altitudes of Global Navigation Satellite System constellations is 20-25 μrad.

3.6.1 Angular calibration

The CCD angular calibration is necessary to convert the pixel reference system to a microradians reference system, in this way we have the absolute angular scale of the optical circuit. In order to do this, we use the Young experiment (the double-slit method). Using a double-slit we want to create a pattern, characterized by a sequence of peaks with known angular distance, fig.3.13.

The double slit produces a similar single slit figure with visible interference fringes inside the diffraction maximums. The distance between the fringes of the diffraction pattern follows the formula:

$$sin\theta_j = j\frac{\lambda}{d} \tag{3.4}$$

Where $\theta_j$is the angle where we can find the j-th fringe; λ is the laser wavelength and d is the slit distance. With small angles, the angular distance between two fringes

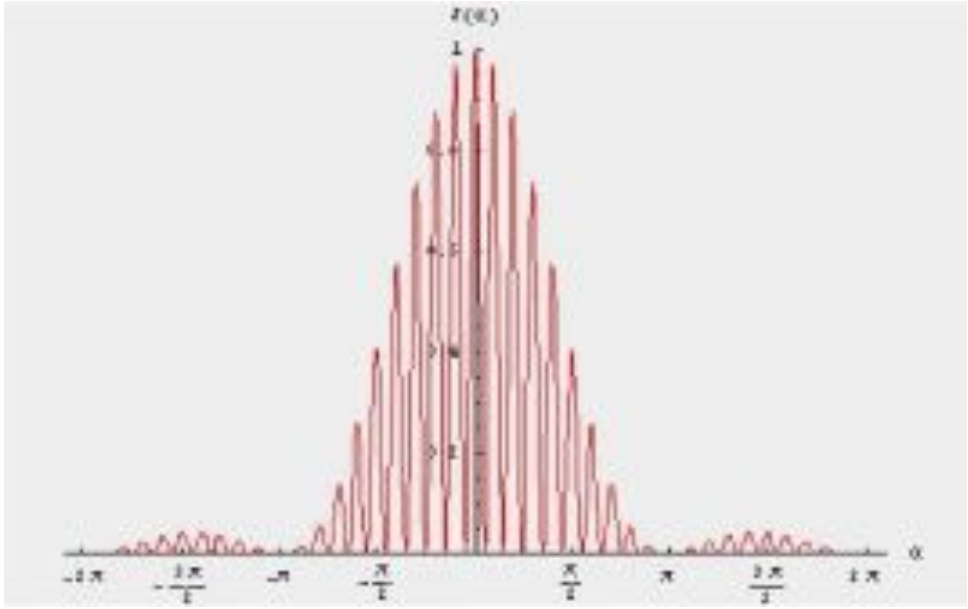

Figure 3.13: Peaks of interference for a double slit

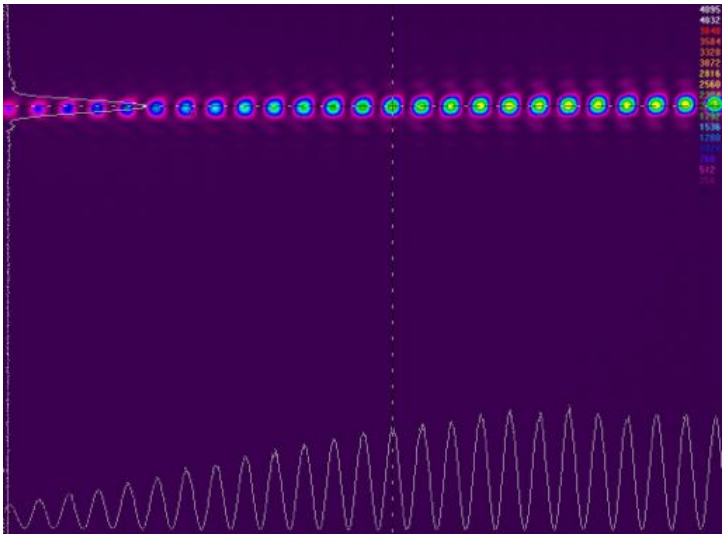

Figure 3.14: Pattern obtained with double slit

is equal to the difference of $\theta_{j+1} - \theta_j$, so we have:

$$\theta = \frac{\lambda}{d} \tag{3.5}$$

Where θ is the distance between two peaks. Using out layout we can measure peaks distance as 36 pixels (see fig.3.14). Thus by an easy pixels vs distance comparison we can conclude that $65\mu rad$ corresponds approximately to 36 pixels obtained with our circuit[1].

Interferometer

In the framework of MoonLIGHT-2 project, we improve the quality of our optical bench with an AccuFiz wavefront interferometer. Thanks to this new device, we are able to test the optical quality of every component of the circuit and most important, we can make very precise measurements of DAO of our CCR not only in air condition, but also during every phase of the SCF-Test.

[1]The distance between our slits is d=8.2 mm. So we have $\frac{\lambda}{d} = 65\mu rad$.

Chapter 4

The MoonLIGHT-2 experiment

This section describes MoonLIGHT-2 design, briefly illustrating its evolution and reporting the most important requirements used to constrain the structure of CCR and housing. In the first section, 4.1, the first MoonLIGHT project (named MoonLIGHT-International Lunar Network (ILN)) will be described along with a summary of the main test results carried out. MoonLIGHT-ILN was always an INFN-LNF project started in 2006 and concluded in 2010 with an extensive test campaign, and today MoonLIGHT-ILN is the base project used for MoonLIGHT-2 development. The second part of this chapter (section 4.2) will describe the optical part of MoonLIGHT-2 design, starting with the optical simulation (4.2.1) carried out by the SCF_Lab team in parallel with the tests to study the payload optical response, concluding with the Big CCR specifics (subsection 4.2.1), the core element of MoonLIGHT-2. The third part of the chapter will be focused on the structural part of the design 4.3, starting with a preliminary General Relativity test study in order to choose a design with or without the sunshade (subsection 4.3.1), and then discussing about the structural requirement needed for the launch with the Falcon-9 vector (with Moon Express mission in 2017) (subsection 4.3.2). Finally the subsection 4.3.3 will describe the actual structural MoonLIGHT-2 design, the same used for the test campaign in chapter 5. Along with MoonLIGHT-2 another device that the mission Moon Express will deploy on the Moon is INstrument for landing-Roving laser ranging/altimetry

Retroreflector Investigations (INRRI), a small and light (less then 30g) retroreflector payload used for altimetry and selenodesy. The section 4.4 will describe the INRRI structure and specifics.

4.1 MoonLIGHT-ILN

In this section we will describe the MoonLIGHT/Lunar Laser RetroReflector for the 21^{st} Century (LLRRA21) (experiment of INFN-CSN5). This project started in 2006 and its main purpose is to improve gravity tests and lunar science measurements [1]. This project was the result of the collaboration between two teams: one in the USA, led by Douglas Currie of the University of Maryland, and one in Italy led by INFN-LNF. We are exploring improvements both in the instrumentation and in the modeling of the CCR.
First of all, it is important to understand the limitation of arrays with a multi-CCR structure located on the lunar surface (cfr 1.3). The main problem that affects the Apollo arrays is due to lunar librations, in longitude, that result from the eccentricity of the Moon's orbit around the Earth. During the 28 days lunar phase, the Moon's rotation alternatively leads and lags its orbital position, of about 8 degree. Due to this phenomenon the Apollo arrays are moved so that one corner of the array is more distant than the opposite corner by several centimeters. Because of the libration tilt, the arrays increase the dimension of the pulse coming back to the Earth (fig.4.1). The broadening of the pulse will be greater proportionally to the array physical dimensions and to the Moon-Earth distance increase (in the position in which the libration phenomena are at the peak). Therefore for the Apollo 15 array the enlargement is about 30 cm, on the other hand is about 15 cm for Apollo 11 and Apollo 14 arrays. In agreement with this relationship, the pulse enlargement corresponds to a time of flight increase:

- $\pm$ 0.5 nanoseconds for Apollo 15;
- $\pm$ 0.25 nanoseconds for Apollo 11 and Apollo 14.

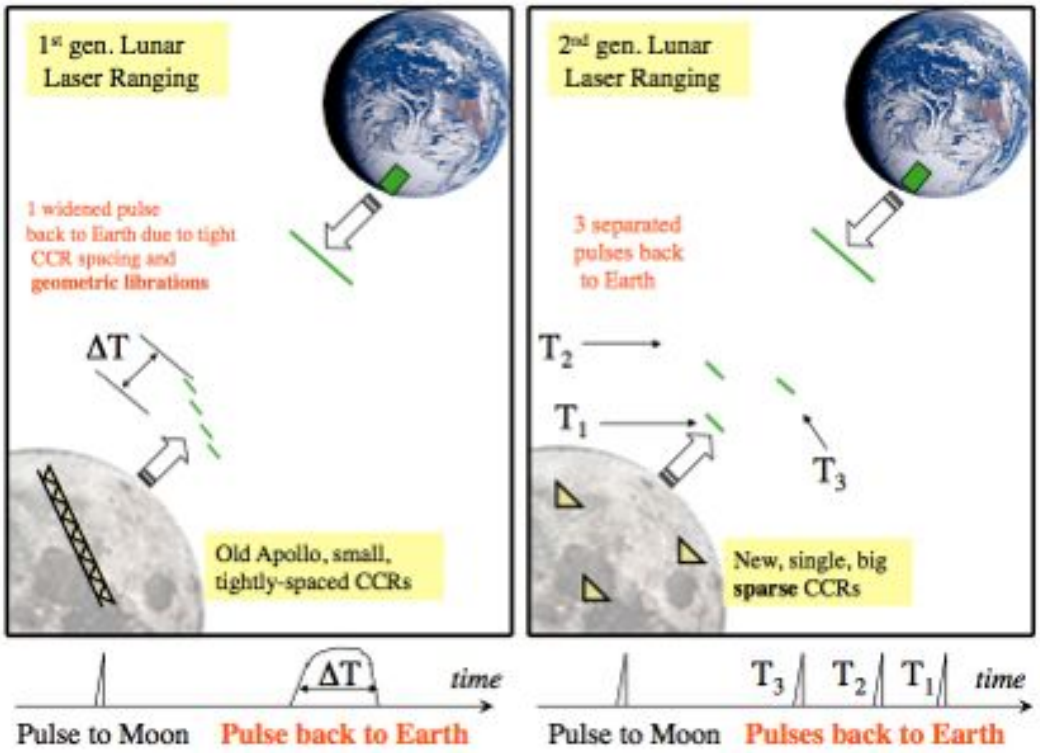

Figure 4.1: Comparison between 1^{st} and 2^{nd} generation LRAs. The librations tilt the arrays on the left, but the single big CCRs are unaffected, on the right. So we have single short pulses coming back.

So the accuracy of the ranging measurements cannot go below few centimeters (for a single normal point). Without hardware improvement, one can only progress by timing an extremely large number of single photoelectron returns to reduce the errors by the root mean square of the single photoelectron measurement error (cfr 1.2).

In order to solve this problem, the SCF group, in collaboration with the University of Maryland, indicates a new design of lunar CCR, named the 2^{nd} generation LLR, whose performance is unaffected not only by lunar librations, but also by regolith motion, due to its very large thermal cycle. The idea that we propose is to move from an array of multiple-small-CCRs, everyone with 3.8 cm of front face diameter,

to a series of single big CCRs, each with 10.0 cm of front face diameter, deployed separately on the lunar surface (fig.1.6).
Instead of having a single pulse, spread by the array and the libration effect, we will have single short pulses coming back with the same dimensions as the incoming one (fig. 4.1), with a final LRA ranging accuracy below 10 μm. When the new CCRs will be placed on the lunar surface, improving the stations capabilities will make sense.

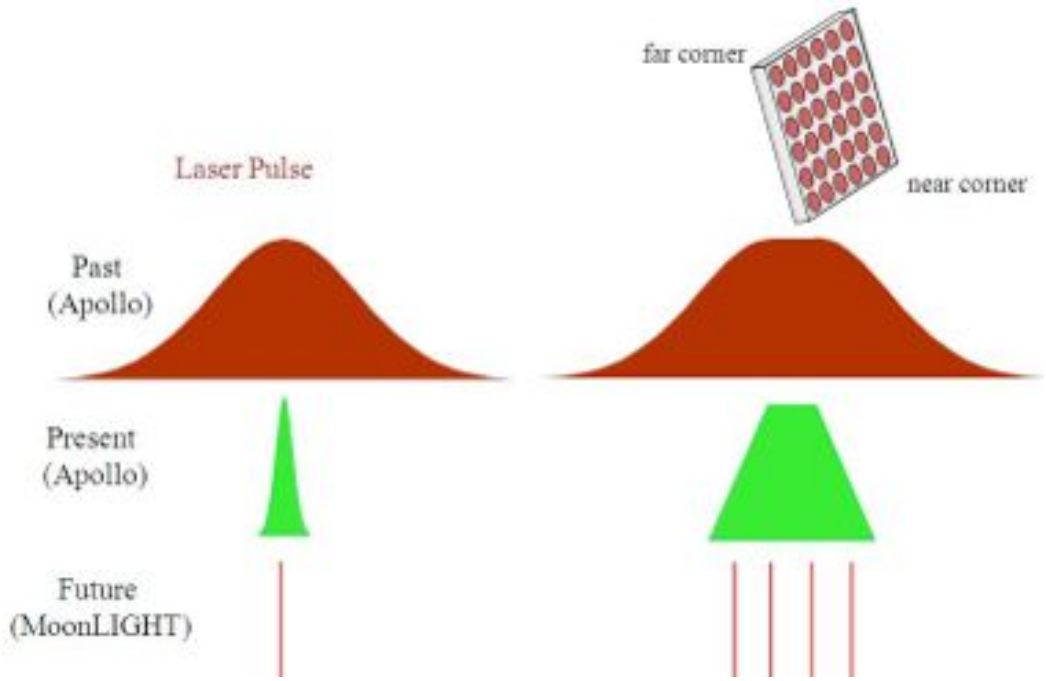

Figure 4.2: The figure shows the measurement uncertainty between laser pulse size fired and retroreflected; how the situation was in the past (on the top); how it is currently (in the middle) and the future possible situation with MoonLIGHT/LLRRA21 CCR (on the bottom).

To summarize, in the past there was a large laser pulse fired from the Earth station, bigger than the dimensions of the array, that dominated the measurement uncertainty. Now there is average size laser pulse , but still large array, so

that the measurement uncertainty is dominated by the array; in the future, with MoonLIGHT/LLRRA21, there will be a single CCR unaffected by librations. The measurement uncertainty will be dominated by the laser pulse, but the modern technology can do shorter laser pulses (fig. 4.2). In order to improve the ranging measurement it is fundamental to investigate the technical and fabrication challenges of MoonLIGHT/LLRRA21, through thermal/optical simulations and vacuum chamber tests performed at the INFN-LNF SCF_Lab. Besides the simulations, the SCF_Lab team, performed thermal and optical vacuum chamber tests to further validate the design issues.

4.2 MoonLIGHT-2 payload

The big solo retroreflector is the core element in the MoonLIGHT-2 project. Its dimensions, material and housing structure must guarantee an adequate light-return from the Moon, also avoiding any Lunar Libration issue, minimizing thermal effects that could affect its optical intensity level. Subsection 4.2.1 will describe the main characteristics of this CCR, chosen through optical simulations, and some of the main performance under thermal stress, while subsection 4.3 will describe the details of the structural design of MoonLIGHT-2.

4.2.1 Optical modeling

A laser beam sent by a ground station to a retroreflector in space, on the Moon in our case, is reflected back to the Earth as a diffracted beam. The intensity distribution of this beam, as seen on a screen in the far field, depends on the optical properties of the retroreflector, its material, dimensions and dihedral angle offsets. However the optical response of the retroreflector captured at the ground station (number of photons), depends also on some environmental factors, the relative motion with respect to the ground station, the Velocity Aberration (VA), orientation of the laser beam on the front face of the retroreflector and the characteristics of the laser beam, its wavelength and polarization. We developed a simulation architecture with the

use of an optical commercial software, CodeV, to determine the basic dimensional and optical characteristics of the MoonLIGHT retroreflector, analyzing the variation of its optical response under different conditions, mechanical and environmental. Some of the basic elements of the simulations were though fixed, because of common knowledge or constrained by technology.

Optimization of the retroreflector

MoonLIGHT-2 retroreflector inherits its basic characteristics from Apollo retroreflectors, it is an uncoated prism of Suprasil 311, a particular grade of Fused Silica. It has a circular front face aperture of $100\,mm$ and an apex length of $72.4\,mm$. The objective is to have a retroreflector whose optical response is of the same level of half of the Apollo15 array, as it is nowadays. Dimensions were not part of the optimization process due to technological/budget restrictions, meaning the capacity to build such a big prism of fused silica with proper optical quality at contained costs. In particular the optical quality is a big constraint since, as will be shown later in this section, increasing dimensions of retroreflectors enhance wavefront distortions due to space environment. For the simulations we used a green laser beam at $532\,nm$ wavelength, since the majority of existing laser ranging systems uses this wavelength.
Another datum for the simulations was the angular position where to evaluate the optical response of the retroreflector in the FFDP image domain, VA. The relative movement between the satellite, the Moon in this case, and the ground station induces a shift in the FFDP domain. The optical response must be calculated at a certain angular distance from the center corresponding to this relative movement. For a generic satellite orbiting around the Earth this shift could be in any direction from the center, but for the Moon this is not the case; in fact as described in 3.6 the VA in not evenly distributed in the FFDP plane and is off-centered to the right in this plane (as will be shown later in this section). The latitude of the laser ranging station is important in the calculation of the VA, since it contributes in the calculation with its rotational velocity. Active lunar laser ranging stations are quite a

few and concentrated in the northern hemisphere. The following table summarizes information for those stations as well as future or inactive stations.

LLR Station	Latitude [°]	VA Moon [μrad]
Active		
APOLLO	$32.78N$	4.18
Matera	$40.65N$	4.44
Grasse	$43.75N$	4.55
McDonald	$30.68N$	4.12
Future or inactive		
Wetzell	$49.14N$	4.76
Mount Stromlo	$35.32S$	4.26
Hartebeesthoek	$25.89S$	4.00

Table 4.1: Latitude and VA for LLR Stations

Looking at data in this table we decided, for simplicity to evaluate the optical response in the range $4.0 \div 4.5\,\mu rad$ on an horizontal segment on the right of the FFDP domain.
Those described till here are the basic assumption made for the simulations. For this kind of CCR, in the condition of a physical edge vertical and an horizontal polarized beam, the FFDP is like the one in Fig. 4.3

To calculate the optimum response from this type of retroreflector three parameters contribute to change the intensity of the FFDP in the chosen VA range.
One common technique to move energy in the FFDP plane is to introduce DAO. DAO is defined as a deviation of the angle between the reflecting faces. In a retroreflector three DAOs can be set. Since we are concentrated in the optical response in the specific range shown in Fig. 4.3, we discarded the option where three DAOs are set, because the intensity is broadened in every direction. When simulating the effect of two DAOs, those are set to be equal. We varied DAOs in the range $[-1; 1]$ arcsec with 0.1 arcsec step.

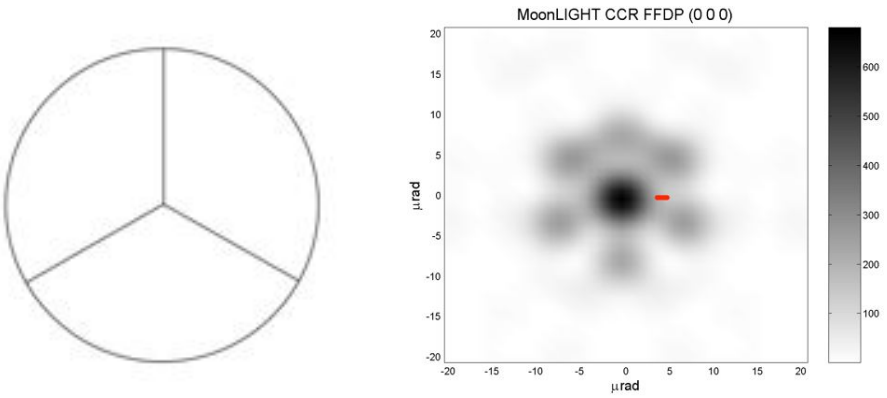

Figure 4.3: on left: Reference 0° orientation for simulated CCR.FFDP of a perfect uncoated retroreflector with physical edge vertical and horizontal polarization. **on right:** Red segment indicates VA range where optical response is calculated.

Uncoated retroreflectors FFDPs are influenced by the polarization of the laser beam. Lunar laser ranging stations use linear polarized beams, but they cannot control its direction. We then spanned the direction of the linear polarization from horizontal (90) to vertical (0), as by CodeV convention. In the design phase we limited our simulations to the case of linear polarization, but we extended simulations of the performance of the CCR to include also the case of a circular polarization.
The orientation of the retroreflector with respect to the polarization is fundamental, especially for this case of an asymmetric VA distribution. 0 reference orientation is as in Fig. 4.3, with a physical edge vertical. We varied the orientation in the range $[-120°; 120°]$ with 30° step.
The following plots show the results of such simulations done for a single DAO case and a double DAO case. In the single DAO case the offset was assigned to the vertical edge in Fig. 4.3. In the two DAO case the offsets were assigned to the two bottom edges of Fig. 4.3.

As affirmed earlier we do not know in advance what could be the polarization of the laser beam hitting the retroreflector, so we concentrated, to determine the optimum solution, on a point on the previous plots which did not have a big variation in intensity with respect its average value. Looking at plots in Fig. 4.4, 4.5, 4.6 and

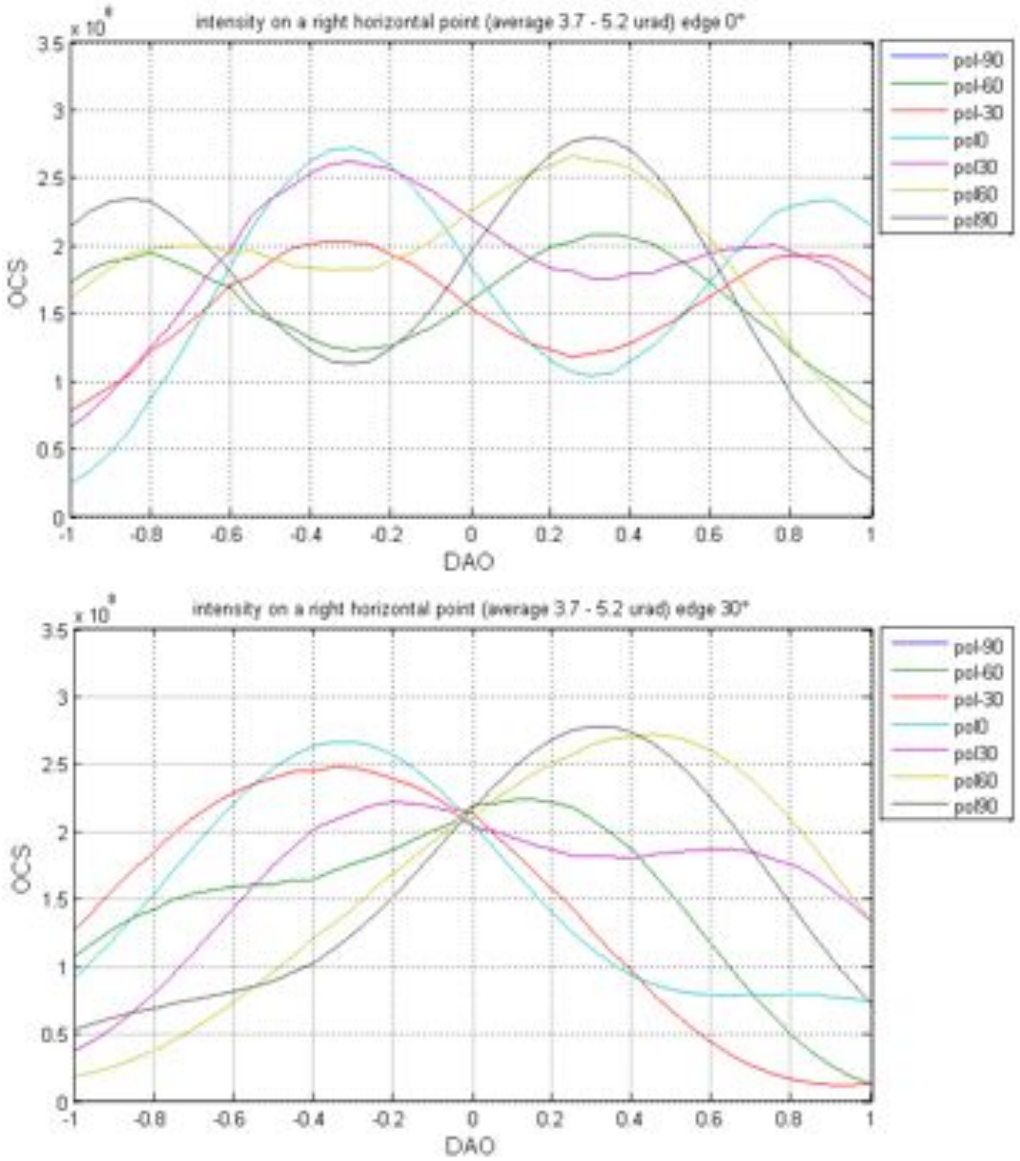

Figure 4.4: Single DAO simulations. CCR orientation 0° and 30° (negative cases are just symmetric).

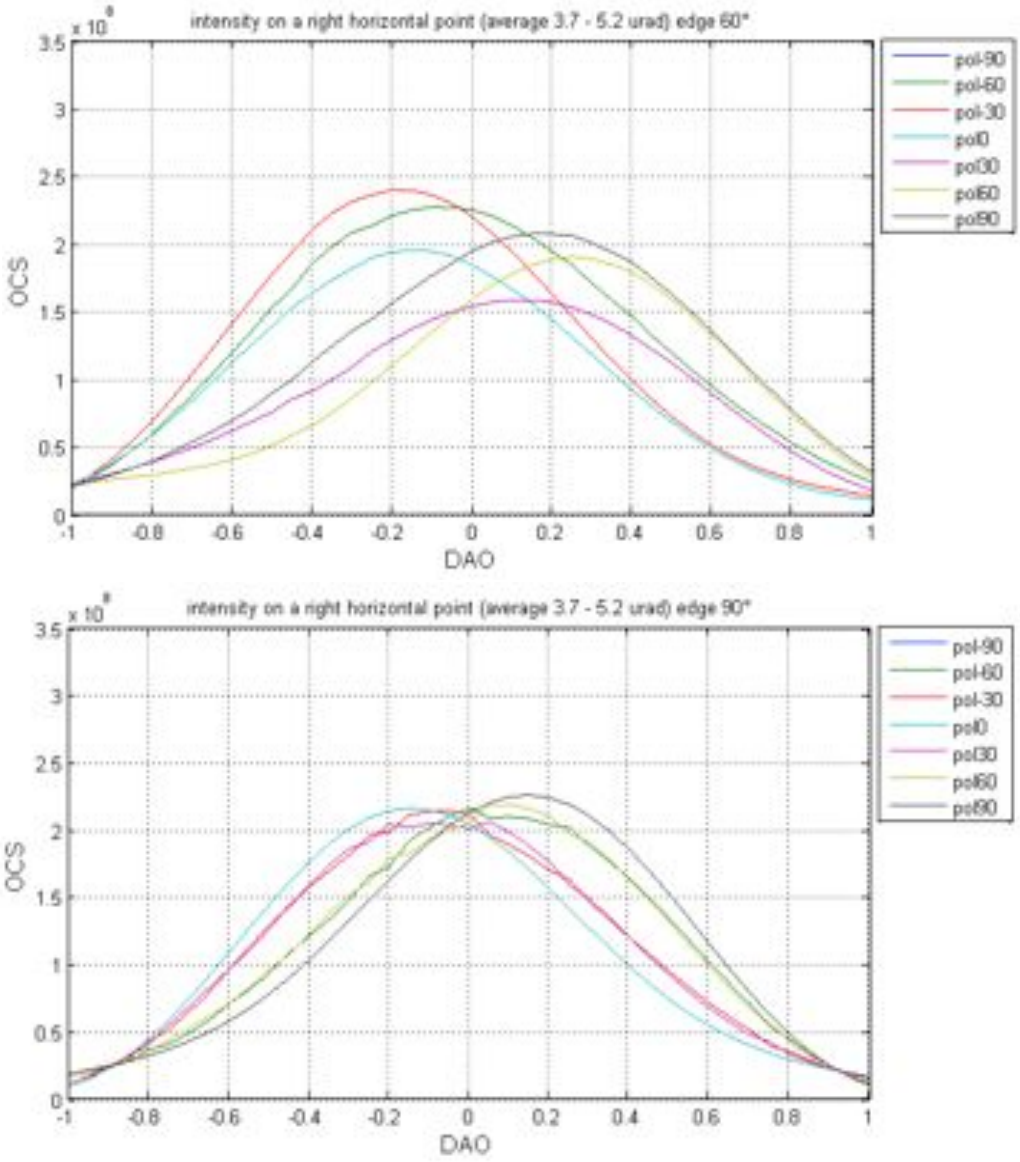

Figure 4.5: Single DAO simulations. CCR orientation 60° to 90° (negative cases are just symmetric).

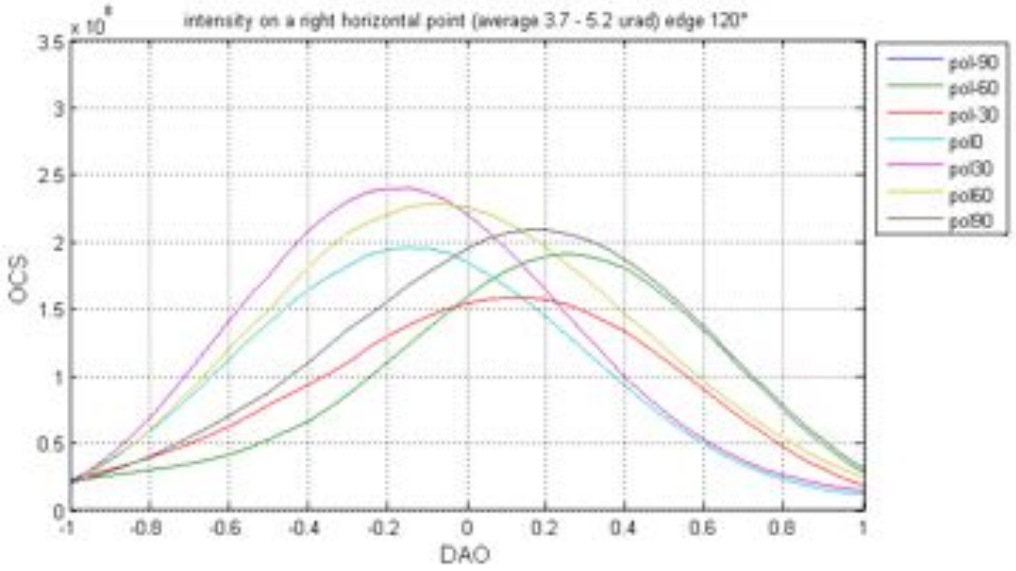

Figure 4.6: Single DAO simulations. CCR orientation 120° (negative cases are just symmetric).

4.7, 4.8, 4.9 we determined two optimum configurations:

- DAO (0,0,0) arcsec, orientation 90°
- DAO (0.6,0,0) arcsec, orientation 0°

4.3 Structural design

The actual MoonLIGHT-2 design depends on two key elements that will be described in more detail in the following subsections:

- Sunshade: Originally, the first MoonLIGHT-2 design was provided with a sunshade, but the GR simulations carried out in collaboration with the CfA, show that its impact on the scientific performance is not so determinant, so the Sun Shade was removed in order to obtain a weight decrease. The subsection 4.3.1 will describe the general relativity simulation and its results.

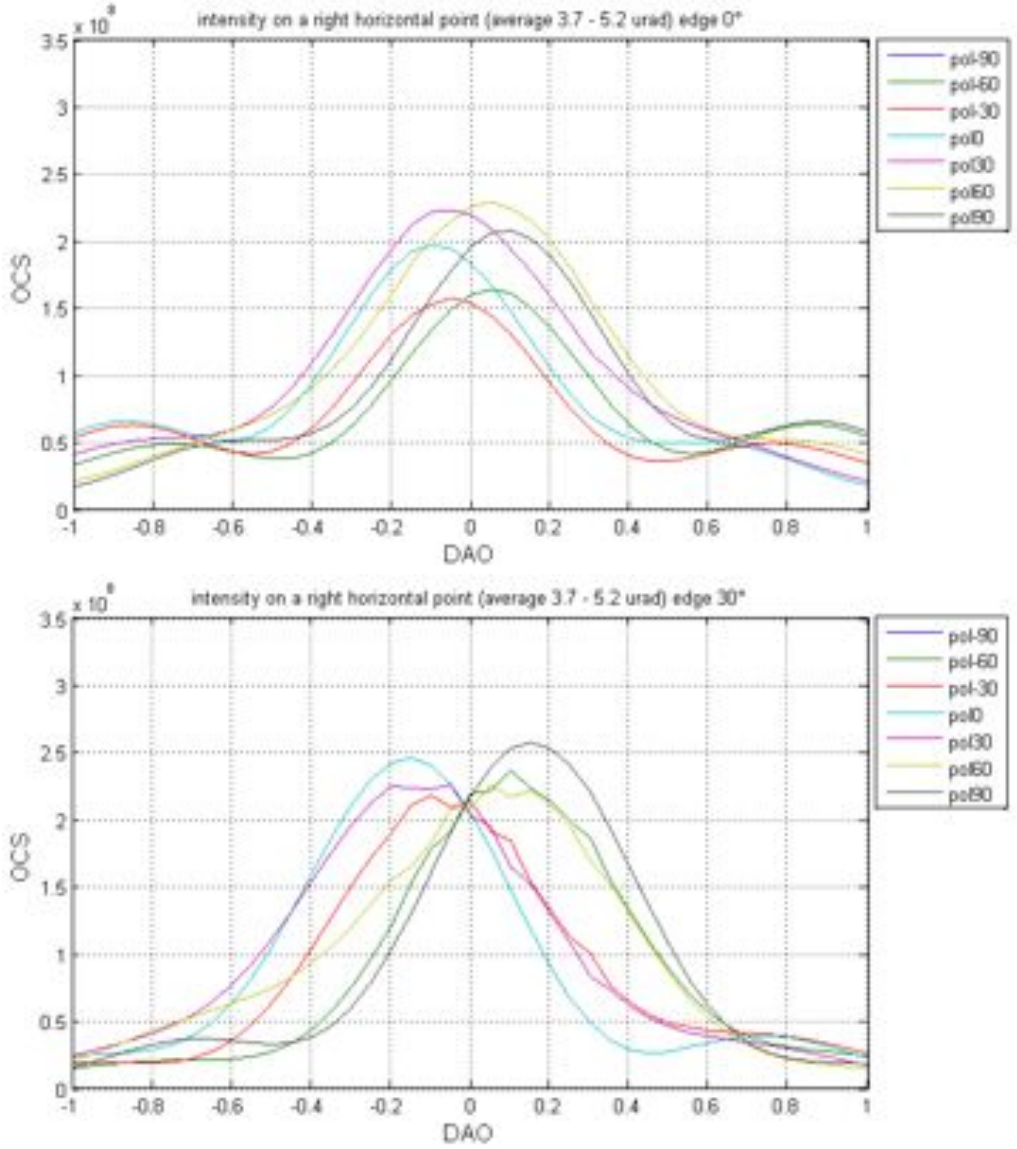

Figure 4.7: Double DAO simulations. CCR orientation 0° and 30° (negative cases are just symmetric).

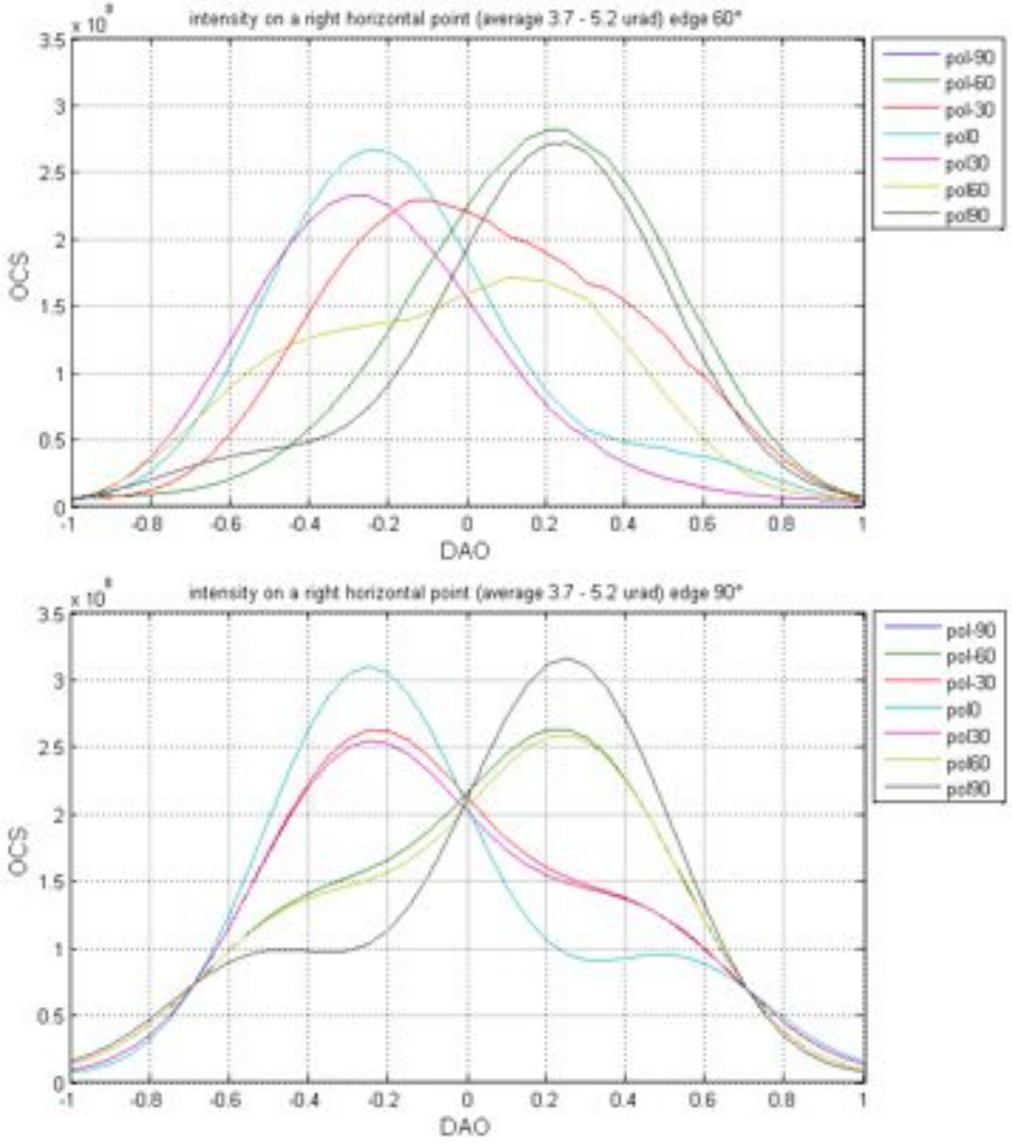

Figure 4.8: Double DAO simulations. CCR orientation 60° to 90° (negative cases are just symmetric).

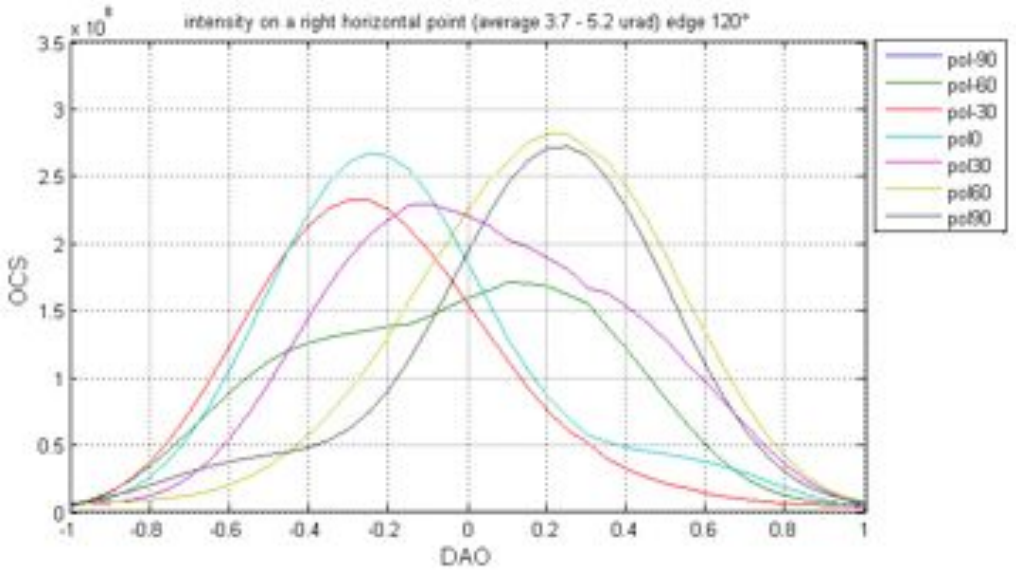

Figure 4.9: Double DAO simulations. CCR orientation 120° (negative cases are just symmetric).

- Structure: The MoonLIGHT-2 housing structure, instead must follow two general requirements: reduce any thermal gradient between CCR and structure, and be enough sturdy to endure the shock vibration during the launch. The subsection 4.3.2 will describe the Falcon-9 vector and the structural requirements for the launch with this vector.

The subsection 4.3.3 will describe the actual MoonLIGHT-2 housing structure coming from the two above points.

4.3.1 Sunshade vs sunshade-less

In the former MoonLIGHT-2 designs, the payload was provided with a Sunshade. The Sunshade (visible in yellow in figure 4.10, left side) was cylindrical-like structure designed to shield the CCR front face from the direct solar radiation. In this way the payload was available even during daylight for LLR, increasing the data collected (and its statistics) and so the accuracy in GR tests.

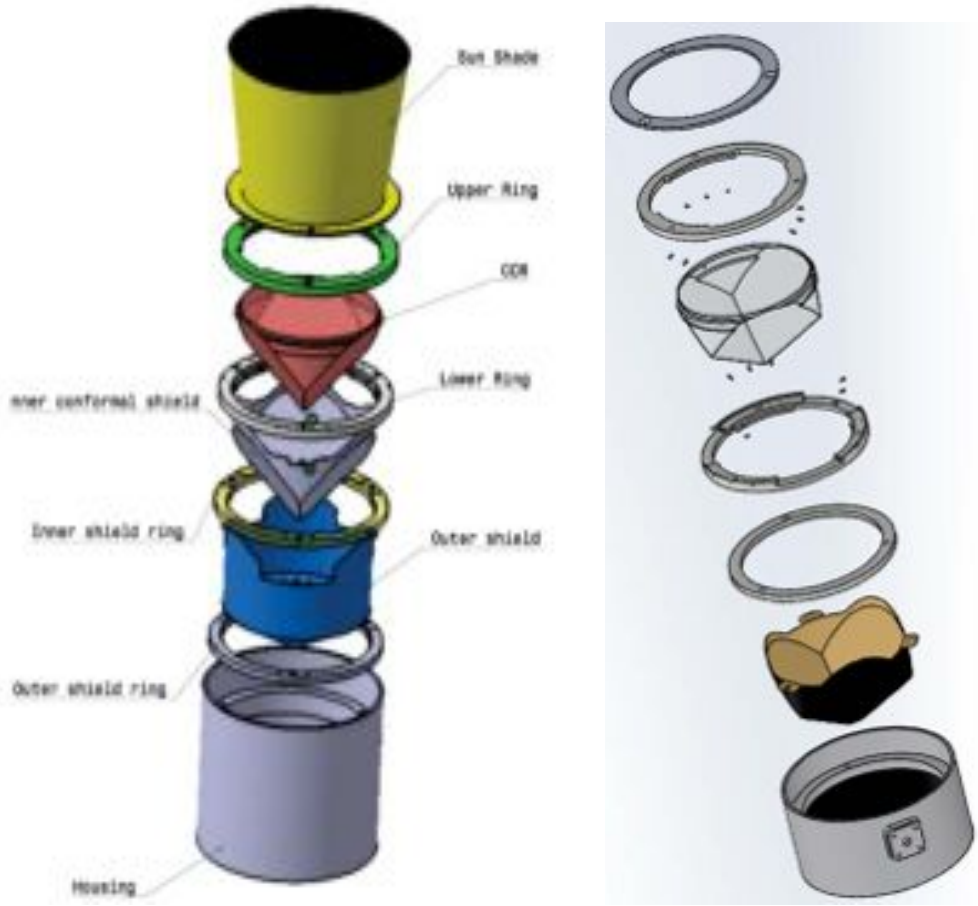

Figure 4.10: on the left: former MoonLIGHT-2 design with a sunshade. **on the right:** actual MoonLIGHT-2 design without the sunshade

However a series of GR simulations with PEP, in collaboration with the CfA of Boston, was carried out. The simulation want to see the effective improvement in test accuracy with data collected also during the daylight with respect to data collected only at night (from the laser ground station), in other words the simulation wants to compare the GR test expected accuracy using a design with or without the Sunshade. In the following part of the section the simulation with its results will be described, however please refer to chapter 6 for the details about the GR tests and the simulations with PEP. We used simulated data from the three Apollo and three MoonLIGHT-2 CCR for four different ground stations: APOLLO, CERGA, McDon-

ald Laser Ranging Station (MLRS) and MLRO. For the MoonLIGHT-2 moon sites, we chose the real deployment sites from the mission MoonExpress (65°N 40°W), Astrobotic (50°S 35°E) and Israel (45°N 27.2°E)(originally, before the choosing of Moon Express, MoonLIGHT-2 was proposed also for Astrobotic and Israel).In this analysis we simulated data starting from 2013 until 2030 (with a time span of 2-3 years) and use the two types of MoonLIGHT-2 design, with and without sunshade. In the first case (design with a sunshade), the MoonLIGHT-2 reflectors were shielded and therefore available whenever conditions were suitable at the observation site. In the second case (design without sunshade), the MoonLIGHT-2 reflectors were unavailable when illuminated, reducing the amount of collectable data. All the reflectors are deemed to be available when the Moon's elevation is 30° or more, as long as the Sun is at least 10° below the horizon. For this simulation, we computed the values of h (variation of the geodetic precession from general relativity value), β and $\frac{\dot{G}}{G}$. The results of the simulation are presented in the following bullets, that report the GR test accuracy for the cases with and without Sunshade and the differences between the two cases:

- h = there is an improvement of 84.4% with the Sunshade, and 81.5% without it. The relative variation between the two cases is: 2.9%.
- β = there is an improvement of 83.8% with the Sunshade, and 81.2% without it. The relative variation between the two cases is: 2.7%.
- η = there is an improvement of 84.4% with the Sunshade, and 81.5% without it. The relative variation between the two cases is: 2.9%.
- $\frac{\dot{G}}{G}$ = there is an improvement of 93.8% with the Sunshade, and 93.1% without it. The relative variation between the two cases is: 0.6%.

The GR tests with the sunshade show a slightly better accuracy compared to the case without the sunshade as expected. The improvement is due to the longer data acquisition interval available for the design with sunshade. However the data without the Sunshade benefit of a significant improvement respect to the GR starting value

either way. Comparing this results, we think that this improvement for the sunshade design respect to the design without the sunshade (around 3%) does not affect significantly the GR results over such a long time analysis. The minor decrease in the instrument performance in the absence of a sunshade is more than compensated by the optimization of the MoonLIGHT-2 weight for its deployment (around 1kg). So in the following MoonLIGHT-2 designs we removed the Sunshade, as visible in figure 4.10 right side, and in the next simulations (described in chapter 6) we will consider the payload available from the ground stations only during night.

4.3.2 Falcon-9 test

Falcon 9, provided by SpaceX Company, is the launch vehicle will send Moon Express robotic spacecraft to the Moon. It is a two stages launch vehicle, all of them reusable, designed for high reliability. The separation system between first and second stage relies on a pneumatic release and it does not include electro-explosive devices. The launch site is on Cape Canaveral Air Force Station (Florida, USA). In the table below are summarized the main characteristics of the launch vehicle.

Falcon 9 is performed to transfer spacecraft into several inclinations and altitudes, from Low Earth Orbit (LEO), to Geosynchronous Earth Orbit (GEO), to planetary missions. Its fearing has a diameter of 17 ft (5,22 m) and it can accommodate payloads with a mass below 15000 lbs (6800 kg). The maximum allowed mass depends on the orbit and its altitude. During pre-flight and flight operations, payloads are exposed to different environments and they need to be qualified in order to ensure their functionality in safety conditions. During flight, they will be exposed to a range of axial and lateral accelerations. Axial acceleration is defined by the vehicle thrust history and drag, while maximum lateral acceleration primarily depends on engine gimbal maneuvers, wind gusts, first stage engine shutdowns. Figure 4.11 shows Falcon 9 Design Load Factors. Positive axial value indicates compression, while negative value indicates tension of gravity acceleration.

As regards shock loads MoonLIGHT will experienced during flight, there are two main events that are responsible of these:

Characteristics	Stage 1	Stage 2
Structure		
Length	55m for both stages	
Diameter	3.66 m	
Type	LOX tank - monococque: Fuel tank Stringer and ring frame	Monococque
Material	Alluminium lithium	Alluminium lithium
Propulsion		
Engine Type	Liquid, gas generator	Liquid, gas generator
Engyne Manufacturer	SpaceX	SpaceX
Engine Designation	Merlin 1C	Merlin Vacuum
Number of engines	9	1
Propellant	Liquid oxygen/Kerosene (RP-1)	Liquid oxygen/Kerosene (RP-1)
Thrust	1,250,000 lbf (sea level) [5MN]	100,000 lbf (vacuum) [445kN]
Propellant feed system	Turbopump	Turbopump
Throttle capability	No	Yes (60-100%)
Restart capability	No	Yes - 2 restart
Tank pressurization	Heated helium	Heated helium
Thrust Vector Control		
Pitch, yaw	Gimbaled engines	Gimbaled engines
Roll	Gimbaled engines	Turbine exhaust dust
Reaction Control System		
Propellant	Not applicable	Monomethyl hydrazine, nitrogen tetroxide
Thrusters	Not applicable	Draco (4)
Trrust	Not applicable	90 lbf [400N] each
Staging		
Nominal burn time	170 sec	354 sec
Shutdown process	Commanded shutdown	Commanded shutdown
Stage separation system	Pneumatically actuated mechanical collets	Not applicable

Table 4.2: Characteristics of the Falcon-9 launcher

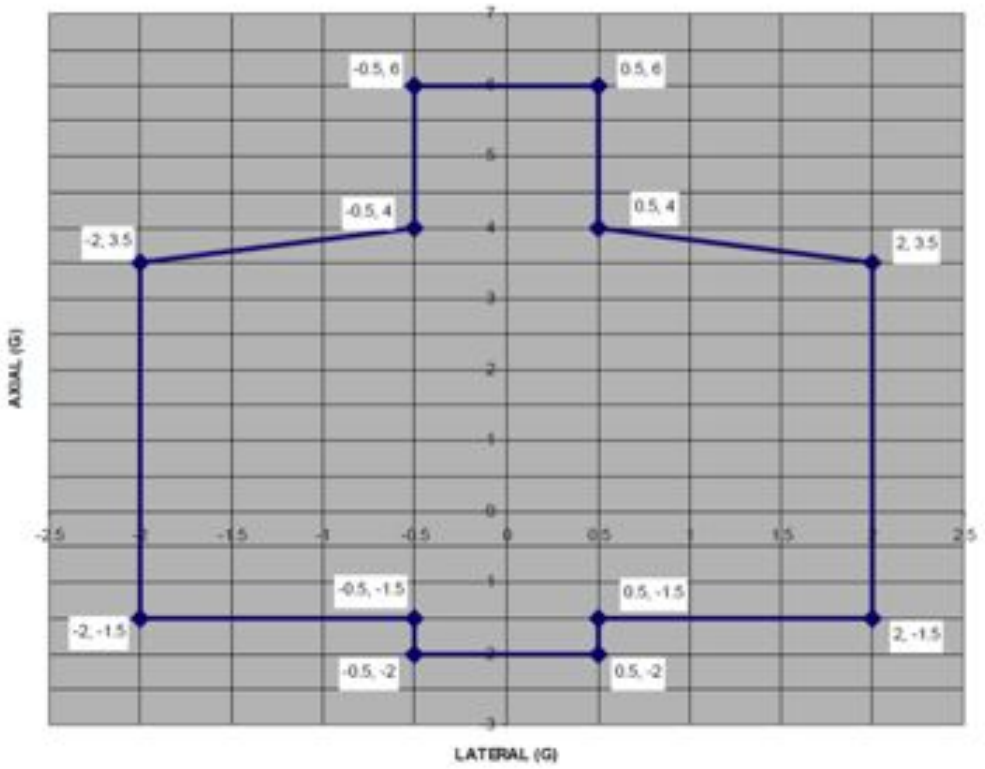

Figure 4.11: Falcon 9 Design Load Factor, provided by Falcon 9 user's guide

- Fairing separation

- Payload release and separation

Figure 4.12 shows the maximum shock environment expected at payload interface.

The maximum temperature seen by MoonLIGHT inside Falcon 9 fairing is shown in Figure 4.13. It depends on the Falcon 9 payload fairing structure, consisting of a 1 inch (2.5 cm) thick aluminum honeycomb core surrounded by carbon fiber face sheet plies and also on its emissivity (0.9).

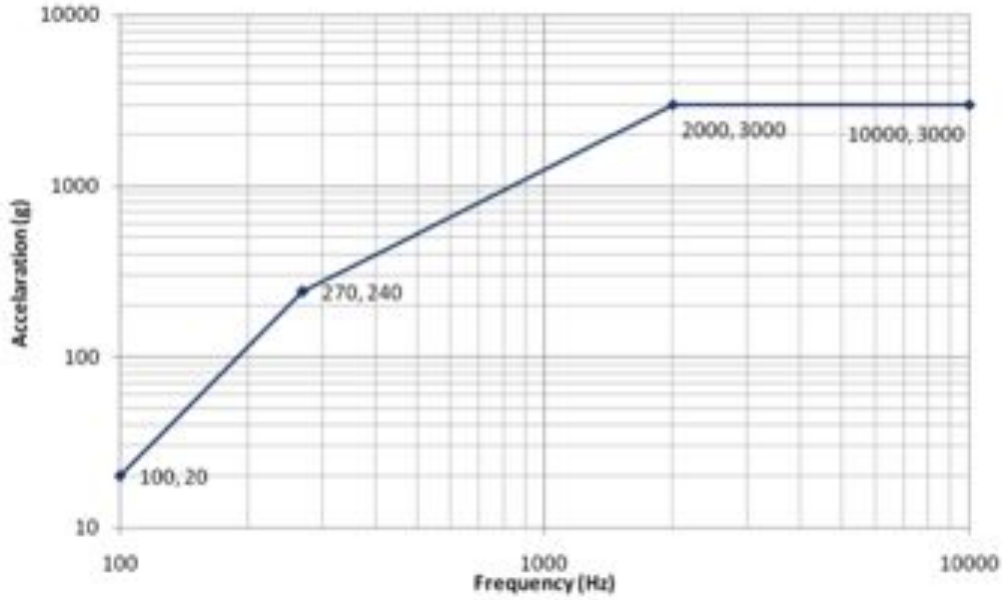

Figure 4.12: Falcon 9 shock response at payload interface, provided by Falcon 9 user's guide

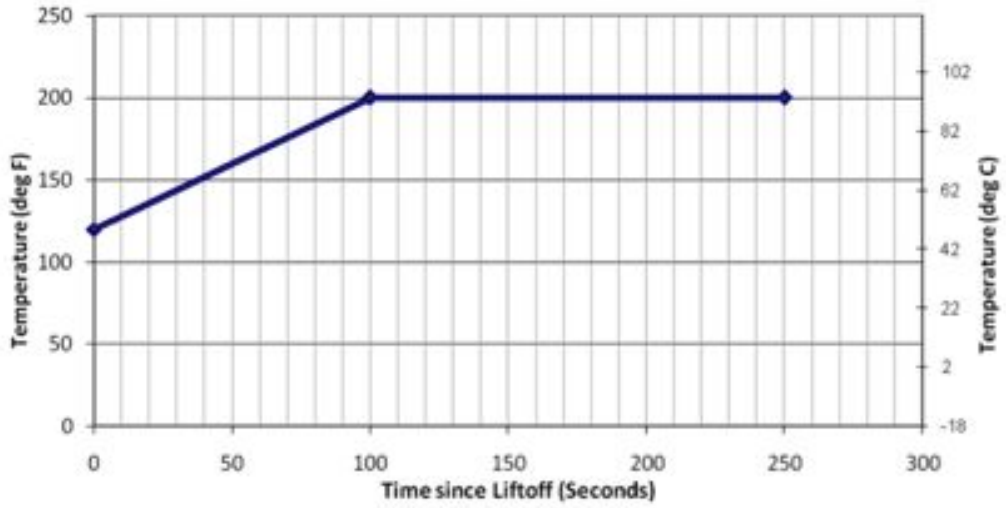

Figure 4.13: Maximum Payload Fairing Temperature Seen By Payload, provided by Falcon 9 user's guide

4.3.3 Actual MoonLIGHT-2 design

At the present time the last optimization of the MoonLIGHT-2 mounting system is shown in figure 4.14.

As we can see from the figure, the actual design is a bit different from the older one. The main differences between these two mounting system can be summarized in:

- In the second model it was not possible to adjust the zenith elevation. With the new one is possible to adjust this angle of about $\pm 30^{\circ}$.
- With the new conformal housing (in the last model) is possible to mount the CCR with its physical edge vertical or horizontal. With the previous model it was possible to put the CCR only with the physical edge horizontal.
- The structural analysis done on the previous model show that the conformal can can encounter resonance problems during the launch. In order to avoid that problem for the last model we will use a conformal housing in order to improve the structural stiffness.

4.4 INRRI

INRRI is a small retroreflector payload designed to be installed on lander and rover designed to mission on rocky solar system body. INRRI is composed by 8 small INRRI (diameter 12.7 mm) glued at the hollow housing, its weight is around 25g and the dimensions are around 7 cm diameter for 3 cm height (see figure 4.15).
The aim is to use INRRI on the ground and an laser source installed on a orbiter around the studied rocky planet/satellite, in this way is possible take laser ranging measurement in order to obtain:

- Altimetry measurements: useful to map obtain detail about the body surface and study possible deformation on the surface produced by tidal effect.

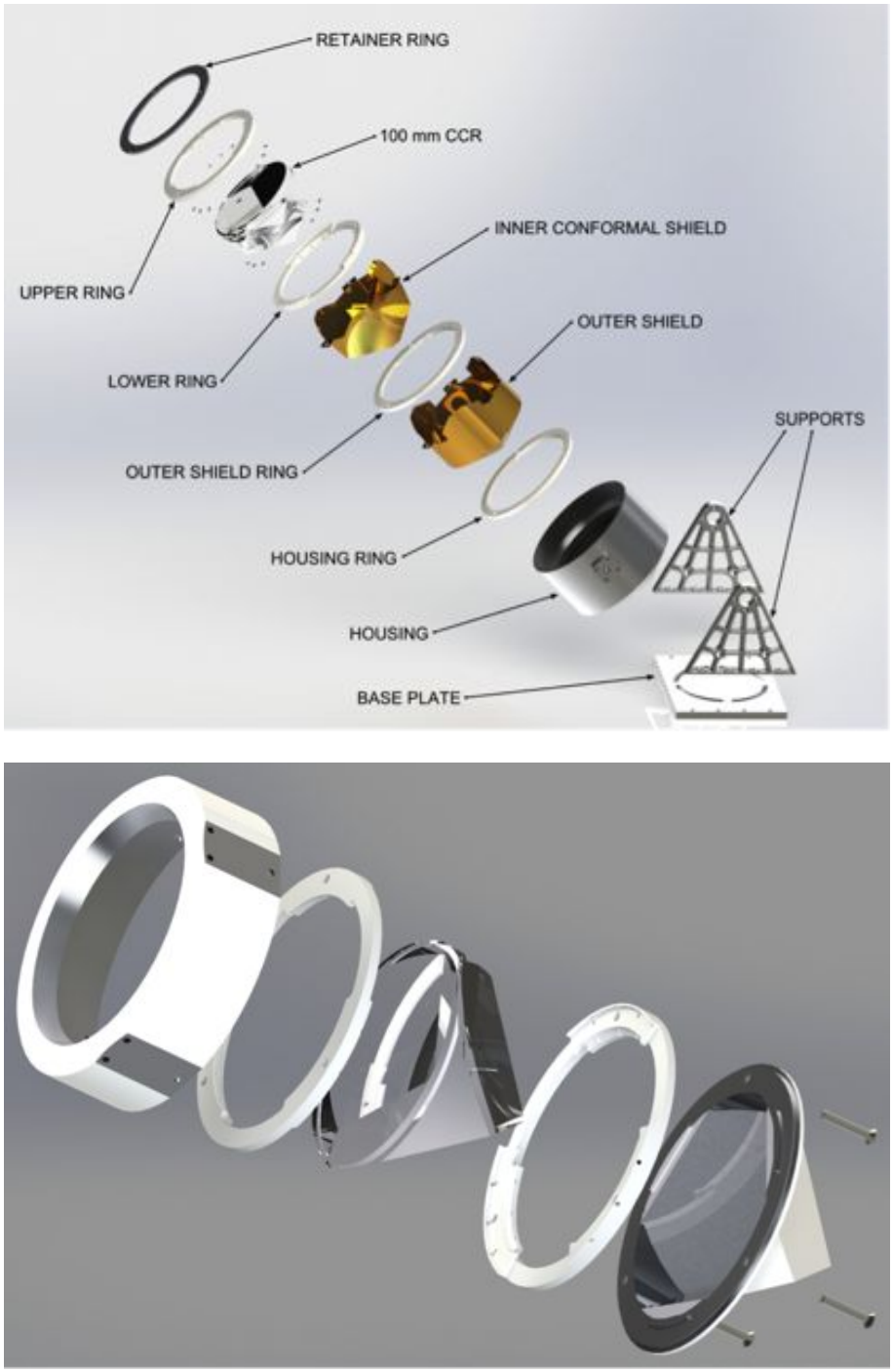

Figure 4.14: **Top:** Full bracket assembly exploded view of the old mounting system. **Bottom:** Exploded view full assembly of the back-mounting conformal housing of the new mounting system

- Center of mass: useful to data that can be used for GR test.

See figure 4.16 for a cartoon showing possible INRRI employment.

Figure 4.15: INRRI setup for the martian precursor test.

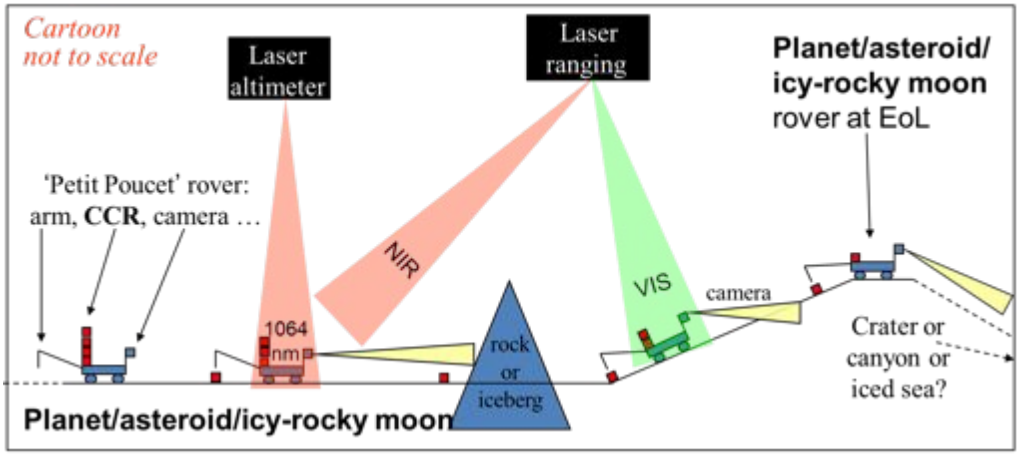

Figure 4.16: INRRI concept cartoon

INRRI is a totally INFN-LNF project, and it is developed and tested at the SCF_Lab. INRRI is currently approved for the Moon Express mission and will be installed on

the Moon along with MoonLIGHT-2 in the 2017. In addition at the SCF_Lab, during the September 2015, a INRRI precursor test for a martian mission is undertaken. At the present details about the test are under confidential agreement.

Chapter 5

The SCF-TEST

The goal of this chapter is to describe the tests carried out at the SCF_Lab in order to characterize MoonLIGHT-2 before the first (out of four) launch, scheduled for 2017, with the Moon Express missions. In the section 5.1 a general description of the SCF-Test will be provided. Then in section 5.1 two test campaigns will be described in specific, showing the MoonLIGHT-2 configuration and the test procedures for the two different campaigns. The sections 5.2 and 5.3 will describe respectively the optical and thermal test procedures and results for each test carried out. Finally the section 5.4 will discuss the tests conclusions, first for each element alone and then comparing the optical simulations along with the optical and thermal tests results.

5.1 The MoonLIGHT-2 SCF-TESTs: general description

The SCF-Test key experimental innovation is the concurrent measurement and modeling of the optical FFDP and the temperature distribution of the SLR/LLR retroreflector payload under thermal conditions produced with a close-match solar simulator. The tests apparatus (described in chapter 3) includes infrared cameras for non-invasive thermometry, PT100 probes for invasive thermometry, thermal control

electronics and systems for real-time movement of the payload to experimentally simulate payload orientation with respect to both solar illumination and laser interrogation beams. For the detail of MoonLIGHT-2 orientation respect to the three window in the SCF-G and the convention used to define the angle value respect to payload orientation see figure 5.1.

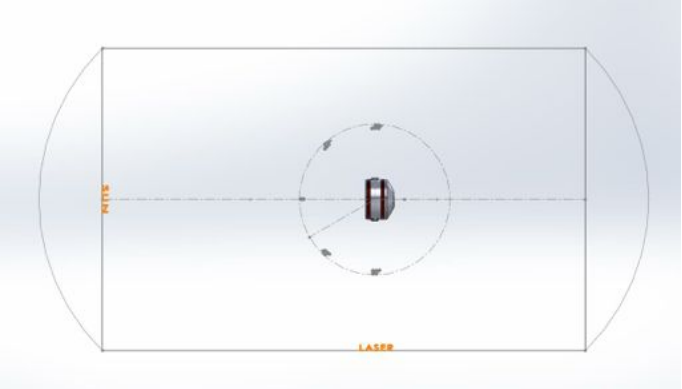

Figure 5.1: CAD sketching from an above viewpoint the position of MoonLIGHT inside the cryostat, with respect to the solar window (left) and the laser window (down).

These unique capabilities provide experimental validation of the space segment for SLR and LLR. For MoonLIGHT-2 with the SCF-Test we want to evaluate:

1. CCR FFDPs under simulated space conditions, with the same optical circuit described in section 3.6; the laser beam has a default linear polarization and an adjustable incidence angle with respect to the normal to the CCR face (see section 5.2 for the acquisition and analysis procedure used);
2. CCR surface temperature and its thermal constant τ_{CCR} using the infrared camera described in section 3.5 (see section 5.3 for the acquisition and analysis procedure used);
3. temperature on the other MoonLIGHT-2 structural component with PT100 contact probes. See following part of the section for the probes configuration used.

First and foremost in the MoonLIGHT-2 test first and foremost we mount the payload assembly inside the SCF-G, thermally decoupled from the shroud (see figures 5.2). Before the start of the test first we must take the SCF-G in cryogenic and vacuum condition: internal chamber pressure about $\times 10^{-6} mbar$ and an T_{shroud} about 90K. Then we hold the average temperature of the MoonLIGHT-2 mechanical support structure (using two resistive wires heater types on the housing), $T_{housing}$, to the expected test average value, waiting plateau condition for MoonLIGHT-2 and SCF-G. In this phase MoonLIGHT-2 faces the optical window for at least 12h. After the reach of the steady condition (plateau condition for 30-60 minutes) the test can start, this phase can be schematized in the following tree experimental steps:

- **Steady state conditioning**: we take 1 FFDP and 1 IR simultaneously in order to acquire the payload initial conditions before the test starts.

- **SUN ON heating phase**: MoonLIGHT-2 faces the solar window with a fixed angle (0° and 30°). Here we take only IR pictures with a fixed cadence. This phase lasts for a defined time (t_{ON}), see section 5.3 for the details.

- **SUN OFF cooling phase**: the solar illumination is closed and the payload feces the optical window. Here we take IR pictures with a fixed cadence and simultaneously FFDP with a different fixed cadence. This phase lasts for a defined time (t_{OFF}), see sections 5.2 and 5.3 for the details.

The test will be repeated for different $T_{housing}$ and different inclinations between CCR and solar radiation during the SUN ON phase, in this way we want to see how much the thermal and optical behavior changes in different experimental conditions. The above description is a general presentation of the SCF-Test, but we conduct two different test campaigns, with different probes configurations and MoonLIGHT-2 structures. For this reason in the two following sections the detail of two tests configurations will be described. We refer to subsection 5.1 to details about these two different test campaigns.

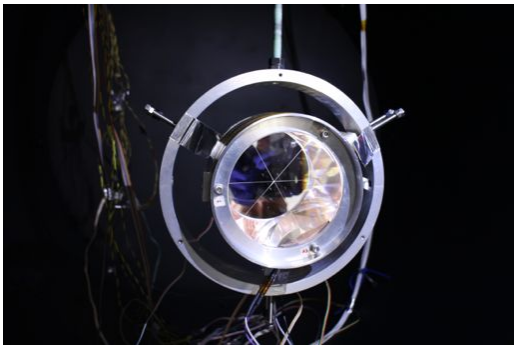

(a) *Front view.*

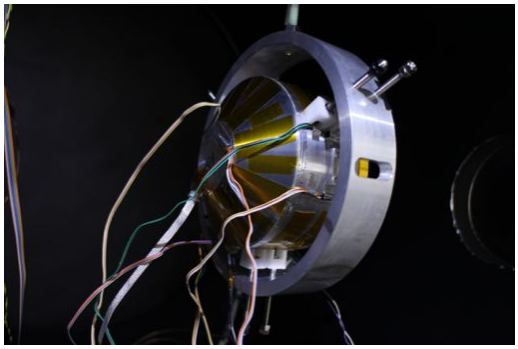

(b) *Rear view.*

(c) *Upper view.*

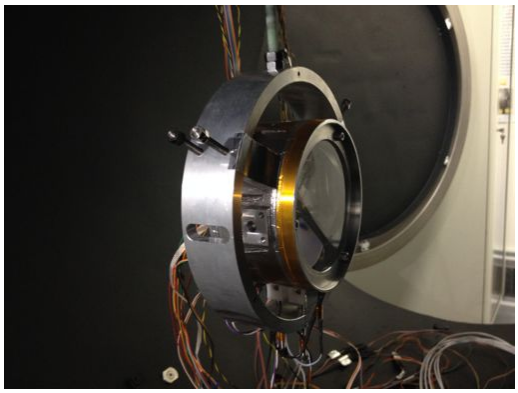

(d) *Side view.*

Figure 5.2: MoonLIGHT-2 inside the SCF-G chamber ready for the tests

1^{st} SCF-Test descriptions details

The assembly used for this tests campaign is visible in figure 5.3; from left to right, is composed of:

1. Aluminum ring with 3 screws, tightened at 0.5 Nm
2. Upper ring (Delrin).
3. MoonLIGHT-2 big CCR.
4. Lower ring (Delrin).
5. Can Ring (Delrin, with 3 probes near screw holes).
6. Conformal Can (in thermal contact with the housing, using 3 thermal pads, pressed between the can tabs and the housing).
7. External Housing with the two resistive heating tapes (two wires) for thermal control installed. The housing is covered with a set of Kapton tapes in order to increase the thermal exchange with the environment (SCF-G shroud).

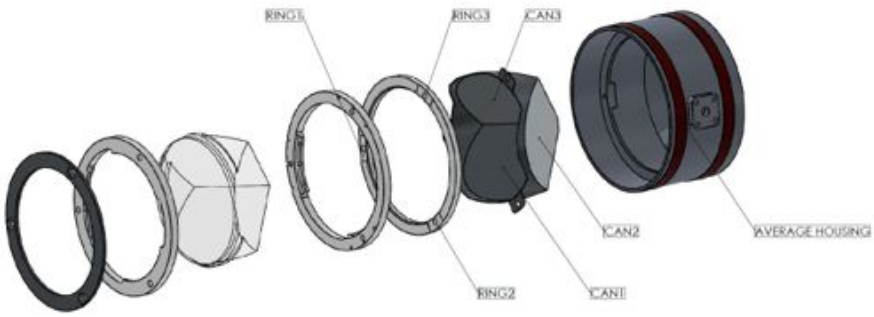

Figure 5.3: MoonLIGHT-2 assembly for first test campaign with probes position

For this test campaign a total of eleven PT100 probes was installed in the following configuration (see figures 5.3 and 5.4 for the scheme positioning):

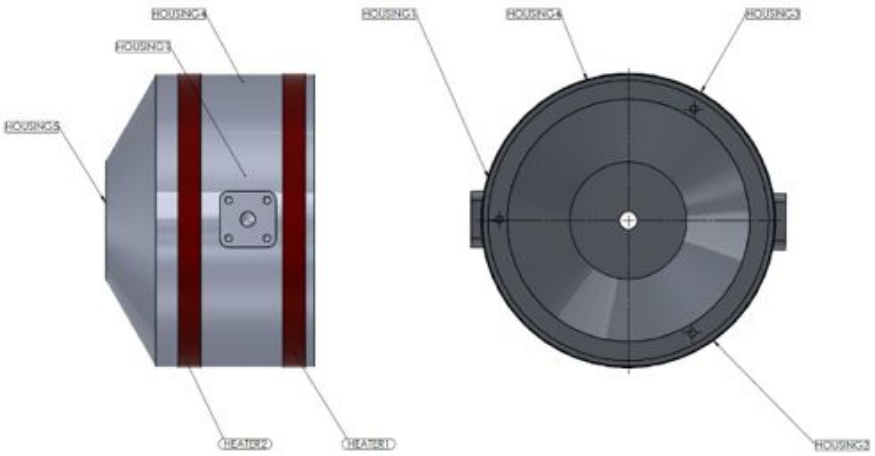

Figure 5.4: MoonLIGHT-2 Housing probes positioning

- 3 probes on the lower ring (see figure 5.5a and 5.5b).
- 3 probes on the Conformal Can (see figure 5.5c).
- 5 probes (see figure 5.5d) (in thermal plots only the average temperature among them has been shown).

With this configuration we performed 2 different SCF-TESTs, both with t_{ON}=t_{OFF}=12h:

1. Housing temperature at 300K, sun incidence on front face CCR during SUN ON equal to 0°
2. Housing temperature at 300K, sun incidence on front face CCR during SUN ON equal to 30° (breakthrough condition)

2^{nd} SCF-Test descriptions details

With respect to the first test campaign, we added copper tape on the three triangular areas below the tabs and on the cylindrical surface of the tabs (figure 5.7) in order to reduce the thermal conductivity between the CCR and its assembly. The remaining

(a) *Installing of 3 probes on the lower ring.*

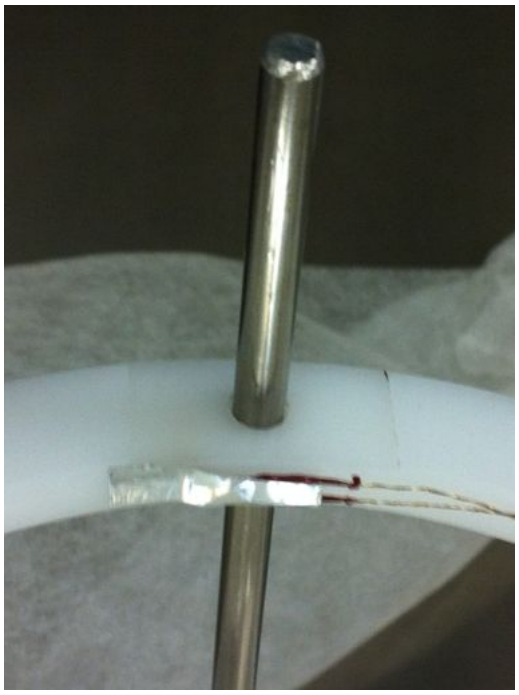

(b) *Installing of 3 probes on the lower ring (side view).*

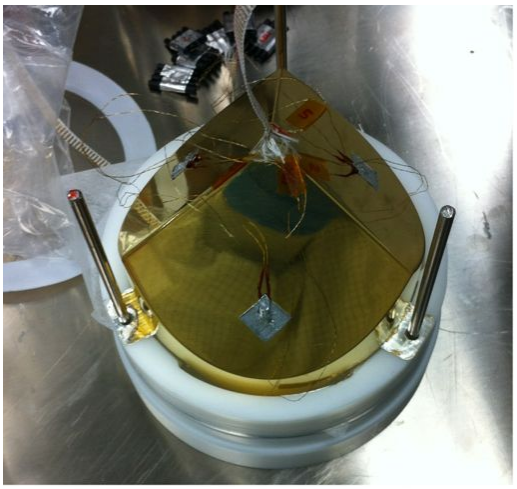

(c) *Installing of 3 probes on the conformal Can.*

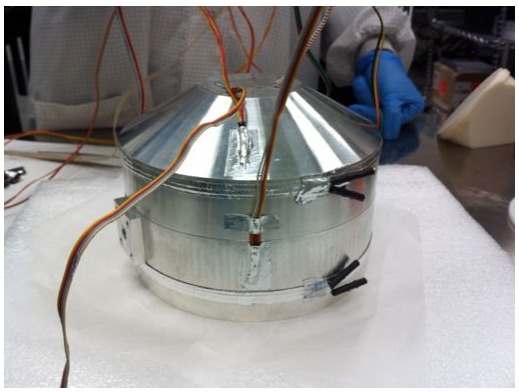

(d) *Installing of 5 probes on the housing.*

Figure 5.5: MoonLIGHT-2 PT100 probes positioning for first test campaign

assembly structure is the same but we modified the probes positioning using the scheme in figure 5.6 (refer always to figure 5.4 for housing probe positioning that do not change). In this second configuration we have always eleven probes now so distributed this way:

- 1 probe on the lower kel-f ring (figure 5.8b)
- 5 probe on the conformal Can (figure 5.8a)
- 5 probes on the housing (just as in first test campaign, figure 5.5d)

With this configuration we performed 3 different SCF-TESTs, all with t_{ON}=13h and t_{OFF}=14h (now we have increased the test time in order to reach a better steady condition after the SUN ON/OFF):

1. Housing temperature at 250K, sun incidence on front face CCR during SUN ON equal to 0°
2. Housing temperature at 300K, sun incidence on front face CCR during SUN ON equal to 0°
3. Housing temperature at 330K, sun incidence on front face CCR during SUN ON equal to 0°

5.2 Optical results

MoonLIGHT was mounted to the SCF-G move and handling system, inside the cryostat, in order to be stimulated by the simulated space environment (vacuum, cold, Sun). Environmental stimulation would affect MoonLIGHT optical behavior. MoonLIGHT underwent two SCF-Tests, with two different fixed temperatures of the housing: 250 K and 300 K. Both SCF-Tests were performed at 0°, i.e. with the CCR front face perpendicular to the Sun Simulator and directly hit by solar flux (fig.5.1 shows exactly such a configuration). Briefly, every SCF-Test consists of a

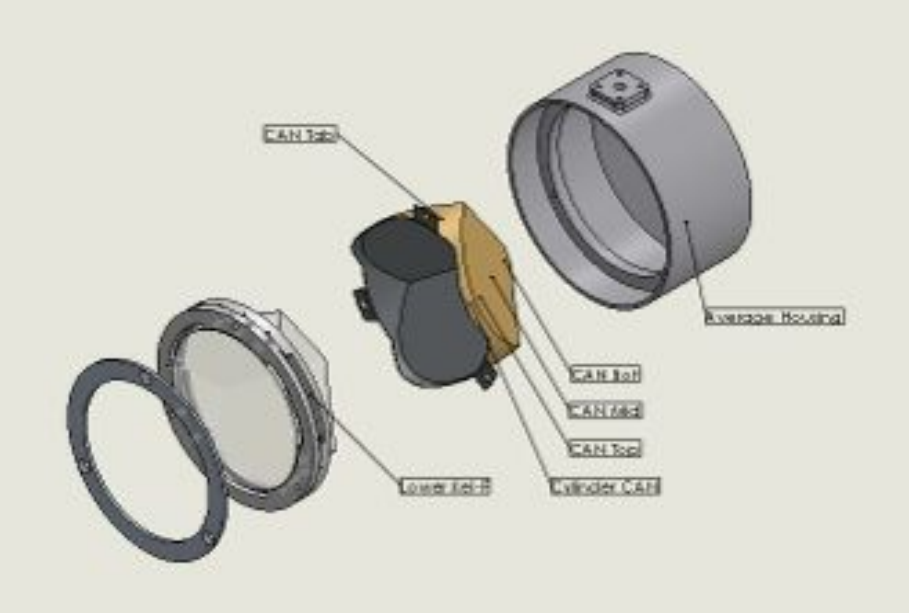

Figure 5.6: MoonLIGHT-2 assembly for second test campaign with probes position

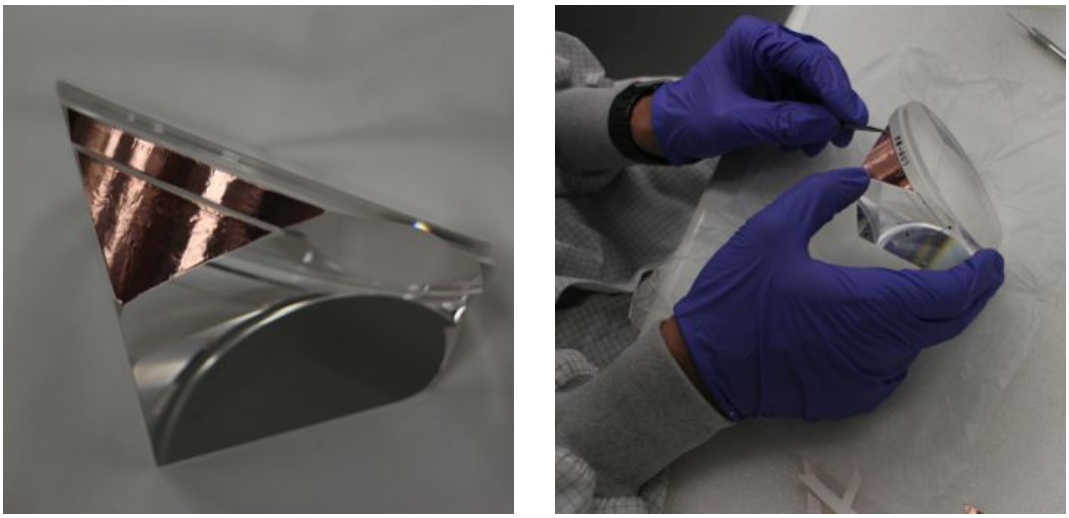

Figure 5.7: MoonLIGHT-2 copper tape placement for second test campaign

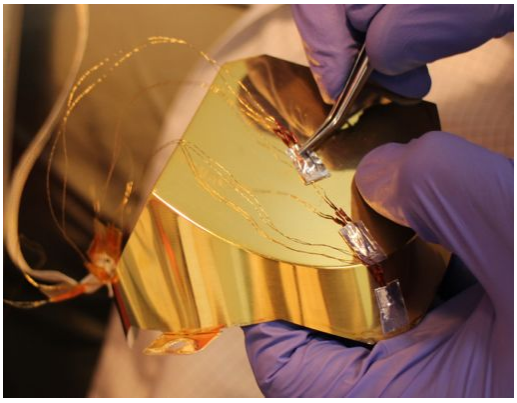

(a) *Installing of 5 probes on the conformal can.*

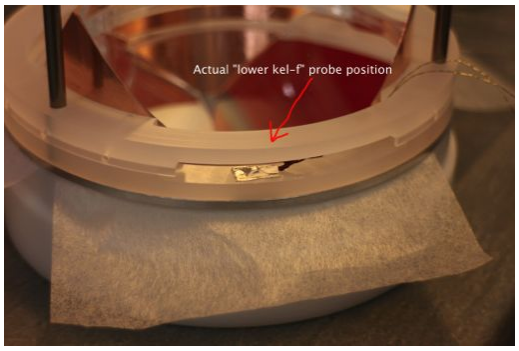

(b) *Installing of 1 probe on the kel-f ring.*

Figure 5.8: MoonLIGHT-2 PT100 probes positioning for second test campaign

heating (Sun ON) phase of 13h and a cooling (Sun OFF) phase of 14 h. During both phases, temperature probe constantly monitor the temperatures of all the assembly; whereas, during cooling phase only, the CCR is optically interrogated in order to link its behavior to the steady-state optical condition (just before Sun ON start) taken as a baseline.

5.2.1 1^{st} SCF Test campaign

Before starting Sun ON phase, with vacuum pulling and LN2 flowing in cryostat systems, first FFDP, named 000, is acquired; it will serve as a baseline steady-state optical condition (Figure 5.9).

Then, for the rest of the Sun ON phase, no optical interrogation is performed, in order not to affect the thermal stimulation of the assembly. During Sun OFF phase, FFDPs are shot with the following frequencies:

- 1 FFDP every 2 minutes for 60 minutes.
- 1 FFDP every 4 minutes for 60 minutes.
- 1 FFDP every 10 minutes for 120 minutes.

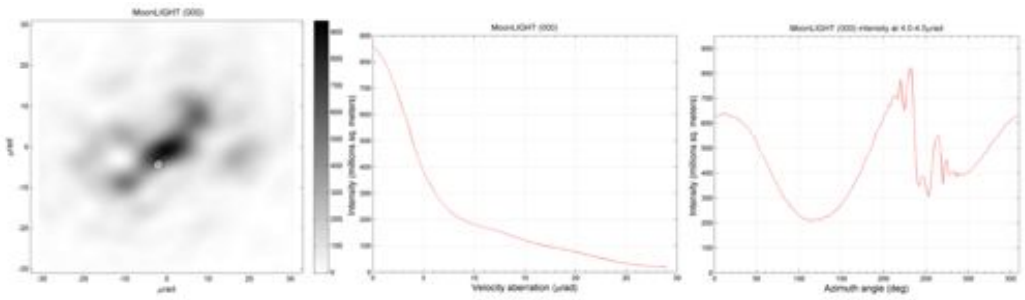

Figure 5.9: Starting from right: 1) FFDP, 2) intensity vs velocity aberration, 3) intensity vs azimuth angle at range 4.0-4.5 μrad, all taken before Sun ON phase.

- 1 FFDP every 30 minutes until the end of the phase.

Figures 5.10 and 5.11 show respectively FFDP 001, at the beginning of the Sun OFF phase and FFDP 074, that is the last one.

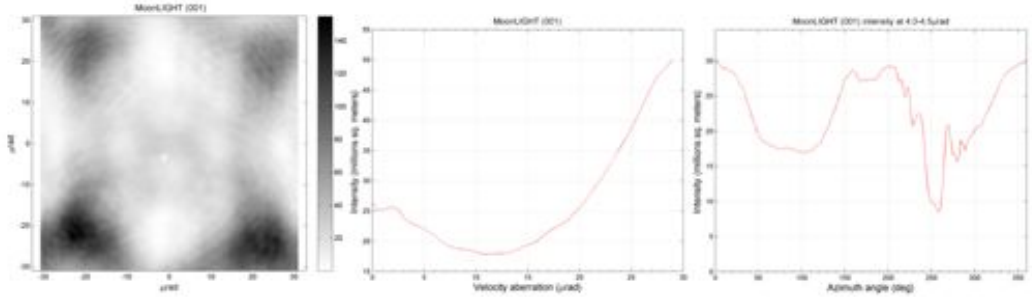

Figure 5.10: Starting from right: 1) FFDP, 2) intensity vs velocity aberration, 3) intensity vs azimuth angle at range 4.0-4.5 μrad, all taken at beginning of Sun OFF phase.

The figures show three different plots each:

- Total FFDP.
- Average intensity in millions square meters vs velocity aberration in μrads.

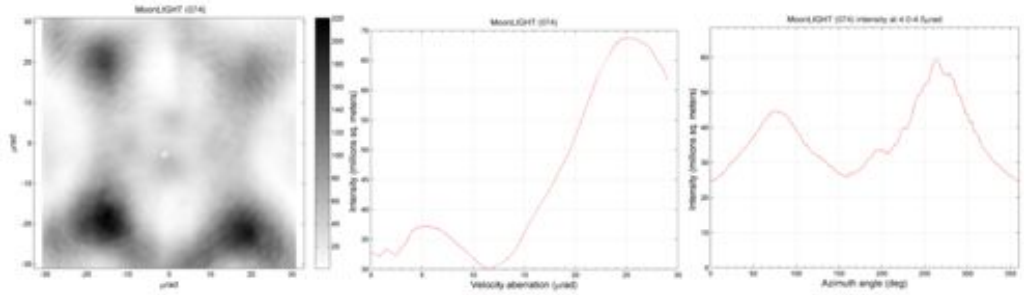

Figure 5.11: Starting from right: 1) FFDP, 2) intensity vs velocity aberration, 3) intensity vs azimuth angle at range 4.0-4.5 μrad, all taken at the end of Sun OFF phase.

- Intensity in millions square meters in the range (4.0-4.5) μ rad vs azimuth angle in degrees.

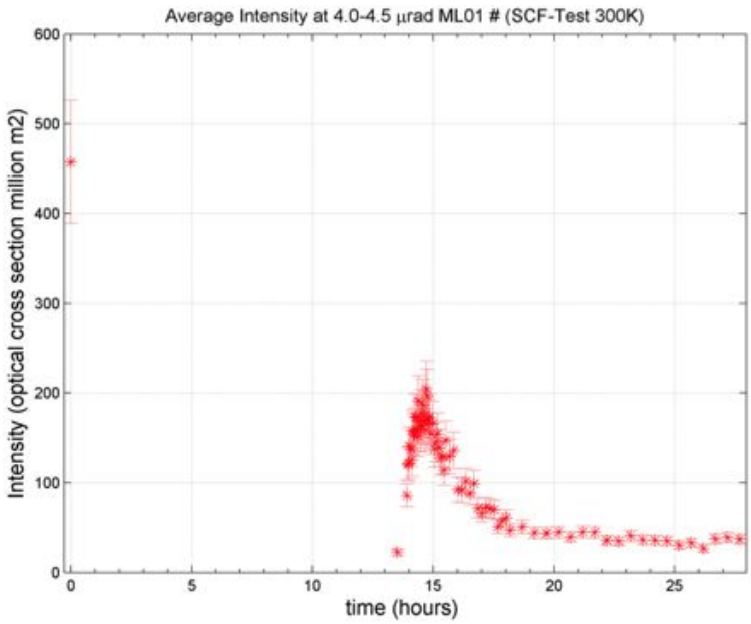

Figure 5.12: Average intensity vs time at range 4.0-4.5 μrad during the SCF-Test with housing at 300 K.

In figure 5.12 the average intensity vs time at range (4.0-4.5) μrad, during the whole test, is shown.

5.2.2 2^{nd} SCF Test campaign

Before starting Sun ON phase, with vacuum pulling and LN2 flowing in cryostat systems, first FFDP, named 000, is acquired; it will serve as a baseline steady-state optical condition (Figure 5.13).

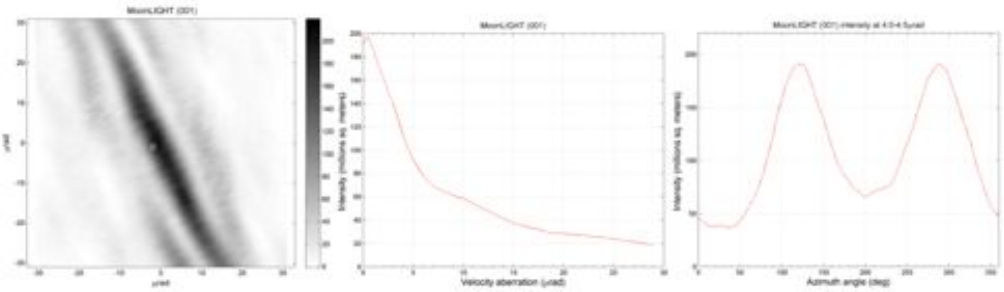

Figure 5.13: Starting from right: 1) FFDP, 2) intensity vs velocity aberration, 3) intensity vs azimuth angle at range 4.0-4.5 μrad, all taken before Sun ON phase.

Then, for the rest of the Sun ON phase, no optical interrogation is performed, in order not to affect the thermal stimulation of the assembly. During Sun OFF phase, FFDPs are shot with the following frequencies:

- 1 FFDP every 2 minutes for 60 minutes.
- 1 FFDP every 4 minutes for 60 minutes.
- 1 FFDP every 10 minutes for 120 minutes.
- 1 FFDP every 30 minutes until the end of the phase.

Figures 5.14 and 5.15 show respectively FFDP 002, at the beginning of the Sun OFF phase and FFDP 079, that is the last one.

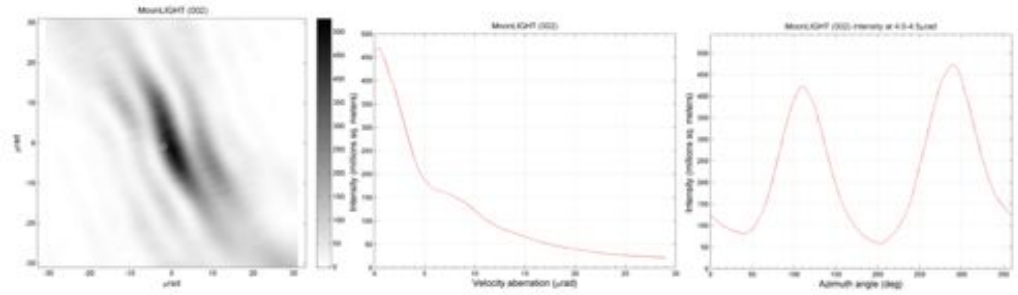

Figure 5.14: Starting from right: 1) FFDP, 2) intensity vs velocity aberration, 3) intensity vs azimuth angle at range 4.0-4.5 μrad, all taken at beginning of Sun OFF phase.

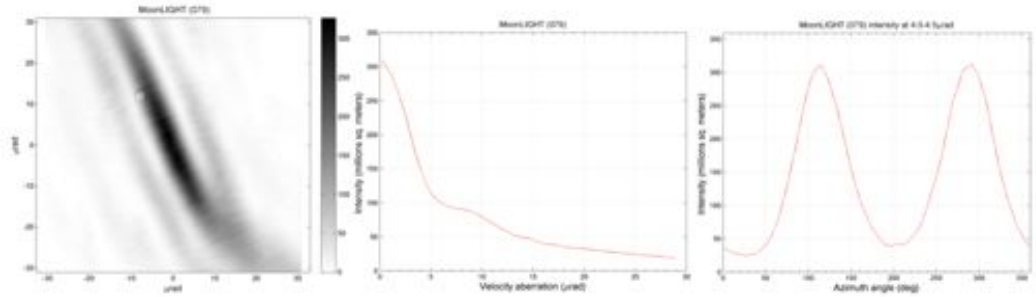

Figure 5.15: Starting from right: 1) FFDP, 2) intensity vs velocity aberration, 3) intensity vs azimuth angle at range 4.0-4.5 μrad, all taken at the end of Sun OFF phase.

The figures show three different plots each:

- Total FFDP.
- Average intensity in millions square meters vs velocity aberration in μrads.
- Intensity in millions square meters in the range (4.0-4.5) μrad vs azimuth angle in degrees.

In figure 5.16 the average intensity vs time at range (4.0-4.5) μrad, during the whole test, is shown.

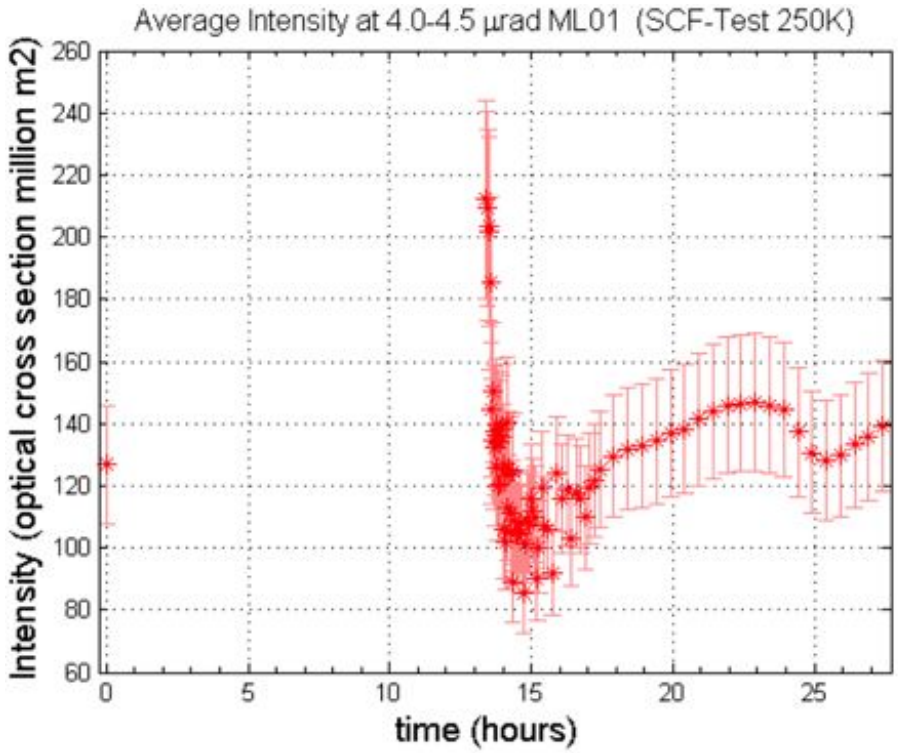

Figure 5.16: Average intensity vs time at range 4.0-4.5 μrad during the SCF-Test with housing at 250 K.

5.3 Thermal results

In this section the procedures used to analyze the IR thermal data will be described. During the first SCF-Test campaign, for each phase, we recorded 1 IR every 5 minutes for the first 30 minutes and 1IR every 5 minutes for the remaining minutes; while for the second SCF-Test campaign, for each phase, we recorded 1 IR every 2 minutes for all the phase lasting in order to acquire more data available for the analysis. The IR analysis is achieved with FLIR Thermacam Researcher software and a specific Matlab code. With FLIR Thermacam Researcher SW we select all the visible CCR front face area, as shown in the Figure 5.17a, in order to extract the average temperature within this area w.r.t. test time. Then we use a custom Matlab code, developed by the SCF_Lab team, to analyze these raw data. The

program computes the best fit parameters searching the minimum of the chi square function on degrees of freedom, where:

- the experimental data are the observed values.
- the pure exponential function describe in equation 5.1 is the expected function.

$$T(t) = T_0 \pm \Delta T(1 - e^{\frac{-t}{\tau_{ccr}}}) \tag{5.1}$$

  with:
  - T(t)is the temperature at time t.
  - T_0 is the temperature at t=0.
  - ΔT = is the difference between the final temperature and T_0.
  - τ_{ccr} is the CCR thermal constant.

- The χ^2 square has three degrees of freedom: T_0, ΔT and τ_{ccr}.

So the code searches the τ_{ccr} that minimizes the χ^2 square function setting as initial values for T_0, ΔT the experimental value, then for each phase it repeats the computation 250 times with a bootstrap cycle and the average τ_{ccr} with its standard deviation are respectively the τ_{ccr} computed by fit with its error (the values that will be shown in the plots). In order to investigate in detail the temperature gradient on the CCR front face we carried out a different analysis. We used eight small areas (3x3 pixels) on the CCR surface: three located near the tabs (AR01 near the left tab, AR02 near the upper tab, AR03 near the lower tab), one in the center (AR04), three located near the edges of the CCR face between the tabs (AR05 near the upper edge, AR06 near the right edge, AR07 near the lower edge) and the last one, AR08, positioned close to the upper tabs, near the AR02, as shown in Figure 5.17b. The AR08 has been chosen because the comparison with AR02, could tell us how sensitive the data is slightly offset positions.
Then we computed and plotted the temperature difference between the average temperatures of each area and the central area AR04. The error bar of each point is given by the r.m.s. of the average value within the area computed by the FLIR codes, $\pm$0.5K, this error bar will not be displayed in the gradients plots in order to

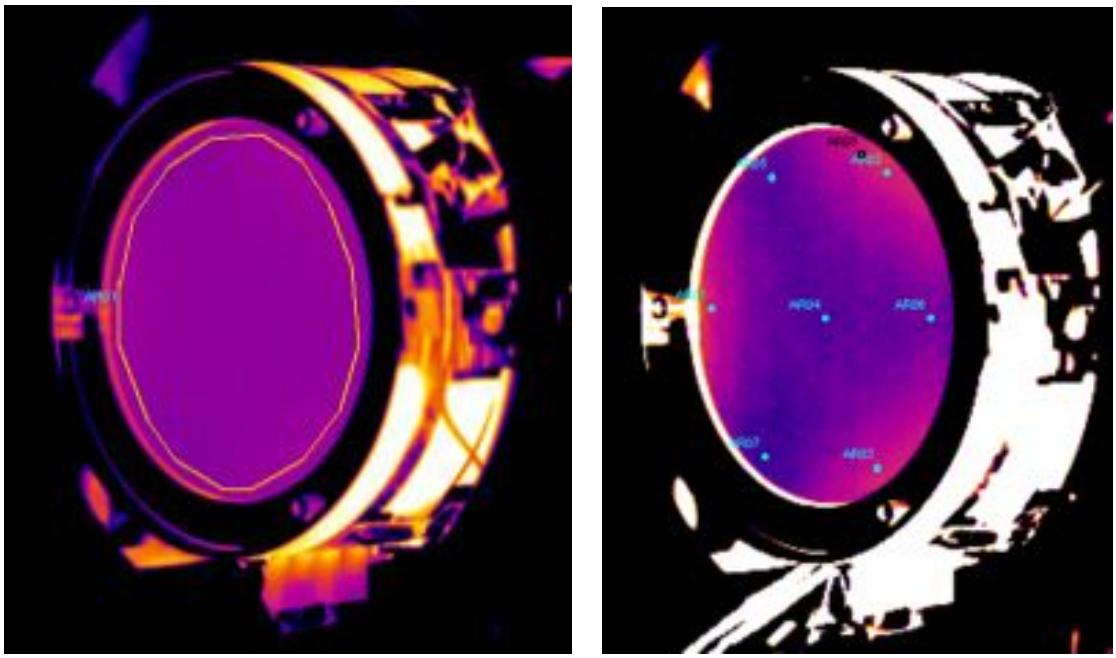

(a) *Sample of MoonLIGHT IR picture with in evidence the area used for the analysis .*

(b) *IR image of MoonLIGHT for the analysis with eight areas.*

Figure 5.17: MoonLIGHT-2 IR analysis example for front face average temperature value and front face temperature gradient

simplify the plot reading. The main plots tests results (τ_{ccr} and ΔT analysis) will be reported in sections 5.3.1 for the first test campaign and in 5.3.2 for the second campaign, while the overall thermal results will be discussed in 5.4.

5.3.1 1^{st} SCF Test campaign

SCF-Test at 300K sun incidence $0°$

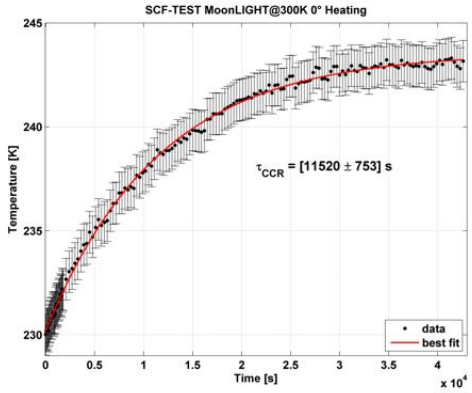

(a) τ_{ccr} *heating phase.*

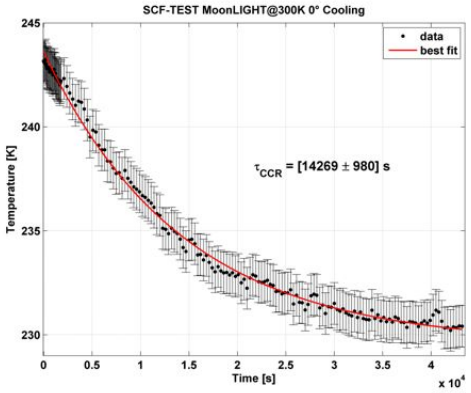

(b) τ_{ccr} *cooling phase.*

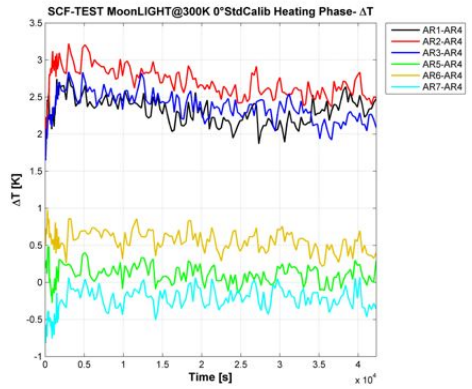

(c) *Front face gradient heating phase.*

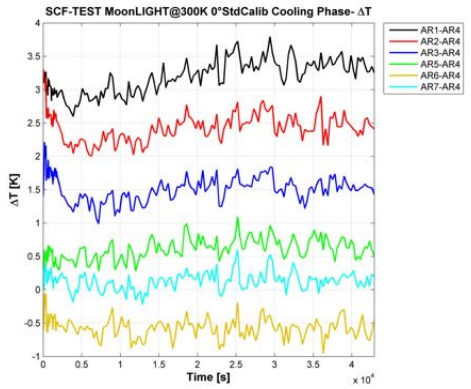

(d) *Front face gradient cooling phase.*

Figure 5.18: MoonLIGHT-2 SCF-Test at 300K, sun incidence 0°, IR analysis result. First test campaign

SCF-Test at 300K sun incidence 30°

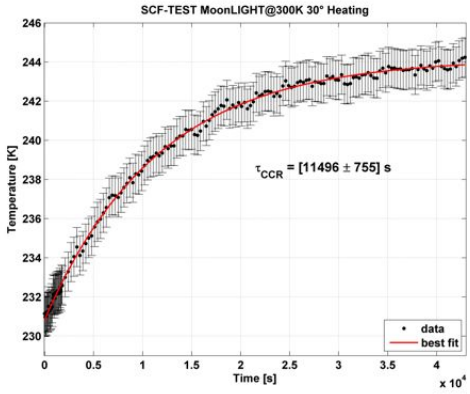

(a) *τ_{ccr} heating phase.*

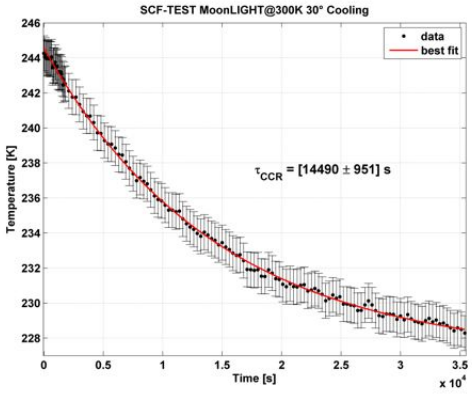

(b) *τ_{ccr} cooling phase.*

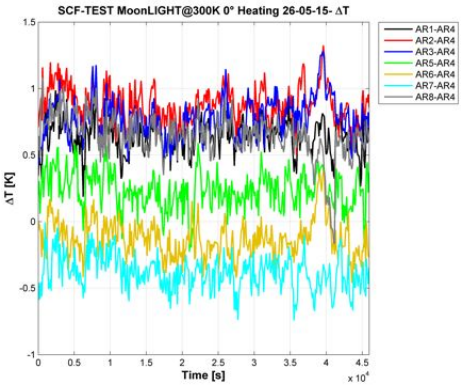

(c) *Front face gradient heating phase.*

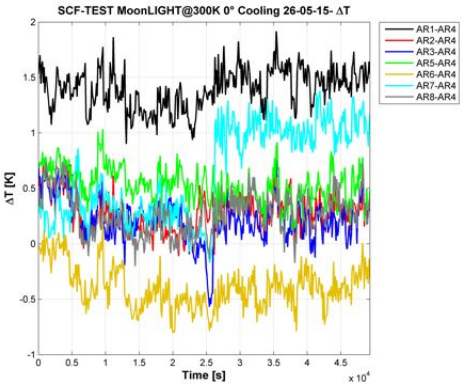

(d) *Front face gradient cooling phase.*

Figure 5.19: MoonLIGHT-2 SCF-Test at 300K, sun incidence 30°, IR analysis result. First test campaign

5.3.2 2^{nd} SCF Test campaign

SCF-Test at 250K sun incidence $0°$

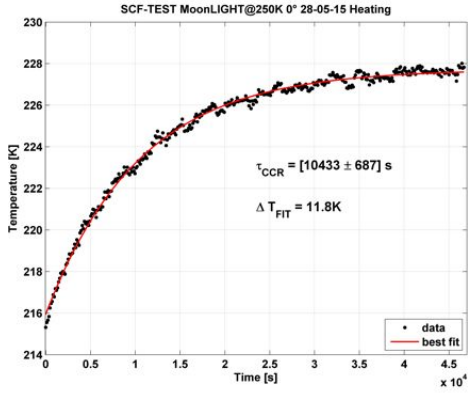

(a) τ_{ccr} *heating phase.*

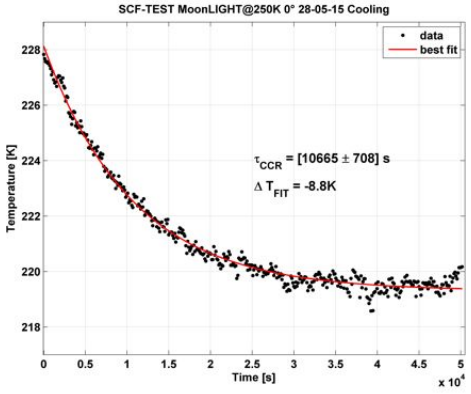

(b) τ_{ccr} *cooling phase.*

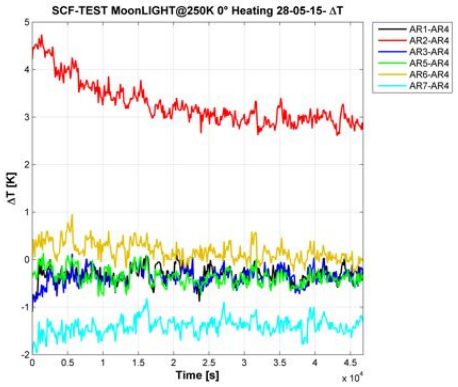

(c) *Front face gradient heating phase.*

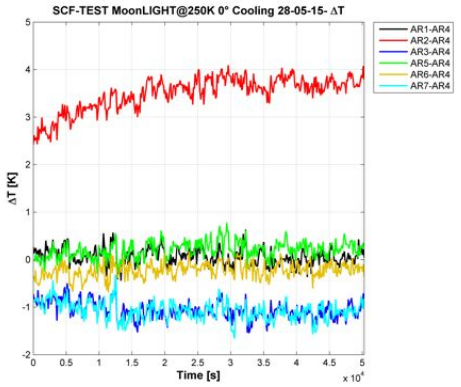

(d) *Front face gradient cooling phase.*

Figure 5.20: MoonLIGHT-2 SCF-Test at 250K, sun incidence 0°, IR analysis result. Second test campaign

SCF-Test at 300K sun incidence 0°

Due to an IR Therma-cam acquisition issue, we lost around 1h of data in SUN ON and another 1h in SUN OFF. However the analysis was still possible, so the plots below will show all data available except for the missing hours.

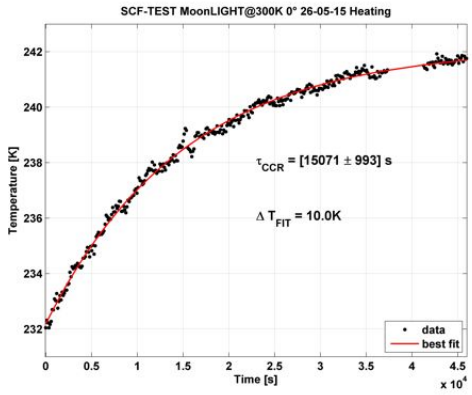

(a) τ_{ccr} *heating phase.*

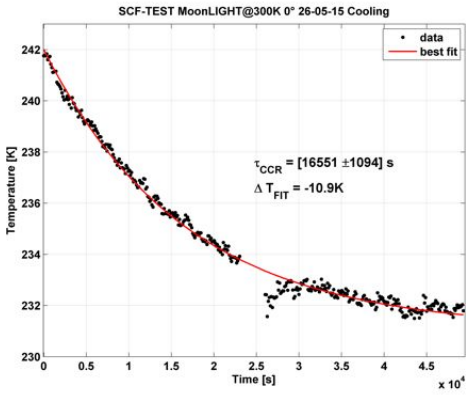

(b) τ_{ccr} *cooling phase.*

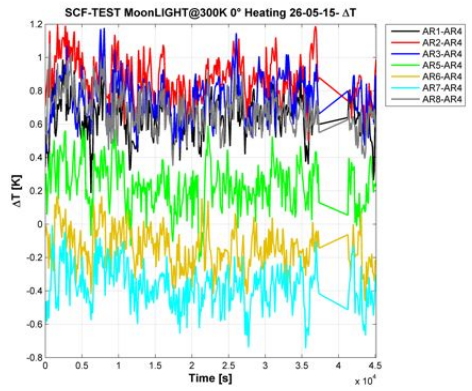

(c) *Front face gradient heating phase.*

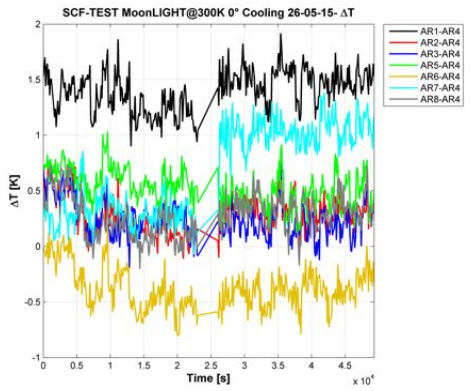

(d) *Front face gradient cooling phase.*

Figure 5.21: MoonLIGHT-2 SCF-Test at 300K, sun incidence 0°, IR analysis result. Second test campaign

SCF-Test at 330K sun incidence 0°

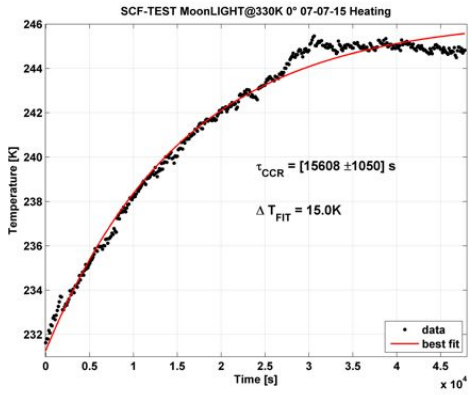

(a) τ_{ccr} *heating phase.*

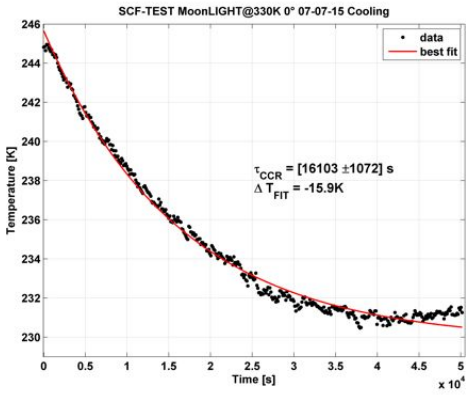

(b) τ_{ccr} *cooling phase.*

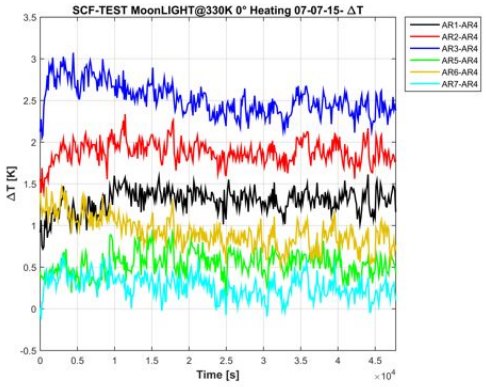

(c) *Front face gradient heating phase.*

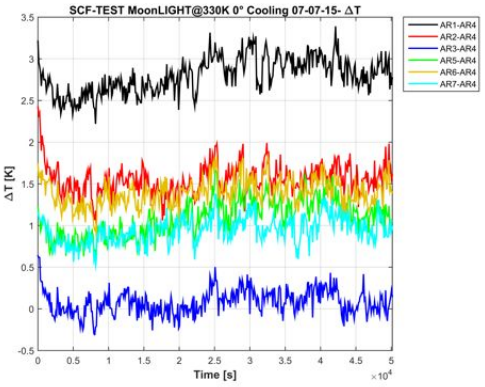

(d) *Front face gradient cooling phase.*

Figure 5.22: MoonLIGHT-2 SCF-Test at 330K, sun incidence 0°, IR analysis result. Second test campaign

5.4 Conclusions

Optical results

We can try and draw some conclusions about the MoonLIGHT SCF-Tests performed in 2015 at SCF_Lab. For the 300 K case, we notice the following:

- Before Sun ON phase (Figure 5.9), CCR FFDP resembles what is expected from optics principles and simulations - energy is mostly located at the centre of the pattern, but is also extends towards the edges, fading out.
- Just after Sun OFF phase (Figure 5.10) and until the end of the test (Figure 5.11), one can see that, due to the thermal stimulation operated during Sun ON phase, energy has now been spread all over the pattern area.
- The spreading of energy due to thermal stimulation also affects the average intensity at operational range (4.0-4.5 μrad) as a function of time, during the SCF-Test (Figure 5.12) - after an initial raise, intensity levels off to about 40 millions square meters.

For the 250 K case, we notice the following:

- Before Sun ON phase (Figure 5.13), CCR FFDP resembles what is expected from optics principles and simulations - energy is mostly located at the centre of the pattern, but is also extends towards the edges, fading out.
- Just after Sun OFF phase (Figure 5.14) and until the end of the test (Figure 5.15), one can see that, despite the thermal stimulation operated during Sun ON phase, energy has not been considerably spread all over the pattern area.
- The eventual spreading of energy due to thermal stimulation also affects the average intensity at operational range (4.0-4.5 μrad) as a function of time, during the SCF-Test (Figure 5.16) - there is the usual initial raise, due to abrupt readjustment of the CCR, which is not anymore exposed to solar constant, and then the intensity levels off to about 130 millions square meters.

We conclude that the thermal environment is crucial for MoonLIGHT's correct operational activity. MoonLIGHT's housing and CCR specs have to be correctly addressed in order to ensure return of light to ground laser ranging stations. There are hints for open issues especially related to ensure MoonLIGHT stability at any reasonable operational temperature.

Thermal results

All test results reported in plots from 5.18a to 5.22d are summarized in table 5.1 for the first test campaign and 5.2 for the second one. The average τ_{ccr} between SUN ON and SUN OFF is computed using the average between the two single τ_{ccr} (heating and cooling) weighted with their errors while the error is the std deviation of the single values.

Table 5.1: First SCF-Test Campaign: IR analysis test results

300K: 0° **sun incidence**	**300K:** 30° **sun incidence**
τ_{ccr} heating = [11520 ± 753]s	τ_{ccr} heating = [11496 ± 755]s
τ_{ccr} cooling = [14269 ± 980]s	τ_{ccr} heating = [14490 ± 951]s
τ_{ccr} average = [13075 ± 1944]s	τ_{ccr} average = [13165 ± 2117]s
ΔT maximum = [4.7 ± 1.0]	ΔT maximum = [5.3 ± 1.0]

The τ_{ccr} analysis shows some considerably long values, as expected. The long thermal constant will provide a good thermal isolation between the CCR and the lunar regolith providing a good stability during the 14 hours night time. However the reduction of housing temperature does not increase the time constant as from theory, this fact in addiction with the quite large front face temperature gradient (respect to the thermal simulations) can suggest a thermal conductance between CCR and housing. This effect is visible even in the thermal gradient analysis. This plots in fact show that, as reported in figure 5.17b, there are hot areas near the tab, where the screws hold the CCR to the structure. After the first test campaign we added the copper tape in order to reduce the conductivity and the second tests campaign

250K: 0° **sun incidence**	**300K:** 0° **sun incidence**
τ_{ccr} heating = [10433 ± 687]s	τ_{ccr} heating = [15071 ± 993]s
τ_{ccr} cooling = [10655 ± 708]s	τ_{ccr} heating = [16551 ± 1094]s
τ_{ccr} average = [10551 ± 164]s	τ_{ccr} average = [15847 ± 1046]s
ΔT maximum = [6.4 ± 1.0]	ΔT maximum = [3.0 ± 1.0]
330K: 0° **sun incidence**	
τ_{ccr} heating = [15608 ± 1050]s	
τ_{ccr} heating = [16103 ± 1072]s	
τ_{ccr} average = [15858 ± 1501]s	
ΔT maximum = [3.1 ± 1.0]	

Table 5.2: Second SCF-Test Campaign: IR analysis test results

shows a reduced thermal gradient (as comparison between the two SCF-Test at 300 K) and a slightly long thermal constant.

Overall conclusions

The results shows that MoonLIGHT-2 can provide a mm-accuracy during lunar night. This is because the SUN-ON phase FFDPs are in good agreement with the simulations as shown by the longer τ_{ccr} and the reduced thermal gradient. Further analysis will be done in order to ensure the operatively phase not only during lunar night but also during lunar day time. However from the simulations reported in 4.3.1 we can see that we can obtain good GR results (see chapter 6) improvement using the payload even during the lunar night alone.

Chapter 6

Data analysis and simulation

6.1 The Planetary Ephemeris Program (PEP)

In order to analyze LLR data we use the PEP software, developed by the Center for Astrophysics (CfA), by I. Shapiro et al. starting from 1970s.
PEP was designed not only to generate ephemerides of the Planets and the Moon, but also to compare model with observations. One of the early uses of this software was the first measurement of the geodetic precession of the Moon [15]. There are several sets of observations that PEP can handle (LLR, radar ranging and doppler, optical positional measurements, transponder measurements, pulsar timing data, etc). Since we are interested primarily on LLR observations, I'll describe the components of a round-trip range prediction, though most of the steps along the way are common to other observables as well.
In order to compute the range observable (transmit and receive time) at some epoch, PEP's capabilities are the following:

- Determine the positions and velocities of the centers of mass of the Sun, planets, Pluto, and Earth-Moon barycenter by integrating their equations of motion

- Integrate the equations of motion for the Moon, Moon rotation and Earth (but not Earth rotation)
- Determine the asteroid positions from an elliptic approximation (rather than from integrated equations of motion)
- Calculate the displacement of the lunar reflector with respect to the center of mass of the Moon
- Calculate the displacement of the ranging station with respect to the center of mass of the Earth
- Treat photon propagation effects
- PEP also allows us to find a constant bias term for any specified span of data

In particular, we are primarily interested in LLR observations. By this purpose, the software is able to calculate the residuals of the distances between observed LLR data and computed data, derived from expectations of GR and of terrestrial and lunar Geodesy. We have performed a very preliminary analysis of LLR data from three stations: McDonald Observatory in Texas (USA), Grasse in France and APOLLO in New Mexico (USA). The latter station provides the best quality data since 2006. On March 25, 2010, the Matera Laser Ranging Observatory in Italy (MLRO, led by G. Bianco) recorded LLR echos from the array of Apollo 15.
The histograms in Fig. 6.1 show photon-by-photon data and are used to form a single LLR "normal point" of the Apollo 15 array taken by the APOLLO station (led by T. W. Murphy) on November 19, 2007. A normal point contains several information e.g. date of observation, atmospheric conditions, as well as time of flight, data quality and CCR arrays. The APOLLO instrumental accuracy (in terms of laser, detector, timing electronics, etc) shown by the fiducial returns in Fig. 6.1 is a root mean square contribution of 120 ps (18 mm).

From a comparison between the middle and the lower plots we can see how the tilt in the arrays affects the accuracy of the ranging measurements. The model parameter estimates are refined by minimizing the residual differences, in a weighted

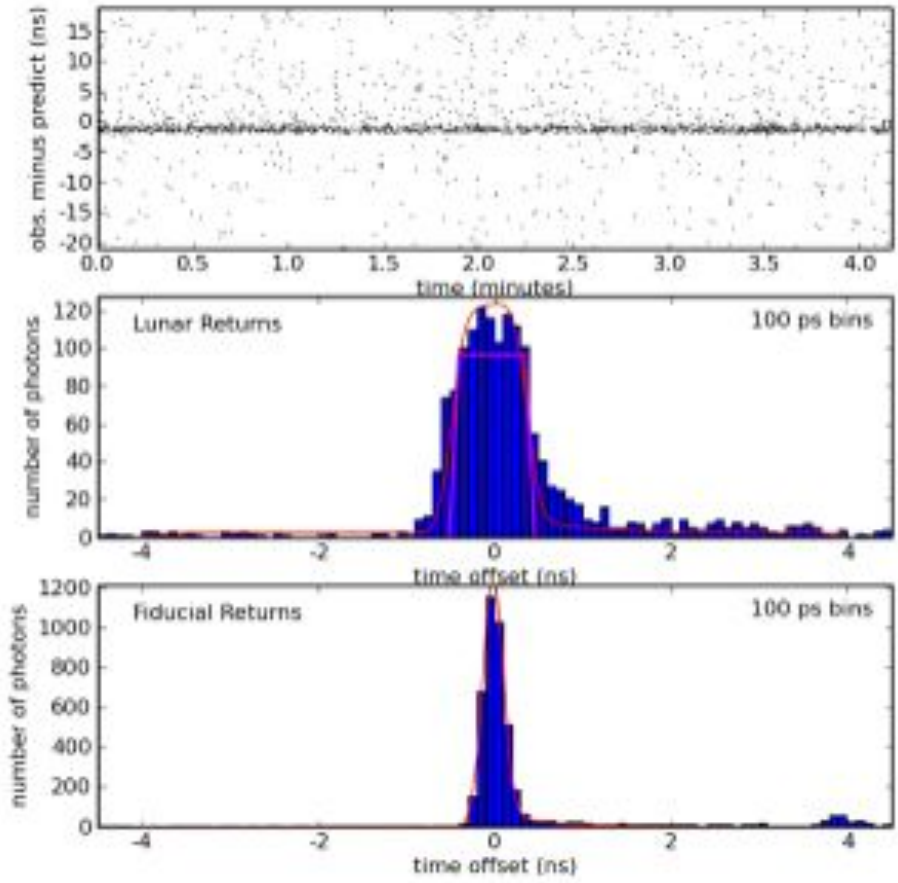

Figure 6.1: Example run of Apollo 15. In the plot, the top panel shows a 40 ns window of observed round trip time minus the predicted range. Background noise and detector dark current appear as scattered dots, while the lunar return is in the middle. The middle panel shows a histogram of the lunar returns, while the bottom panel shows the local "fiducial" CCR return, fitted by the red Gaussian. The Lunar return is additionally spread by the tilted reflector array modeled by the superimposed magenta trapezoidal shape [16].

least-squares sense, between observations (O) and model predictions (C, stands for "Computation"), O-C. "Observed" is round-trip time of flight. "Computed" is modeled by the PEP software. PEP software has enabled constraints on departures from standard physics. For example, it has been used to place limits on the PPN parameters β and γ, geodetic precession and the variation of the gravitational constant, $\frac{\dot{G}}{G}$ [17], [18], [19].
Before describing the various facets of the ephemeris calculation, it is worthwhile to spend a moment to describe the frame of reference in which PEP calculations are carried out. PEP asserts that the solar system barycenter frame is an inertial frame. Thus far, there is no evidence to suggest otherwise.
Although the forces are calculated in the solar system barycenter frame, PEP reports the positions and velocities of the solar system bodies with respect to the Sun's center of mass (Solar System Barycenter, SSB). The heliocentric coordinates of the solar system barycenter are also computed. Nevertheless, the physics is performed in the (inertial) solar system barycenter frame; the heliocentric coordinates are derived quantities.

6.1.1 N-Body integration

If we consider all solar system bodies to be point masses, and assume that the only force in town is gravity, then the positions and velocities of those bodies as a function of time can be determined from a numerical integration of the Einstein-Infeld-Hoffman equations of motion. With one caveat (solar oblateness, as parametrized by the gravitational spherical harmonic J2), this is exactly what PEP does. The equations of motions are expanded to first PPN order which includes $(v/c)^2$ terms (since no $(v/c)^3$ terms exist in the PPN expansion, the equations of motion are good to third order in v/c). No post-post-Newtonian terms (of order $(v/c)^4$) are included. The following point-mass bodies are included in the n-body integration: the Sun, the barycenter of the Earth-Moon system, the seven non-Earth planets, and Pluto. The asteroids are included only as perturbing bodies in the n-body integration [23], [24]. The treatment of asteroids is described in 6.1.2

6.1.2 Asteroids

The asteroids are challenging to model, mostly because there are so many of them. However, much of the mass of the asteroid belt lies in only a few large asteroids. The largest asteroid, Ceres (like Pluto, Ceres is currently classified as a dwarf planet) has a diameter of 950 km and contains about 32% of the mass of the asteroid belt. In fact more than half of the mass of the asteroid belt is contained in the four largest objects: Ceres, 4 Vesta, 2 Pallas and 10 Hygiea. Eight asteroids (Ceres, Pallas, Juno, Vesta, Hebe, Iris, Eunomia and Psyche) are treated individually. Their masses are fit parameters, but their orbits are assumed to be known and are computed from an elliptic approximation. The next 90 most-important individual asteroids are classified into five sub- categories based on their spectral type (based on observed properties such as color, albedo and spectral shape). Each sub-category has a single density parameter that is fit for it. The asteroid volumes are taken from radiometric observations, and in some cases stellar occultation measurements. The volumes are not fit parameters. The remaining mass of the asteroid belt is modeled as an infinitesimally thin circular ring with constant linear density and known radius. The mass of the ring is a fit parameter. The selection criterion for these asteroids was not mere size, but rather the estimated amplitude of periodic signatures induced in the orbits of Earth and Mars.

6.1.3 Earth and Moon rotation

The position and velocity of the Earth-Moon barycenter is determined through the n-body integration described above. The coordinates of the Moon and Earth need to be determined separately. Furthermore, the rotation of the Moon must also be computed. It turns out that models of the Earth orientation are not accurate enough, and so the Earth orientation is instead obtained by the International Earth Rotation Service (IERS). The equations of motion of the Earth and Moon are simultaneously integrated using the solar system as determined from the n-body integration above. Of course, this affects the position of the Earth-Moon barycenter, which in turn affects the coordinates of the n-body integration [25], [26], [27]. As a result, the

n-body integration and the Earth-Moon integration must be iterated (typically 3 times) until some convergence criteria is met. The Earth and Moon equations of motion allow for the inclusion of ten orders of gravitational harmonics (both zonal and tesseral). In practice, however, only the first four orders are used, and only the first three are fitted parameters (the fourth is a fixed parameter). The spherical harmonic, $Y_l^m(\mu, \phi) = f(l, m)e^{im\phi}P_l^m(cos\mu)$, has degree l and order m. If m = 0, then the spherical harmonic is independent of ϕ (does not depend on longitude) and is called a zonal harmonic. Harmonics for which $l = |m|$ have no zero crossings in latitude and are called sectoral harmonics. The rest, which checker the sphere, are called tesseral harmonics. The equations of motion of the Moon involve coupled differential equations for the Moon and the Moon rotation. The lunar rotation model includes the effects of a solid-body tidal term. The lunar model includes only the gravitational harmonics. There is no provision for a liquid core/solid mantle or for dissipation at that boundary.

6.1.4 Site and spot motion

The location of the transmit/receive site on the Earth is specified by latitude, longitude and radius (all three of which are typically fit parameters). Similarly, the reflecting spot on the Moon is specified in selenographic coordinates. Solid body tides deform the shape of the Earth and Moon, and so the site and spot coordinates are corrected for this motion. At present, solid-body tides are the only adjustments made to the site and spot vectors. An obvious upgrade to the site displacement would be to include plate motion (plate tectonics). The lithospheric plates are known to move with speeds of 5-10 cm/year.

6.2 PEP computation

PPN parameter β, γ and η

In PPN gravity, the parameter gamma parametrizes the amount of spacetime curvature per unit mass, and the parameter beta parametrizes the non-linearity of gravity. In General Relativity, beta and gamma are exactly unity.
In the late 1960s, Kenneth Nortvedt showed that a violation of the Strong Equivalence Principle (SEP) could be parametrized by the parameter η, where:

$$\eta = 4 \times \beta - \gamma - 3 \tag{6.1}$$

In GR $\eta = 0$.
PEP can be used to derive constraints on the PPN parameters beta and gamma, as well as on eta. The way that these parameters appear in PEP is sufficiently complicated to warrant further description. In PEP, there are actually two sets of PPN beta and gamma parameters: in this case we will call them (beta, gamma) and (beta', gamma'). In PEP the designators for these parameters are (PRMTER(41), PRMTER(42)) and (PRMTER(43), PRMTER(44)), respectively.
The existence of two sets of beta and gamma parameters results from the historical development of PEP. Originally, (beta, gamma) were included in the equations of motion, but the SEP was not implemented. Later, however, the Nordtvedt effect was added to PEP. In order to maintain backwards compatibility, a new, separate pair of parameters (beta', gamma') was introduced. The original (beta, gamma) pair does not control the SEP violation, and (beta', gamma') appear only in the SEP terms. However, the partial derivatives of (beta', gamma') are calculated as if they did both tasks (even though they do not).
In PEP, the Nordtvedt eta parameter appears in the following way:

$$\eta \times \Delta = (4 \times \beta' - \gamma' - 3) \times \Delta + (\eta \times \Delta)' \tag{6.2}$$

It turns out that PEP does not estimate η alone; it estimates the $(\eta \times \Delta)'$ product (in addition to estimating β' and γ'). Δ is the ratio of the gravitational self-energy (U) to the total mass-energy (Mc^2) of the body in question:

$$\Delta = \frac{U}{Mc^2} \tag{6.3}$$

There is an $\eta \times \Delta$ term for each body because Δ is body-dependent.

Geodetic precession

One of the consequences of GR is that the orbital plane of a planetary satellite precesses about the plane of the planet's orbit. This effect, known as geodetic precession, was pointed out by De Sitter in 1916. In the case of Earth satellites (such as the Moon), this rate is about 2 arcseconds per century. There is also an advance of perigee analogous to Mercury's perihelion advance (cfr 2.1.1), but the latter is orders of magnitude smaller because it depends on Earth's mass rather than the Sun's one.
Inside PEP, the equations of motion are cast in terms of the Newtonian accelerations plus relativistic terms with coefficients composed by β and γ. There is also an arbitrary scale factor λ multiplying all the relativistic terms, and all of these parameters are programmed in variational equations so that any of them can be estimated by least-squares analysis of observation residuals. Thus, for PEP, any departure of β or γ from unity is equal to a violation of GR. On the other hand, any departure of λ from unity means a breakdown of PPN formalism.
In the same way, it is possible to add an ad hoc term to the equations of motion with an adjustable scale factor (called h) nominally zero, such as an extra precession of the Moon's node. The parameter h is the key element of our study since it is a measure of the (dis)agreement between the observed motion of the Moon and the De Sitter precession. Inside PEP the equations of motion are formulated in a coordinate system rotating in the instantaneous ecliptic at a (variable) rate $h\Delta\Omega$, where $\Delta\Omega$ is the de Sitter precession rate. Any departure in the lunar motion from

the de Sitter rate is characterized by the numerical factor h, where $h = 0$ would be consistent with the prediction from GR and $h = 1$ would imply a 100% error in this prediction [28], [29], [30], [31].

6.3 Simulations

I have performed a number of numerical simulations in order to develop and optimize the design of MoonLIGHT type CCR in time for their deployment on the lunar surface[1].
For these simulations I have used every LLR data available until 2014 (fig.6.2) plus dummy observations on MoonLIGHT-2 CCR.

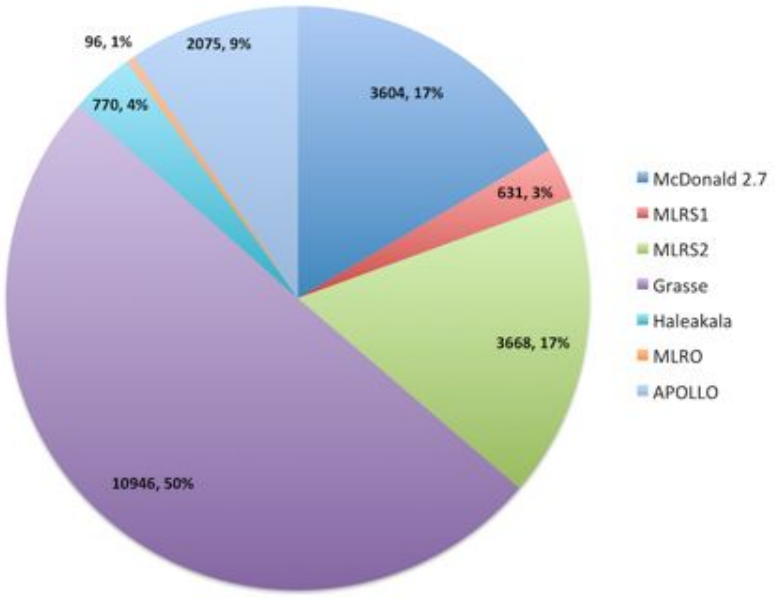

Figure 6.2: LLR data available until 2014

All the dummy observations were computed by PEP after defining CCRs positions on the lunar surface (fig.6.3) and the accuracy of the ranging data (table 6.1).

[1]The first mission will be in 2016 with the Moon Express mission (agreement signed on May 15^{th} 2015)

CCR Array	Stations	Position	Cadence	Accuracy [ps]		
				STD	Double STD	Half STD
Apollo	APOLLO	AP 11,14,15	30	16	32	8
	CERGA		14	33	66	16.5
	MLRS		20			
	MLRO		8			
MoonLIGHT-2	APOLLO	80N, 80S, 80E, 80W	30	3	6	1,5
	CERGA		14	7	14	3.5
	MLRS		20			
	MLRO		8			

Table 6.1: Parameter and relative accuracy used for dummy data

As shown in Table 6.1, I have used three different sets of parameters for the dummy observations.
For the simulated observations, the round-trip timing uncertainties are:

- STD: 16 ps for APOLLO and 33 ps for other sites on existing reflectors, and 3 ps for APOLLO and 7 ps for other sites on the proposed reflectors
- Double STD: 32 ps for APOLLO and 66 ps for other sites on existing reflectors, and 6 ps for APOLLO and 14 ps for other sites on the proposed reflectors
- Half STD: 8 ps for APOLLO and 16.5 ps for other sites on existing reflectors, and 1.5 ps for APOLLO and 3.5 ps for other sites on the proposed reflectors

The assumed accumulation of future data is calculated with a cadence of 30 days for APOLLO, 20 days for MLRS, 14 days for CERGA, and 8 days for MLRO. The results obtained with the simulations are shown in tables 6.2, 6.3, 6.4.

The σ reported in the results is the purely statistical uncertainty in the estimation of parameters, assuming no systematic errors in the data or imperfections in the model. It is better to talk about the PEP solution values as "estimates", rather than "measurements", and therefore it is better to talk about of the "uncertainty"

Year	$\sigma[\beta]$	$\sigma[\gamma]$	$\sigma[\dot{G}/G]$	$\sigma[h]$
2015	1.30×10^{-5}	5.22×10^{-5}	2.20×10^{-14}	1.37×10^{-4}
2018	7.06×10^{-6}	2.84×10^{-5}	1.54×10^{-14}	1.04×10^{-4}
2019	6.22×10^{-6}	2.50×10^{-5}	1.40×10^{-14}	8.27×10^{-5}
2020	5.22×10^{-6}	2.10×10^{-5}	1.23×10^{-14}	6.87×10^{-5}
2021	4.40×10^{-6}	1.77×10^{-5}	1.03×10^{-14}	5.75×10^{-5}
2022	3.60×10^{-6}	1.45×10^{-5}	8.30×10^{-15}	4.35×10^{-5}
2023	3.10×10^{-6}	1.26×10^{-5}	6.84×10^{-15}	3.31×10^{-5}
2024	2.80×10^{-6}	1.14×10^{-5}	5.89×10^{-15}	2.80×10^{-5}
2025	2.52×10^{-6}	1.03×10^{-5}	5.12×10^{-15}	2.57×10^{-5}
2026	2.27×10^{-6}	9.32×10^{-6}	4.45×10^{-15}	2.27×10^{-6}
2027	2.03×10^{-6}	8.36×10^{-6}	3.85×10^{-15}	2.08×10^{-6}
2028	1.87×10^{-6}	7.68×10^{-6}	3.36×10^{-15}	1.90×10^{-5}
2029	1.75×10^{-6}	7.15×10^{-6}	2.99×10^{-15}	1.78×10^{-5}
2030	1.66×10^{-6}	6.79×10^{-6}	2.88×10^{-15}	1.73×10^{-5}
2031	1.57×10^{-6}	6.39×10^{-6}	2.50×10^{-15}	1.59×10^{-5}

Table 6.2: Results of expected uncertainty improvements with STD accuracy set

Year	$\sigma[\beta]$	$\sigma[\gamma]$	$\sigma[\dot{G}/G]$	$\sigma[h]$
2015	1.30×10^{-5}	5.22×10^{-5}	2.20×10^{-14}	1.37×10^{-4}
2018	8.32×10^{-6}	3.34×10^{-5}	1.69×10^{-14}	1.19×10^{-4}
2019	7.44×10^{-6}	2.99×10^{-5}	1.59×10^{-14}	1.07×10^{-4}
2020	6.54×10^{-6}	2.63×10^{-5}	1.47×10^{-14}	9.16×10^{-5}
2021	5.96×10^{-6}	2.39×10^{-5}	1.35×10^{-14}	8.31×10^{-5}
2022	5.19×10^{-6}	2.09×10^{-5}	1.18×10^{-14}	7.03×10^{-5}
2023	4.67×10^{-6}	1.88×10^{-5}	1.04×10^{-14}	5.77×10^{-5}
2024	4.32×10^{-6}	1.75×10^{-5}	9.39×10^{-15}	5.02×10^{-5}
2025	4.00×10^{-6}	1.62×10^{-5}	8.34×10^{-15}	4.63×10^{-5}
2026	3.66×10^{-6}	1.48×10^{-5}	7.46×10^{-15}	4.11×10^{-5}
2027	3.31×10^{-6}	1.34×10^{-5}	6.61×10^{-15}	3.79×10^{-5}
2028	3.08×10^{-6}	1.24×10^{-5}	5.95×10^{-15}	3.56×10^{-5}
2029	2.86×10^{-6}	1.16×10^{-5}	5.41×10^{-15}	3.37×10^{-5}
2030	2.71×10^{-6}	1.10×10^{-5}	5.08×10^{-15}	3.27×10^{-5}
2031	2.54×10^{-5}	1.02×10^{-5}	4.63×10^{-15}	3.04×10^{-5}

Table 6.3: Results of expected uncertainty improvements with Double STD accuracy set

Year	$\sigma[\beta]$	$\sigma[\gamma]$	$\sigma[\dot{G}/G]$	$\sigma[h]$
2015	1.30×10^{-5}	5.21×10^{-5}	2.20×10^{-14}	1.37×10^{-4}
2018	5.76×10^{-6}	4.31×10^{-5}	1.33×10^{-14}	7.98×10^{-5}
2019	4.71×10^{-6}	1.89×10^{-5}	1.11×10^{-14}	5.84×10^{-5}
2020	3.66×10^{-6}	1.47×10^{-5}	8.90×10^{-15}	4.74×10^{-5}
2021	2.85×10^{-6}	1.14×10^{-5}	6.69×10^{-15}	3.57×10^{-5}
2022	2.22×10^{-6}	8.89×10^{-6}	4.92×10^{-15}	2.44×10^{-5}
2023	1.91×10^{-6}	7.82×10^{-6}	3.88×10^{-15}	1.78×10^{-5}
2024	1.73×10^{-6}	7.14×10^{-6}	3.29×10^{-15}	1.49×10^{-5}
2025	1.58×10^{-6}	6.58×10^{-6}	2.85×10^{-15}	1.36×10^{-5}
2026	1.44×10^{-6}	5.99×10^{-6}	2.46×10^{-15}	1.19×10^{-5}
2027	1.32×10^{-6}	5.47×10^{-6}	2.09×10^{-15}	1.11×10^{-5}
2028	1.24×10^{-6}	5.12×10^{-6}	1.80×10^{-15}	1.00×10^{-5}
2029	1.17×10^{-6}	4.81×10^{-6}	1.58×10^{-15}	9.29×10^{-6}
2030	1.11×10^{-6}	4.57×10^{-6}	1.46×10^{-15}	9.00×10^{-6}
2031	1.07×10^{-6}	4.35×10^{-6}	1.30×10^{-15}	8.21×10^{-6}

Table 6.4: Results of expected uncertainty improvements with Half STD accuracy set

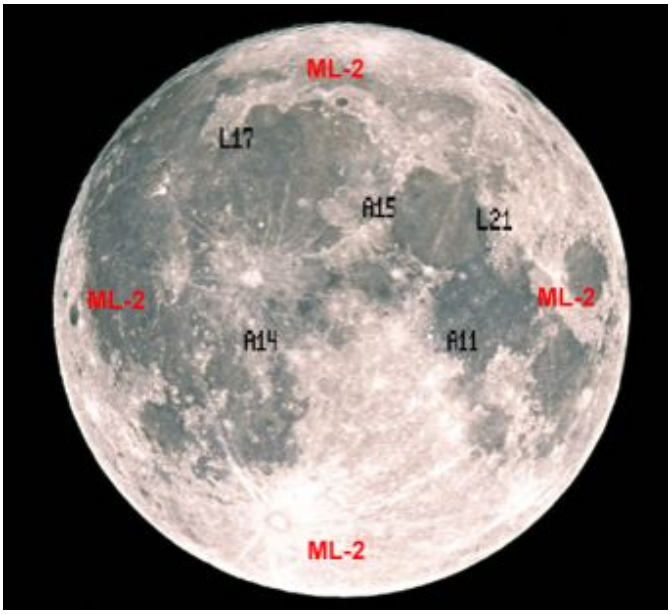

Figure 6.3: CCRs position on the lunar surface

of the values, rather than their "accuracy". However, the main point is that the sigma put out by PEP is a formal uncertainty and not always a realistic uncertainty. The ultimate scientific objective of MoonLIGHT-2 is to provide constraints in the theories that are proposed to determine the properties of other gravitational theories [20]. This improved precision will be useful to identify the theoretical directions that will further the development of an understanding of these phenomena that lie beyond our current understanding. Looking at the obtained preliminary results, no parameter here attains the best-case improvement of table 6.5.

This is because the results show the pessimistic case of a minimal number of MoonLIGHTs deployed in non-optimal locations with current, non-upgraded laser station hardware and, most of all, with current version of the orbit software which only supports a total LLR error budget on the order of a cm.
Most of all, figures 6.4, 6.5, 6.6, 6.7 and 6.8 do not include the updates, optimizations and improvements of any current orbit software that will have to be implemented, and that will be possible to implement, as the LLR instrumental accuracy will im-

Parameter	Accuracy (cm)	Accuracy (1mm)	Accuracy (0.1mm)
PPN, β	1.1×10^{-4}	10^{-5}	10^{-6}
WEP	1.4×10^{-13}	10^{-14}	10^{-15}
SEP	4.4×10^{-4}	3×10^{-5}	3×10^{-6}
$\dot{G}/G$	9×10^{-13}	5×10^{-4}	5×10^{-15}
$1/r^2$	3×10^{-11}	10^{-12}	10^{-13}
Geodetic Precession	6.5×10^{-3}	6.5×10^{-4}	6.5×10^{-5}

Table 6.5: GR science objectives and measurements. 2^{nd} column shows current situation and measurements from [21]. Column 3 and 4 show expectations in the ideal, best-case scenario.

prove thanks to the progressive deployment of MoonLIGHT CCRs on the Moon and thanks to the progressive upgrades of the LLR ground stations and/or additions of new LLR ground stations.

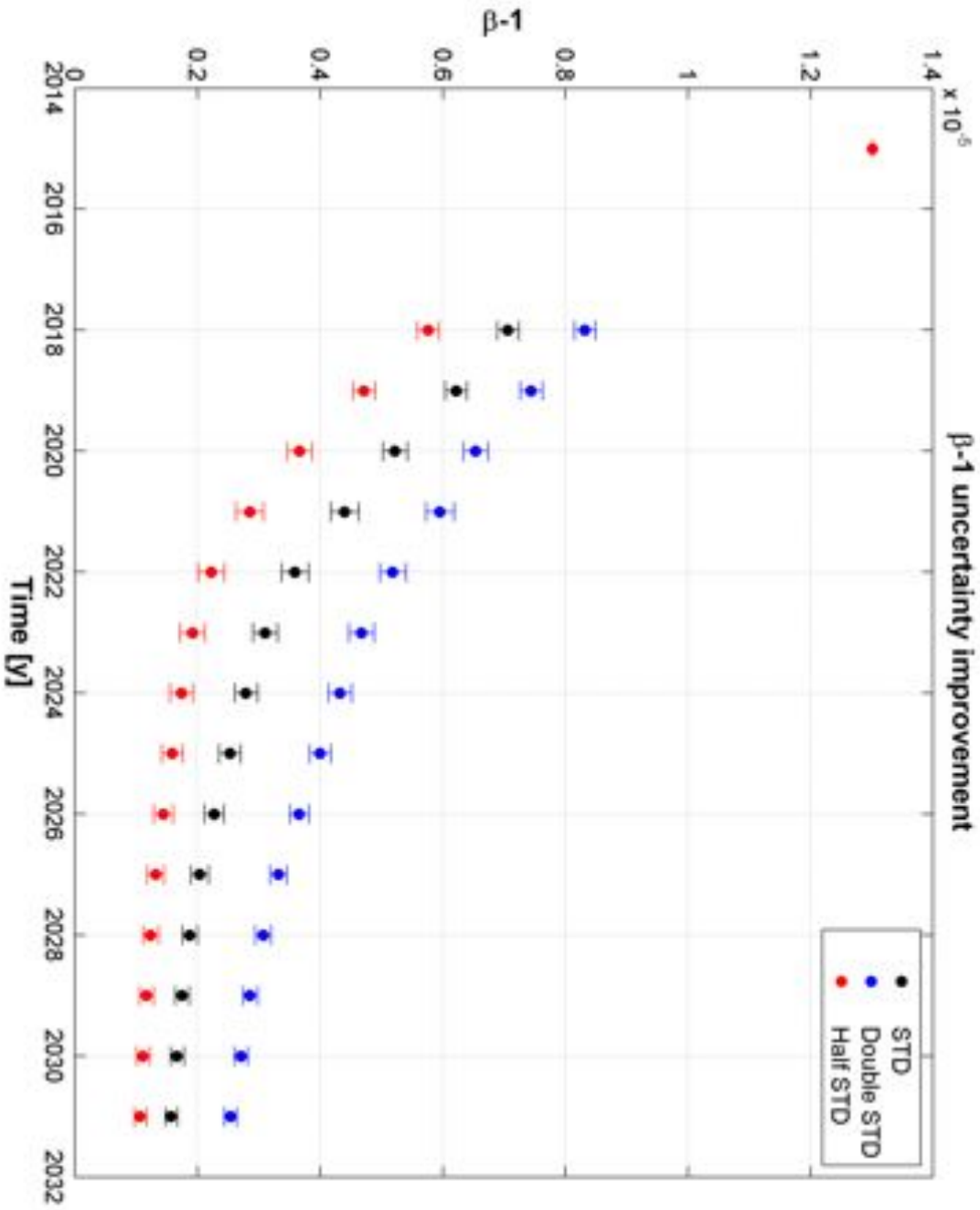

Figure 6.4: β uncertainty improvement during a long time simulation using MoonLIGHT-2 CCRs

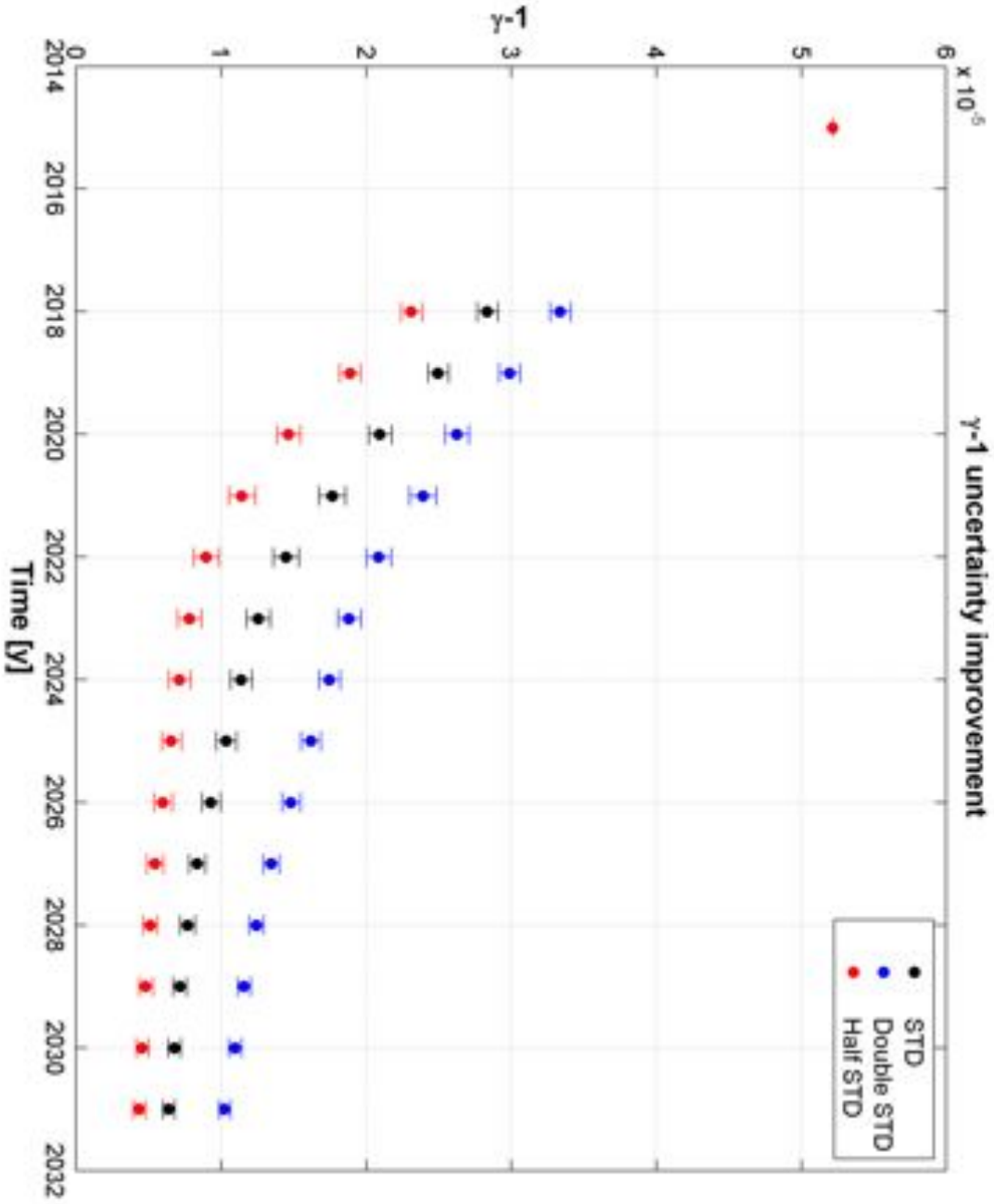

Figure 6.5: γ uncertainty improvement during a long time simulation using MoonLIGHT-2 CCRs

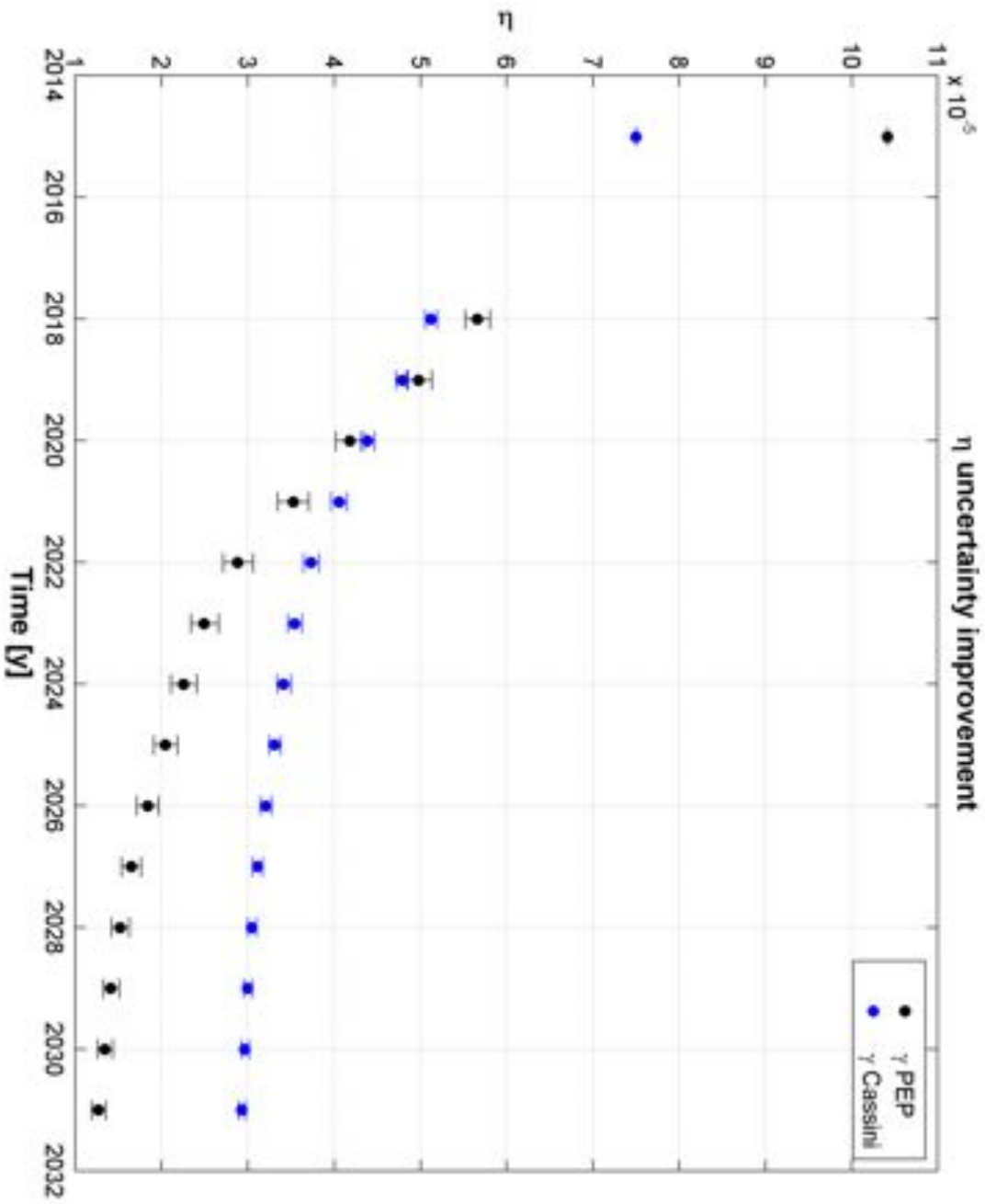

Figure 6.6: η uncertainty improvement during a long time simulation using MoonLIGHT-2 CCRs

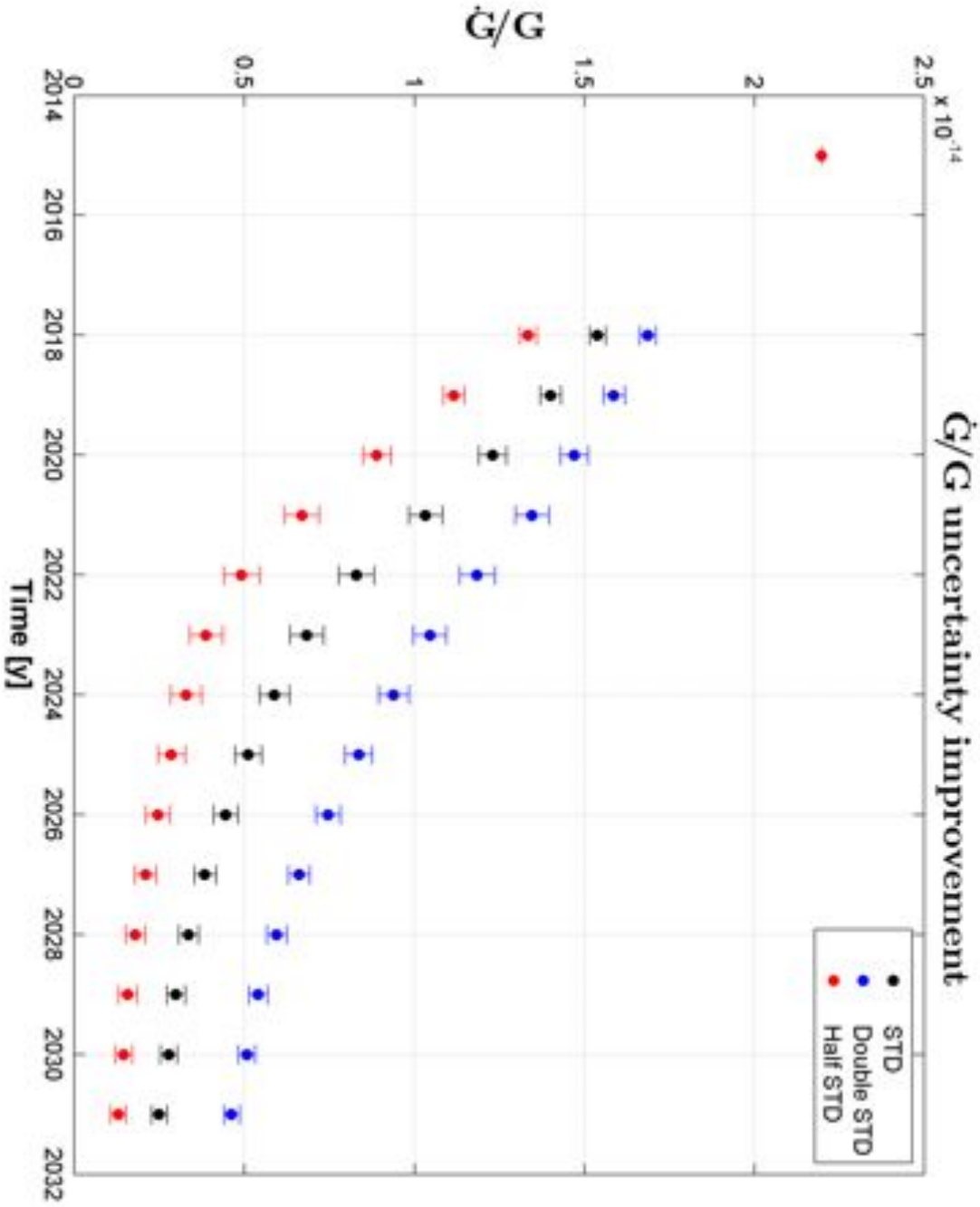

Figure 6.7: $\frac{\dot{G}}{G}$ uncertainty improvement during a long time simulation using MoonLIGHT-2 CCRs

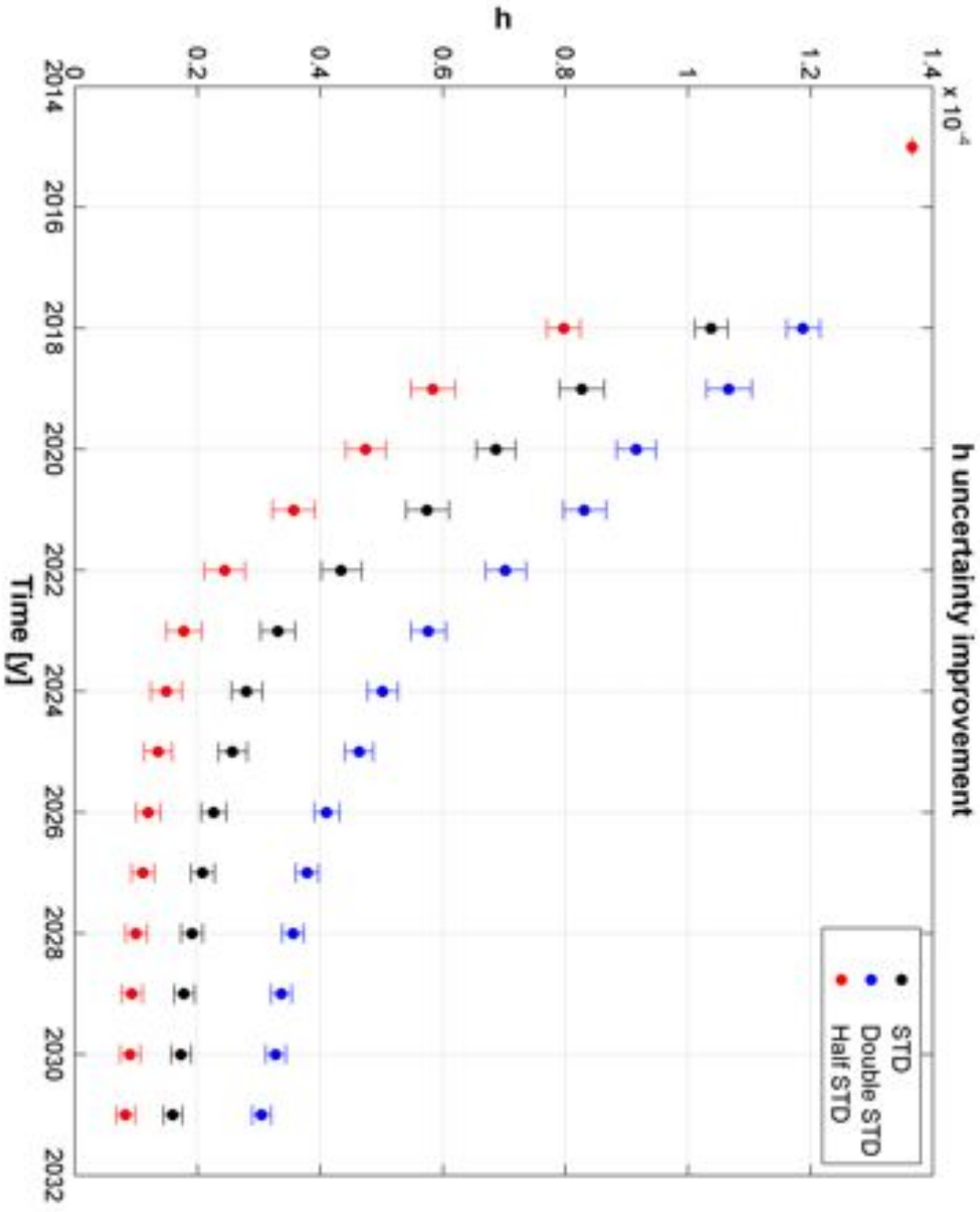

Figure 6.8: Geodetic precession uncertainty improvement during a long time simulation using MoonLIGHT-2 CCRs

Conclusions & Future prospects

Although Apollo retroreflectors will continue to operate and provide new science results, their geometry is now limiting the precision of the single photoelectron returns. The next generation retroreflector, MoonLIGHT-2, will support improvements in ranging precision, by one order of magnitude, depending on the method of deployment. Speaking about the experimental test done on MoonLIGHT-2 CCR we can conclude that the results shows that MoonLIGHT-2 can provide a mm-accuracy during lunar night. This is because the SUN-ON phase FFDPs are in good agreement with the simulations as shown by the longer τ_{CCR} and the reduced thermal gradient. Further analysis will be done in order to ensure the operatively phase not only during lunar night but also during lunar day time. However from the simulations reported in 4.3.1 we can see that we can obtain good GR results (see chapter 6) improvement using the payload even during the lunar night alone.
For the analysis part we can conclude that the simulations described in this work show that:

- The GR tests with MoonLIGHT-2 will be not dependent from the MoonLIGHT-2 deployment site with the exceptions of the poles (because of the lunar libration, the array is not always visible from Earth).

- There are not great differences in the GR tests using a MoonLIGHT-2 design with or without Sun-shade. So we choose the design without the sun-shade that will provide an important weight optimization (about 1kg) with similar results in GR tests.

- The improvements shown in the simulations represent the most pessimist case where we do not considerate the LLR station upgrade or any software update and only few MoonLIGHT deployed in non-optimal locations.

The ultimate scientific objective of MoonLIGHT-2 is to provide constraints on the theories that are proposed to determine the properties of Dark Matter and Dark Energy, and other gravitational theories [22]. This improved precision will be useful to identify the theoretical directions that will further the development of an understanding of these mysterious phenomena that lie beyond our current understanding. Summarizing we can say that the simulations showed in this thesis work are a good starting point in order to achieve better tests of GR using the Earth-Moon system and MoonLIGHT-2 CCRs. Nevertheless if we want to better investigate GR we have to include in our analysis data not only from the Moon but also from other rocky solar system bodies. By this end is possible to study not only Moon-related parameters but also other GR parameters.

For the near future we are moving forward to five main areas:

- **Test**: By the end of 2015, it is scheduled another MoonLIGHT test campaign. In particular we are going to change the MoonLIGHT design (see 4.3.3) in order to reduce the thermal conductivity between the CCR and the housing. The first test will be carried out removing the conformal can to reduce the thermal radiative load on the object. Using this new configuration we are going to study also the change in the optical performance of the CCR under space conditions.

- **Structural design**: At the same time, other MoonLIGHT configuration will be simulated at the SCF_Lab. These structural simulations concerns about the conformal can, the bracket and the tabs.
  The presence of the braces decreases the displacement on each corner-cubic surface of the can, especially at the intersection point of each braces couple (where the displacement is maximized). On the other hand, the use of the braces increases the weight of the entire can and therefore increases the stress

in the critical zones;
The braces increase the value of the first resonance frequency, so decreasing the problems due to shock and vibration loads;
The use of large tabs, instead of small tabs, decreases significantly the stress in the area closer to the tabs.
The structural simulations and the experimental tests must provide the best match between low thermal conductivity and a proper structure design avoiding stress during the launch.

- **Vibration tests**: After the items above and before the end of 2016, the validation tests for the launch will be carried out.

- **INRRI**: We are currently simulating the INRRI performance with the ExoMars EDM mission. With this simulations we want:
Geo-referencing of Mars surface using a preliminary version of a future Mars Geo/physics Network based on INRRI;
Using INRRI to measure GR parameters along with LLR measurements.

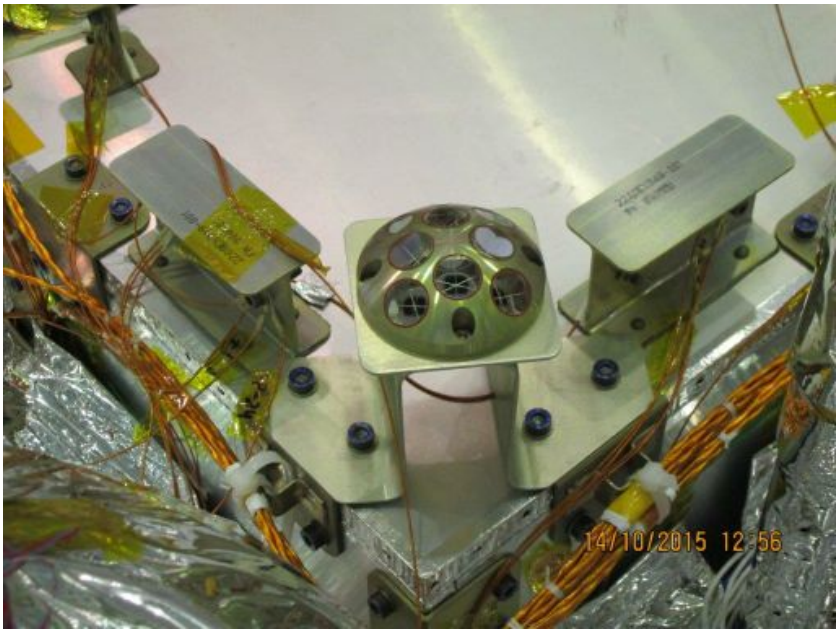

Figure 6.9: INRRI integrated on ExoMars EDM.

- **PEP improvements on GR tests**: We have already planned possible improvements in the PEP software in collaboration with the Center for Astrophysics. The first update concern about the computation of PPN parameter η in order to estimate the violation of the Equivalence Principle. Second, we also want to estimate the position of the Center of Mass of the Earth and Mars. Last, in order to realize INRRI simulations we have to introduce a new orbiter around Mars and simulate a link among the Earth ground station, the orbiter around Mars and the CCRs on Mars surface.

Most of all, after the MoonLIGHT deployment on the lunar surface, we will acquire the first new LLR data to begin the second generation of LLR measurements and GR tests.

Bibliography

[1] Martini M. et al. *MoonLIGHT: A USA-Italy lunar laser ranging retroreflector array for the* 21^{st} *century* Planetary and Space Science 74 (2012) 276?282

[2] Williams J.G., Boggs D.H., Ratcliff J.T., *A larger Lunar Core?*, 40^{th} Lunar and Planetary Science Conference, March 23-27, 2009.

[3] Williams J.G., Turyshev S.G., Boggs D.H., *Lunar Laser Ranging Test of the Equivalence Principle with the Earth and Moon*, Int. J. Mod. Phys. D, Volume 18, 1129-1175, 2009.

[4] Rambaux N., Williams J.G., Boggs D.H., *A dinamically Active Moon-Lunar Free Librations and Excitation Mechanism*, 39^{th} Lunar and Planetary Science Conference, March 10-14, 2008.

[5] Williams J.G., Boggs D.H., Ratcliff J.T. *Lunar Tides, Fluid Core and Core/Mantle Boundary* 39^{th} Lunar and Planetary Science Conference, March 10-14, 2008.

[6] Murphy T. et al., *Testing Gravity via Next Generation Lunar Laser-Ranging* Nuclear Physics B Proceedings Supplements, 134, 155.

[7] Nordtvedt K., *Testing the Equivalence Principle with laser ranging to the Moon* Adv. Space Res., 32, 1311.

[8] Dell'Agnello S., Boni A. et al *ETRUSCO-2: an ASI-INFN Project of Development and SCF-Test of GNSS Retroreflector Arrays (GRA) for Galileo and the*

GPS-3 17^{th} International Workshop on Laser Ranging, Bad Koetzting, Germany, (May 16-20, 2011)

[9] Dell'Agnello S., Cantone C. et al *SCF-Test of the NASA-GSFC "LAGEOS Sector" and of a Hollow Retroreflector* 17^{th} International Workshop on Laser Ranging, Bad Koetzting, Germany, (May 16-20, 2011)

[10] *The Lunar Laser Ranging Experiment*, Science, Volume 182, Issue 4109, pp 229-238, 1973

[11] Dell'Agnello et al., *Next Generation Lunar Laser Ranging and its GNSS Applications*, IEEE Aerospace Conference, Big Sky (MT), USA, March 2010 - Conference Proceeding

[12] Merkowitz S. et al. *The Moon as a Test Body for General Relativity* A white paper to the planetary science decadal survey

[13] http://www.physics.ucsd.edu/∼tmurphy/apollo/basics.html

[14] Dell'Agnello S. et al. *Creation of the new industry-standard space test of laser retroreflectors for the GNSS and LAGEOS* Adv. in Space Research, Vol.47, 822-842 (2011)

[15] Shapiro I., Reasenberg R. D., Chandler J. F., *Measurement of the de Sitter Precession of the Moon: A Relativistic Three-Body Effect*, Phys. Rev. Lett. 61, 2643-2646 (1988).

[16] http://www.physics.ucsd.edu/∼tmurphy/apollo/highlights.html

[17] Battat J. B. R., Stubbs C. W., Chandler J. F., *Solar system constraints on the Dvali-Gabadadze-Porrati braneworld theory of gravity*, Phys. Rev. D, 78, 022003, 2008.

[18] Reasenberg R. D., Shapiro I. I., MacNeil P. E., Goldstein R. B., Breidenthal J. C., Brenkle J. P., Cain D. L., Kaufman T. M., Komarek T. A., Zygielbaum A. I., Astrophysical. Journal Letters 234, L219 (1979).

[19] Chandler J. F., Reasenberg R. D., Shapiro I. I., Proceedings of the 7^{th} Marcel Grossman Meeting on recent developments in theoretical and experimental general relativity, gravitation, and relativistic field theories, edited by Jantzen R. T., Mac Keiser G., Ruffini R. (1996), p. 1501.

[20] Bertolami O., March R., Páramos J., *Solar System constraints to nonminimally coupled gravity*, Phys. Rev. D, 88, 064019, 2013.

[21] Williams J.G., Turyshev S.G., Boggs D.H., *Progress in Lunar Laser Ranging Tests of Relativistic Gravity*, Phys. Rev. Lett. 93, 261101 (2004).

[22] March R. et al., *Constraining spacetime torsion with the Moon and Mercury*, Phys. Rev. Letter D83, 104008, 2011

[23] M.E. Ash, *Generation of Planetary Ephemeris on an electronic computer*, MIT libraries Technical Report 63-391, 2 June 1965.

[24] R.D. Reasenberg, *The PEP A Priori facility*, MIT libraries Technical Report 54-612, 28 July 1975.

[25] R.D. Reasenberg, *De Sitter Precession of Earth-Moon Gyroscope*, MIT libraries Technical Report 87-03, 09 April 1987.

[26] J.F. Chandler, *Correcting the predicted chi square for a priori constraints*, MIT libraries Technical Report 88-06, 30 december 1988.

[27] R.D. Reasenberg, *The RMS predicted residual calculated in the analyze link of PEP*, MIT libraries Technical Report 80-01, 18 Januaryl 1980.

[28] J.F. Chandler, *A test of General Relativity through the Geodetic Precession of the Moon's orbit*, MIT libraries Technical Report 85-05, 20 december 1985.

[29] M.E. Ash, *Determination of Earth Satellite Orbits*, MIT libraries Techical Note 1972-5, 19 April 1972.

[30] M.J. Tausner, *General Relativity and its effect on planetary orbits and interplanetary observation*, MIT libraries Techical Report 425, 07 October 1966.

[31] M.A. Slade, *The Orbit of the Moon*, Partial fulfillment of the requirements for the degree of Doctor of Philosophy, September 1971.